

UCSF

UC San Francisco Electronic Theses and Dissertations

Title

Endoplasmic Reticulum stress-independent activation of unfolded response kinases by a small molecule ATP-mimic

Permalink

<https://escholarship.org/uc/item/4wx092pg>

Author

Mendez, Aaron Stephen

Publication Date

2015

Peer reviewed|Thesis/dissertation

**Endoplasmic Reticulum stress-independent activation of unfolded
protein response kinases by a small molecule ATP-mimic**

By

Aaron Stephen Mendez

DISSERTATION

DOCTOR OF PHILOSOPHY

in

Chemistry and Chemical Biology

in the

GRADUATE DIVISION

of the

UNIVERSITY OF CALIFORNIA, SAN FRANCISCO

Dedications and acknowledgments

I would like to thank Peter Water and Kevan M. Shokat for allowing me to be a part of their labs and for their patience and support. I would also like to thank all members of the Walter and Shokat labs for their advice in group meetings and help with laboratory techniques. Special shout out to Arvin C. Dar and Alexei V. Korennykh without whose help this project would not be possible. To my partners in crime on this project: Jennifer Alfaro and Marisol A. Morales Soto, who were instrumental in helping with the target identification of IPA and were commencement professionals throughout the project: Muchas gracias! To all members of team C.C.B (Noel Jee, Justin Rettenmaier, Klim Verba, Dan Kaemmerer) and the incoming C.C.B class of '09. Without their unique perspectives on life and entertainment, I would have never escaped the doldrums of graduate school. Thank you guys and party on!

Thanks to both the x-ray crystallography and NRM facility managers for putting up with my frantic late night emails and for their help with instrumentation. Thank you to lab managers in both the Shokat and Walter labs for their help with reagents, ordering, and constant enthusiasm. To Delany Lynch and Christine Genero, who helped me navigate both Peter's and Kevan's crazy schedules and who have also been a valuable resource for consulting. To the CCB graduate advisors, Julia Molla and Nichole Flowers, for their understanding, patience, and persistence in keeping me on track for graduation. Thank you. I know it's not easy.

I would like to thank the Mendez family for their love and support throughout graduate school. To my parents, Martha B. Mendez and Mike J. Mendez for keeping me motivated during the turbulent times. I love you both and many thanks. To my brothers Nicholas M. Mendez and Mike J. Mendez, Jr., who taught me that things could always be worse and to keep fighting. I would also like to thank my B.O.F group for keeping it real. They make anytime a great time and also provided me an outlet to vent during my early years of graduate school. To the current and former members of the Minority Science Programs (MSP) for providing me with the resources and opportunity to graduate. Thank you all! To my family away from home, Elif Karagoz, Silvia Ramundo, Jirka Peschek, and Diego Acosta-Alvear, you guys are great scientists and friends. Thank you all!

To Lindsey A. Harms: Thank you for putting up with my mood swings and existential crises. Graduate school can sometimes bring out the demons in people, and you might have seen mine. Thanks for being there for me and helping me through the bad times.

In Memory of:

Theresa Donovan and Valerie Ohman: They were strong and supportive women in my life when my mother was sick with cancer. They also looked out for my best interest as a student and were always a shoulder to cry on. Both the Walter and Shokat labs are not the same without these two extraordinary women.

Ana Maria Cano Aguilar and Vincente Perez Cortez, my grandparents who migrated from Jalisco, Mexico as teenagers and ultimately married and settled down in San Diego. They were instrumental in raising me as a young kid and helping me understand the natural world through farming. They both passed away before I could defend my thesis, but would be proud that I made it this far. Funding: I would like to thank the Howard Hughes Medical Institute (HHMI) and the Collaborative Innovation Award (CIA) for funding during my time at UCSF.

Endoplasmic Reticulum stress-independent activation of unfolded protein response kinases by a small molecule ATP-mimic

by

Aaron Stephen Mendez

Abstract

Two ER membrane-resident transmembrane kinases, IRE1 and PERK, function as stress sensors in the unfolded protein response. IRE1 also has an endoribonuclease activity, which initiates a non-conventional mRNA splicing reaction, while PERK phosphorylates eIF2 α . We engineered a potent small molecule, IPA, that binds to IRE1's ATP-binding pocket and predisposes the kinase domain to oligomerization, activating its RNase. IPA also inhibits PERK but, paradoxically, activates it at low concentrations, resulting in a bell-shaped activation profile. We reconstituted IPA-activation of PERK-mediated eIF2 α phosphorylation from purified components. We estimate that under conditions of maximal activation, less than 15% of PERK molecules in the reaction are occupied by IPA. We propose that IPA binding biases the PERK kinase towards its active conformation, which trans-activates apo-PERK molecules. The mechanism by which partial occupancy with an inhibitor can activate kinases may be wide-spread and carries major implications for design and therapeutic application of kinase inhibitors.

Table of Content

Dedications and acknowledgments.....	iii
Abstract	vi
Table of Content	v
Tables	x
Table of Figures.....	xi
1 The Unfolded Protein Response.....	1
1.1 Conformation and Self-Assembly of IRE1 By Cofactors.....	5
1.1.1 Insight Into PERK Kinase Activation	7
2 Introduction	8
3 Results	11
3.1 Generation of small molecule activators of IRE1 α	11
3.2 In vivo effects of IPA on IRE1 α Signaling.....	20
3.3 <i>In vivo</i> effects of IPA on the ATF6 and PERK UPR branches	23
3.4 IPA activates PERK at low concentrations.....	27
3.5 PERK inhibitors block IPA-induced PERK activation.....	29

4	Discussion	35
5	Contributions	40
6	Work Cited	41
7	Material and Methods.....	49
7.1	Cell Culture	49
7.2	Live cell imaging	49
7.3	Metabolic labeling	49
7.4	Cell viability assays	50
7.5	RNA isolation and RT-PCR.....	51
7.6	Protein expression and purification.....	52
7.6.1	IRE1 α -KR43.....	52
7.6.2	PERK (580-1077aa) murine	53
7.6.3	PERK mammalian (535-1093 Δ 660-868).....	54
7.7	Immunoblotting	54
7.8	In vitro endoribonuclease IRE1 α activity assay	55
7.9	Generation of XBP1 reporter cell line	56
7.10	Kinase-inhibitor profiling	57

7.11	In vitro PERK cross-linking assay	57
7.12	In vitro PERK kinase assay	58
7.12.1	PERK activation assay	58
7.13	Chemical synthesis.....	59
7.13.1	Synthesis of intermediate 3	59
7.13.2	Synthesis of intermediate 5	60
7.13.3	Synthesis of AD75/cmp1	61
7.13.4	Synthesis of AM1/cmp4.....	62
7.13.5	Synthesis of AM2	63
7.13.6	Synthesis of AM3	64
7.13.7	Synthesis of AM4 / cmp5.....	65
7.13.8	Synthesis of AM5	66
7.13.9	Synthesis of AM6	67
7.13.10	Synthesis of AM7	68
7.13.11	Synthesis of AM8	69
7.13.12	Synthesis of AM9/IPA	70
7.13.13	Synthesis of AM10/cmp3	71
7.13.14	Synthesis of AM11	72

7.13.15	Synthesis of AM12.....	73
7.13.16	Synthesis of AM13.....	74
7.13.17	Synthesis of AM14.....	75
7.13.18	Synthesis of AM15.....	76
7.13.19	Synthesis of AM16.....	77
7.13.20	Synthesis of AM17.....	78
7.13.21	Synthesis of AM18.....	79
7.13.22	Synthesis of AM19.....	80
7.13.23	Synthesis of AM20/cmp2.....	81
7.13.24	Synthesis of AM21.....	82
7.13.25	Synthesis of AM22.....	83
7.13.26	Synthesis of AM23/IPAx.....	84
7.13.27	Synthesis of AM24.....	85
7.13.28	Synthesis of AM25/cmp9.....	86
7.13.29	Synthesis of AM26.....	87
7.13.30	Synthesis of AM27/cmp10.....	88
7.13.31	Synthesis of AM28/cmp7.....	89
7.13.32	Synthesis of AM29/cmp8.....	90

7.13.33	Synthesis of AM30	91
7.13.34	Synthesis of AM31	92
7.14	Raw Kinome data	93

Tables

Table 1 Invitrogen kinome screen raw data	93
--	-----------

Table of Figures

Figure 1: The Unfolded Protein Response	3
Figure 2: The core scaffold of APY29	12
Figure 3: Structure-activity analysis of activating compounds	14
Figure 4: Characterization of IRE1 activators	17
Figure 5: Concentration dependence of IPA, cmp1, and APY29 on IRE1 α .	18
Figure 6: Structure of APY based compound	19
Figure 7: IPA activates the IRE1 branch of the UPR in HEK293T cells	21
Figure 8: AD60 inhibition of XBP1-luciferase-splicing in HEK293T	22
Figure 9: IPA mediated activation of IRE1 in HEK293T cells	23
Figure 10: Effects of IPA on the ATF6 and PERK branches of the UPR	25
Figure 11: <i>In vitro</i> effects of IPA on GST-PERK kinase activity	28
Figure 12: Inhibition of IPA-mediated PERK activation by GSK2606414	30
Figure 13: Effects of IPA-mediated PERK activation in HEK293T cells	31
Figure 14: Reconstitution of activation of cytosolic PERK protein in vitro.	34
Figure 15: In vitro higher-ordered oligomerization of PERK.....	34
Figure 16: Proposed model for PERK activation.....	37
Figure 17: Langmuir isotherm equation	59
Figure 18: Synthesis of intermediate 3.....	60
Figure 19: Synthesis of intermediate 5.....	60
Figure 20: Synthesis of AD75/cmp1	61

Figure 21: Synthesis of AM1/cmp4	62
Figure 22: Synthesis of AM2	63
Figure 23: Synthesis of AM3	64
Figure 24: Synthesis of AM4 / cmp5	65
Figure 25: Synthesis of AM5	66
Figure 26: Synthesis of AM6	67
Figure 27: Synthesis of AM7	68
Figure 28: Synthesis of AM8	69
Figure 29: Synthesis of AM9/IPA	70
Figure 30: Synthesis of AM10/cmp3	71
Figure 31: Synthesis of AM11	72
Figure 32: Synthesis of AM12	73
Figure 33: Synthesis of AM13	74
Figure 34: Synthesis of AM14	75
Figure 35: Synthesis of AM15	76
Figure 36: Synthesis of AM16	77
Figure 37: Synthesis of AM17	78
Figure 38: Synthesis of AM18	79
Figure 39: Synthesis of AM19	80
Figure 40: Synthesis of AM20/cmp2	81
Figure 41: Synthesis of AM21	82
Figure 42: Synthesis of AM22	83

Figure 43: Synthesis of AM23/IPAx	84
Figure 44: Synthesis of AM24	85
Figure 45: Synthesis of AM25/cmp9	86
Figure 46: Synthesis of AM26	87
Figure 47: Synthesis of AM27/cmp10	88
Figure 48: Synthesis of AM28/cmp7	89
Figure 49: AM29/cmp8	90
Figure 50: Synthesis of AM30	91
Figure 51: synthesis of AM31	92

1 The Unfolded Protein Response

The endoplasmic reticulum (ER) serves as a folding compartment for secreted and membrane proteins in eukaryotic cells. These proteins enter the ER as nascent, unfolded polypeptides at flux rates that can vary widely within the same cell depending on the physiological demand. During differentiation of B cells into antibody-secreting plasma cells (1) and during secretory tissue development (2), progenitor cells are transformed into professional secretory cells that output thousands of folded proteins per second (3-5). During this transition, the ER abundance increases to accommodate the demand for protein production. ER expansion is driven by sensors of protein-folding quality embedded in the ER membrane. These sensors detect unfolded proteins inside the ER and activate a signal transduction program known as the unfolded protein response (UPR), which maintains homeostasis of protein folding.

In eukaryotic microorganisms such as yeasts, a single sensor of unfolding proteins, Ire1, controls the UPR (4, 6). Ire1 belongs to the family of protein kinases, and harbors an N-terminal sensor domain in the ER lumen and a CDK2-like serine/threonine kinase domain fused to a unique C-terminal ribonuclease (RNase) domain in the cytosol (7) (Figure 1). The sensor domain detects unfolded proteins and promotes higher-order oligomerization of Ire1 in the plane of the ER membrane, which activates the RNase domain (8-12).

The mechanism by which the sensor domain detects unfolded proteins has been debated and converged to two possible models. One model poses a competition between unfolded proteins and the sensor domain of Ire1 for binding to the ER-resident chaperone binding immunoglobulin protein (BiP). According to this model, unfolded proteins activate Ire1 by binding to BiP and causing its dissociation from the sensor domain of Ire1 (13, 14). An alternative model poses direct binding of unfolded proteins to the sensor domain of Ire1 (9). This model is supported by the finding that Ire1 mutants, unable to bind BiP, still respond to ER stress. This observation suggests that BiP does not serve as the primary activating switch, but instead provides a buffer that maintains the concentration of free Ire1 monomers at an appropriate level for sensing unfolded proteins (15, 16).

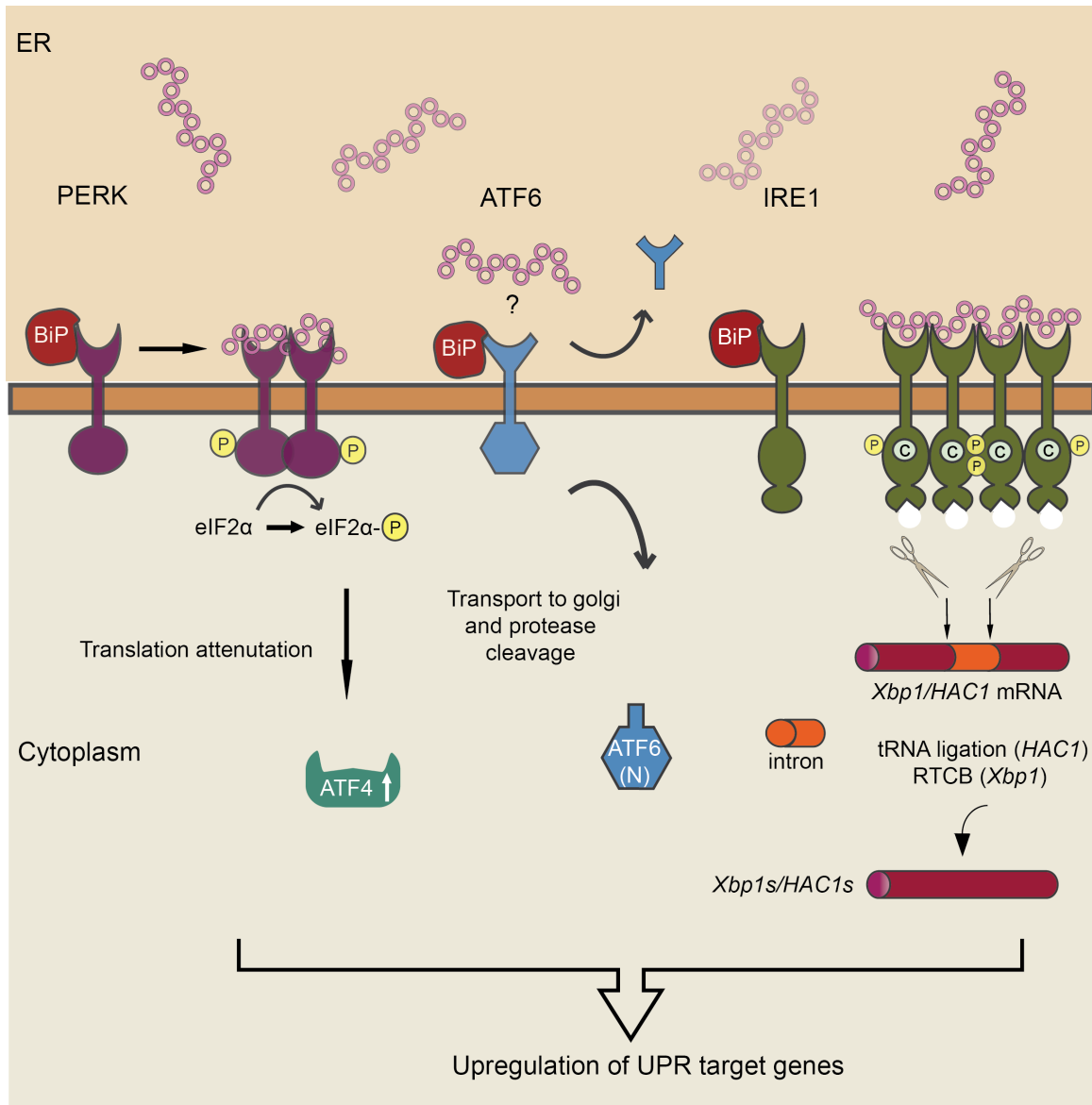


Figure 1: The Unfolded Protein Response

The three unfolded protein response (UPR) branches in higher eukaryotes. The UPR is controlled by three sensors of unfolded proteins in the endoplasmic reticulum (ER) membrane (IRE1, PERK, and ATF6). The sensors activate transcriptional programs that collectively reestablish the homeostasis of protein folding in the ER. Unfolded proteins are thought to bind directly to the sensors domains of IRE1 and PERK while the mechanism of unfolded-protein detection by ATF6 remains unknown.

The kinase activity of Ire1 is not essential for UPR activation (17-20). The Kinase domain in Ire1 serves as an allosterically regulated scaffold that enables oligomerization of the RNase domain (11, 20, 21). Autophosphorylation of Ire1 kinase results in stronger Ire1 self-association (11) and promotes a faster shutdown upon ER adaptation, which reveals two roles of the phosphate groups in tuning the RNase activity of Ire1 (17, 19). ADP and synthetic ligands that bind to the ATP pocket provide another mechanism for allosteric tuning of Ire1 RNase (10, 20), as do ligands that dock to a unique binding pocket created at the dimerization interface in the RNase domain (22).

Activated Ire1 RNase cleaves *HAC1* (yeast) or *Xbp1* (metazoan) mRNA at two unconventional splice sites, which releases an intron (5, 6). The resulting two exons are joined by tRNA ligase in yeast and by RtcB in metazoans (7, 23, 24), which produces mRNA encoding functional Hac1 or XBP1 transcription factors. The transcription factors enter the nucleus and activate the production of UPR target genes, many of which are directly involved in ER functions. This mechanism establishes a feedback loop that relieves the ER stress by supplying more ER protein folding capacity to the cell at issue.

The UPR in metazoan cells contains two additional signaling branches, one controlled by the ER membrane-resident kinase PERK and the other by the membrane-tethered transcription factor ATF6 (5, 12). The sensor domains of PERK and IRE1 reside in the ER lumen, share homology with one another, and likely use a similar mechanism for unfolded protein detection. The kinase domain of PERK is closely related to a cytosolic kinase, PKR, that provides antiviral innate immunity (25-28). PKR

and PERK share a downstream signaling substrate, and both inhibit translation by phosphorylating translation initiation factor eIF2 α (Figure 1). The PERK-induced translational block relieves the ER from unfolded proteins by reducing the influx of new polypeptides. Under conditions of reduced translation initiation, some mRNAs become preferentially translated, which leads to the production of another transcription factor, ATF4, that also drives UPR target genes (5, 13, 25, 29). The third UPR sensor, ATF6, contains an ER luminal domain that by sequence comparison does not resemble any other proteins. It is unknown how unfolded proteins activate ATF6. The downstream events of ATF6 signaling are much better understood (**Figure 1**) (5, 30). ER stress results in vesicular export of ATF6 from the ER followed by its sequential proteolytic cleavage by S1P and S2P proteases in the Golgi complex. The cleavages sever the cytoplasmic domain of ATF6 from its transmembrane anchor and ER luminal domain. The cytoplasmic ATF6 domain then enters the nucleus and transcriptionally up regulates UPR in metazoan cells, which cross-communicate to form an integrated signaling network (5).

1.1 Conformation and Self-Assembly of IRE1 By Cofactors

The RNase activity of IRE1 and its oligomerization equilibrium depend on the presence of cofactors bound to the ATP pocket of IRE1 kinase (12, 20). Under optimal conditions, the RNase activity of IRE1 from yeast and human increases by up to 20-fold upon binding of AMP; ATP; or sunitinib, a US Food and Drug Administration approved

anticancer drug. ADP and synthetic small molecules such as APY29 and its derivatives are the most potent cofactors and can induce a 100-fold activation (11, 26).

Studies of cofactor-induced IRE1 activation were unexpectedly facilitated by a sulfur-substituted ADP variant, ADP β S. ADP β S binds well to the kinase domain but, paradoxically, does not cause oligomerization or activation of the RNase. Replacing magnesium with manganese, a more thiophilic metal ion, completely restored the cofactor activity of ADP β S(10, 12). This observation reveals a strong metal-specificity switch and indicates the cofactors that activate IRE1 in two steps. The first step is binding to the ATP pocket, which occurs without changing the conformational properties of the IRE1 kinase domain that affect IRE1 activation. The second step involves protein interaction with the phosphodiester-magnesium moiety at the β -phosphate-binding site (10).

Superposition of the inactive IRE1 monomer onto the active back-to-back dimer shows a profound steric clash between the α C-helix and a partnering IRE1 monomer. The assembly of the back-to-back dimer and consequently, of the higher-order oligomer is sterically prohibited unless the kinase domain and the α C-helix are in the active conformation. Once activated, the IRE1 kinase domains would force dimerization, which would move the α C-helix into the active conformation. Such a rearrangement would enable productive ATP docking and phosphoryl transfer. Similar mechanisms of activation occur upon cyclin binding to CDK2 and during the asymmetric epidermal growth factor receptor (EGFR) dimerization (31, 32). Conformational perturbations of

the α C-helix by ligands in the ATP pocket could, in principle, modulate IRE1's oligomeric state and RNase activity. This mechanism readily explains how different small molecules that bind to the ATP pocket can be either activators or inhibitors of IRE1 RNase (20, 21).

1.1.1 Insight Into PERK Kinase Activation

PERK kinase resides in the ER membrane of metazoan cells and controls a second branch of metazoan cells and a second branch of the UPR. PERK phosphorylates the ubiquitous translation initiation factor eIF2 α to repress translation globally. In the short term, PERK increases cell survival by relieving the ER stress. In the longer term, it activates a transcriptional program that complements IRE1 signaling and contributes to the cytoprotective/apoptotic functions of the UPR (5, 30, 33). The first structure of the kinase domain of mouse PERK revealed a back-to-back dimer that closely resembles the back-to-back arrangement of IRE1's kinase domains.

The kinase domain of PERK is found in the active conformation, as indicated by the positions of the α C-helix and the activation loop (25). The ATP-binding pocket of PERK is empty, which suggests that, as observed for oligomeric IRE1 with an unoccupied ATP pocket, dimerization/oligomerization is sufficient to induce the active conformation of the kinase domain (12). The close similarity of their activation mechanisms, self-assembly by their sensory domain, suggest that dimerization activates both kinases via a similar mechanism. We expect that the back-to-back dimerization interface mechanically places the α C-helix of PERK kinase into the active

conformation, just as in the inactive conformation the α C-helix would clash with the dimerization interface. The similar mode of activation of PERK like IRE1 could readily explain how different types of ATP-mimetic elicit differential responses, i.e., pathway activation or inhibition.

2 Introduction

Roughly 30% percent of all proteins encoded in eukaryotes pass through the endoplasmic reticulum (ER), where they are folded, modified, and assembled before they are delivered to the plasma membrane, the outside of the cell, or to various way-stations in the secretory and endocytic pathways. To ascertain fidelity during protein maturation, ER-resident unfolded protein sensors continuously monitor the folding status in the ER lumen. The Unfolded Protein Response (UPR) is induced when the protein folding capacity of the ER is surpassed, triggering the activation of three transmembrane sensors/signal transducers, IRE1 (inositol-requiring enzyme 1), PERK (protein kinase RNA (PKR)-like ER kinase), and ATF6 (activating transcription factor-6). Two of the sensors, IRE1 and PERK, are protein kinases that are amenable to modulation by small molecule ATP-mimetics.

IRE1 is the most conserved of these proteins. It contains an ER-luminal sensor domain that is activated by binding directly to unfolded polypeptides (5, 9, 16). As a result, IRE1 oligomerizes, activating its cytosolic kinase and endoribonuclease domains. IRE1's RNase domain initiates a non-conventional splicing reaction that results in the

excision of an intron from the mRNA, encoding the transcription factor XBP1 (7, 11, 34). XBP1 produced from the spliced mRNA drives transcription of UPR target genes to remedy ER stress. The luminal domain of PERK is homologous to that of IRE1, and thus, its activation is presumably also driven by direct binding to unfolded polypeptides. Active PERK phosphorylates the α -subunit of eukaryotic translation initiation factor 2 (eIF2 α) (35), leading to trapping eIF2 α in its GDP-bound inactive state, which blocks eIF2 α recycling. As a result, global protein synthesis is attenuated, while a few mRNAs, including the mRNA encoding the transcription factor ATF4, are preferentially translated (36, 37).

Recent chemical genetic work in our laboratories revealed that phospho-transfer by Ire1's kinase domain can be bypassed using an ATP mimetic (1NM-PP1) (11, 18, 20). Starting with studies in *S. cerevisiae*, we showed that Ire1's RNase modality can be activated using a small molecule ATP mimetic (1NM-PP1), when used in conjunction with a mutant form of Ire1 ("IRE1-as" for analog sensitive) that allows 1NM-PP1 to bind to the ATP-binding site of IRE1's kinase domain. Subsequent work showed that the RNase activity of wild type Ire1 can too be activated pharmacologically with the broad-acting kinase inhibitors APY29 and Sunitinib *in vitro* (11). The crystal structure of the Ire1 kinase/RNase domains bound to APY29, combined with biophysical and enzyme kinetic analyses, showed that binding of ATP-mimetic ligands to Ire1's active kinase site predisposes the enzyme to oligomerization, which activates its RNase activity.

Ligand binding to the ATP binding pocket in IRE1's kinase domain, however, does not always result in oligomerization and RNase activation. Rather, activation

requires that IRE1's kinase domain remain in its *active* conformational state, characterized by the inward positioning of the α C helix and the DFG-loop in the kinase active site (DFG/ α C-in conformation) (10, 20, 38-40). Thus, ATP-mimetic ligands that trap IRE1's kinase domain in the inactive, DFG/ α C -out conformation act as inhibitors, rather than activators, of IRE1 oligomerization and signaling via its RNase domain. Because RNase activation can occur in the absence of a phospho-transfer reaction, IRE1 is unique in that it is possible to monitor the functional consequences of conformational changes in the kinase domain induced by ligand occupancy of the ATP-binding site without the risk of losing the kinase activity.

The model depicting IRE1's kinase domain as a switch that becomes trapped in two states (DFG/ α C - in and DFG/ α C - out) depending on the ligand bound to its active site is an over-simplification. Different ligands yield different plateaus of maximal oligomerization and RNase activation, even when saturating the active site. This seemingly perplexing property is reconciled by the model in which different ligands predispose IRE1's kinase domain to populate the DFG/ α C - in and DFG/ α C - out states to different degrees; a strong IRE1 RNase activator would stabilize the DFG/ α C -in state, whereas a weaker one would bias the IRE1 molecules in the population towards the DGF/ α C - in state, without completely trapping them in this state. The reverse would be true for IRE1 RNase inhibitors, which would bias IRE1's kinase domain towards the DFG/ α C - out state.

To date, models of IRE1 activation have largely been derived from *in vitro* characterizations that lack *in vivo* confirmation, as the available tools were non-selective, and thus excessively toxic, to test in living cells (21, 41, 42). Moreover, while 1NM-PP1 predisposes IRE1-as towards activation, it proved insufficient to activate IRE1 in cells in the absence of ER stress (which vastly concentrates IRE1 by virtue of oligomerization of the luminal domain) or over-expression (43-45). Here, we describe the development of a novel small molecule, IPA, as the lead compound of a series of second-generation IRE1 activators. Surprisingly, IPA activates not only IRE1's RNase, but also PERK signaling but, by contrast to its ability to activate IRE1, only at low concentrations. We propose that PERK activation results from ligand induced conformational changes in a small percentage of the molecules in the population that then interact with and activate PERK molecules containing an empty active site.

3 Results

3.1 Generation of small molecule activators of IRE1 α

Recent work identified an ATP mimetic that activates mammalian IRE1 α 's RNase activity *in vitro* (11, 20, 21, 40, 46). These results, along with the co-crystal structure of *S. cerevisiae* Ire1 with the aminopyrazole-based inhibitor APY29 (PDB ID: 3FBV) (11), provided a starting point to develop more selective and more potent IRE1 activators. We reasoned that 1) the cyclopropyl substituent on the pyrazole ring, which binds to the

gatekeeper pocket in the *S. cerevisiae* Ire1 structure, would be a key determinant of human IRE1 α binding, 2) interactions of the hinge-binding element of the APY29 scaffold would be essential to stabilizing IRE1 α 's kinase domain in a conformation leading to RNase activation, and 3) the pyrimidine ring, which occupies the adenine pocket in the *S. cerevisiae* structure, would provide an appropriate space filling moiety that further enhances affinity to the ATP binding pocket (11, 47). We therefore kept these three elements constant in further optimizations and explored varying substituents attached to the pyrimidine ring for their ability to improve properties of the compounds.

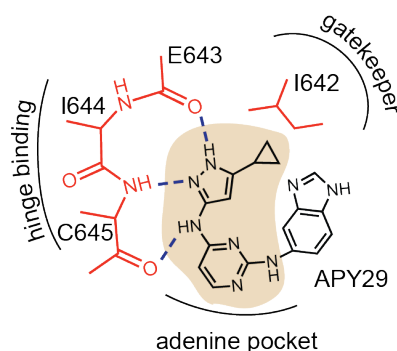


Figure 2: The core scaffold of APY29

Aminopyrazole pyrimidine-base indicated in beige

To this end, we modified the molecule by substituting urea-linked and variably *m*- and *p*-substituted phenyl groups for the benzimidazole of APY29. Diphenyl urea linkers have previously been used successfully in the design of kinase inhibitors (11, 47, 48). In

exploring the addition of this chemotype on the APY29 scaffold, we generated a series of 31 variants each member was tested in an RNase activity assay using recombinant IRE1 α -KR43 and a fluorescent short hairpin RNA substrate derived from human XBP1 mRNA (49). The activating compounds were compared to three parent compounds (APY29, AD75, and NHC57-1). A panel of the 10 best compounds were then used in a follow up assay to determine their relative rate constants (k_{obs}). For simplicity the numbering of the compounds were changed (see Figure 4A and Chemical synthesis). IRE1 α -KR43 comprises the soluble cytoplasmic portion of IRE1 α , composed of the kinase and RNase domains plus 43 amino acids of the linker that bridges the kinase to its transmembrane domain.

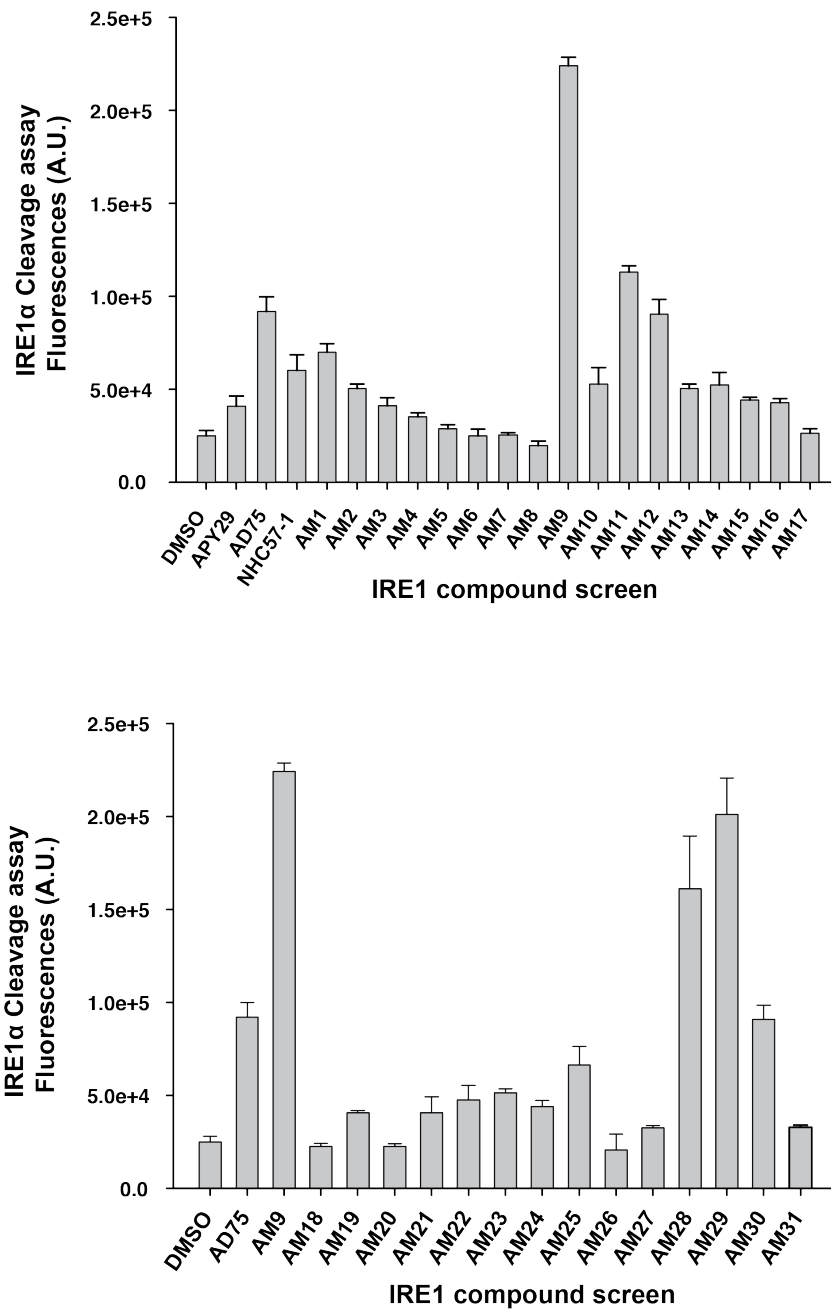


Figure 3: Structure-activity analysis of activating compounds

Compounds were assayed at 1 μ M in a RNA cleavage assay containing IRE1 α -KR43 (200 nM) and a fluorescently labeled RNA probe (see methods).

As expected from the chemical design strategy, we produced a series of IRE1 α RNase activators. We observed that compounds bearing *m*-trifluoromethyl, *p*-methyl, *p*-ethyl, *m*-methoxy, and *p*-methoxy groups on the terminal phenyl ring (**cmp1**, **cmp2**, **cmp3**, **cmp4**, and **cmp5**) activated IRE1 α -KR43 activity 10-100-fold under assay conditions, as compared to 5-fold by the parent compound APY29) (Figure 4A). These results were surprising, because the presence of an *m*-trifluoromethyl group was previously shown to be important to retain activity of related kinase inhibitors but, as shown here, is not essential for activation of IRE1 α -KR43. We were also surprised that the activity was improved further by the presence of a *p*-substituted thioether group and, similarly albeit weaker, by the presence of a *p*-iodo group (cmp6 and cmp7, 900-fold RNase activation under assay conditions). We conclude that IRE1 α prefers a substituent with polarizable character at the para-position of the terminal phenyl ring, perhaps indicating that the ring occupies a hydrophobic region in IRE1 α 's active site. Increasing bulkiness at the para-position resulted in decreased activities (cmp8, cmp9, and cmp10), suggesting that the size of this pocket must be limited.

We decided to further characterize compound cmp6, based on its robust activation properties. Henceforth, we refer to cmp6 as IPA (for IRE1/PERK Activator) for reasons to be discussed below. To validate that binding of IPA to IRE1 α 's kinase domain is critical for IRE1 α RNase activation, we generated a control compound, IPAx.

In IPAx, the pyrazole ring bears an additional N1-methyl group that is predicted to sterically interfere with binding to the gatekeeper pocket in IRE1 α (Figure 1) Indeed, when assayed for activation of IRE1 α RNase activity, IPAx was inactive showing an indistinguishable effect from the DMSO control (Figure 4A).

ATP mimetics, such as APY29, induce IRE1 α -KR43 oligomerization, which in turn activates the RNase activity (11, 20, 45). To assess whether IPA acts through a corresponding mechanism, we measured RNase activity as a function of enzyme concentration in the presence of saturating compound concentrations (Figure 4B and Figure 5). When no activator was added, apo-IRE1 α -KR43 RNase activity, measured as k_{obs} under single-turnover conditions, increased sharply with increasing enzyme concentration, reaching $\frac{1}{2} k_{max,obs}$ at 8 mM (Figure 4B, purple circles).

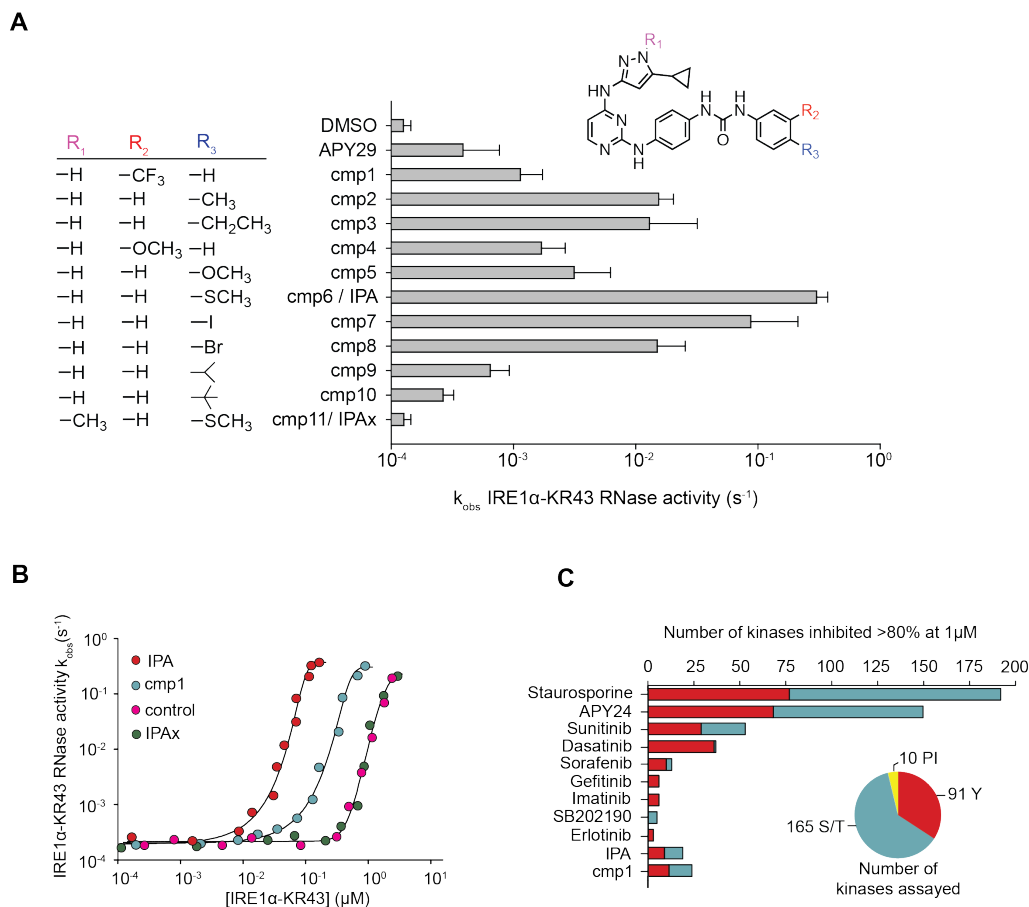


Figure 4: Characterization of IRE1 activators

(A) Structure-activity analysis of activating compounds. Compounds were assayed at 1 μM in a RNA cleavage assay containing IRE1 α -KR43 (200 nM) and 5' [^{32}P] – labeled RNA substrate HP21 (see Methods). IPAx is methylated at the N[1] position in the pyrazole ring indicated as shown in R₁. (B) The effects of activating compounds (50 μM) as a function of IRE1 α -KR43 concentration. $1/2k_{\text{max, obs}}$ and Hill coefficients ('n') were calculated (IPA: $1/2k_{\text{max, obs}} = 0.43 \mu\text{M}$, $n = 4.2$; cmp1: $1/2k_{\text{max, obs}} = 3 \mu\text{M}$, $n = 3.8$; IPAx $1/2 k_{\text{max, obs}} = 8 \mu\text{M}$, $n = 3.3$, DMSO control: $1/2k_{\text{max, obs}} = 8 \mu\text{M}$, $n = 3.3$) (C) compounds and FDA-approved drugs (all at 1 μM) were screened against a panel of 266 recombinant human kinases ("S/T" : Ser/Thr protein kinases; "Y" : Tyr protein kinases, "PI" phosphatidylinositide lipid kinases. APY24 contains the aminopyroazole pyrimidine-base, which is similar to APY29

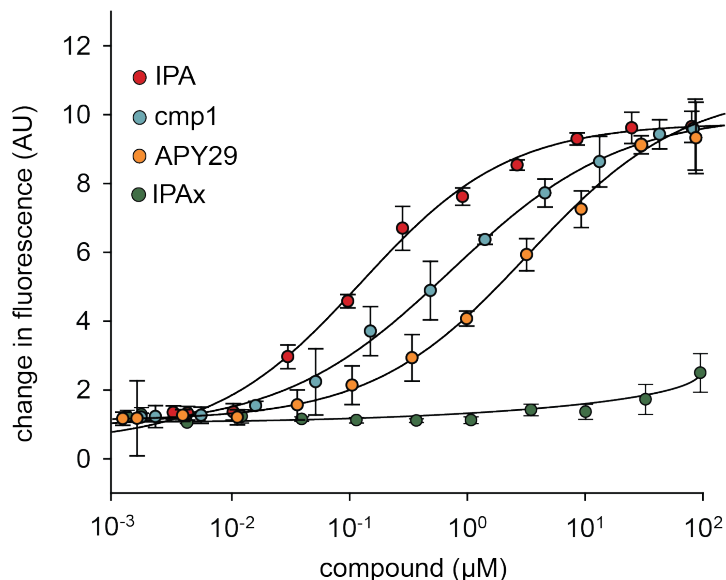


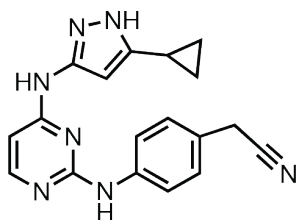
Figure 5: Concentration dependence of IPA, cmp1, and APY29 on IRE1 α

A fluorescence RNA substrate (HP17) containing a 5' fluorescein and 3' black hole quencher was used to determine RNase activity at a constant concentration of IRE1 α ([IRE1 α -KR43] = 100 nM; IPA EC₅₀ = 0.36 μ M; APY29 EC₅₀ = 5.2 μ M; cmp1 EC₅₀ = 0.95 μ M).

The measured Hill coefficient of the activation was $n = 3.3$, indicating that, consistent with previous work (45), enzymatic activation parallels oligomerization. By contrast, in the presence of **cmp1** or IPA, IRE1 α -KR43 RNase activity reached $\frac{1}{2}$ $k_{\max, \text{obs}}$ at ~ 3 - and 20-fold lower enzyme concentrations, respectively ($\frac{1}{2} k_{\max, \text{obs}} = 3 \mu\text{M}$ and $0.43 \mu\text{M}$; and $n = 3.8$ and 4.2 , Figure 4B, red and blue circles), indicating that **cmp1** and IPA binding significantly predispose IRE1 α -KR43 to oligomerization and activation. By contrast, addition of IPAx did not enhance IRE1 α activation, showing activation

kinetics that were in all respects indistinguishable from the no-compound control (Figure 4B, pink circles), consistent with its inability to bind to IRE1 α -KR43 (Figure 4B and Figure 5).

Kinome-wide screening of cmp1 and IPA demonstrated a dramatic improvement of selectivity for both molecules when compared to APY24 (Figure 4C and Figure 6), a close analog of APY29, containing the same core-scaffold. In this assay, compounds were screened at a fixed concentration of 1 μ M against a panel of 266 kinases, and the number of those inhibited by \geq 80% were scored (Figure 4C). We also included in the analysis several bench-mark inhibitors, such as the promiscuous natural product staurosporine and several clinically approved kinase inhibitors. We note that both cmp1 and IPA show better selectivity profiles when compared to the clinically approved compounds Sunitinib and Dasatinib.



APY24

Figure 6: Structure of APY based compound

The structure of APY24 contains a aminopyrozole pyrimidine core similar to APY29

3.2 In vivo effects of IPA on IRE1 α Signaling

To examine the effects of IPA in living cells, we monitored the UPR in HEK293T cells using RT-PCR to measure splicing of *XBP1* mRNA. We found that IPA induced *XBP1* mRNA splicing in a time- and dose-dependent manner (Figure 7A). At a concentration of 2 μ M IPA, splicing was induced within two hours (lane 5). As expected, IPAx did not induce *XBP1* mRNA splicing (Figure 7B, lane 3). We used tunicamycin (Tm), which induces ER stress by blocking *N*-linked glycosylation, as a positive control to induce the UPR (Figure 7A, lanes 7, and Figure 7B, lane 4).

To further rule out off-target effects through which IPA might induce ER stress indirectly, we use a recently discovered IRE1 α inhibitor, AD60, expected to bind to an inactive conformation of IRE1 α and inhibit its RNase activity while competing for IPA binding (11, 47, 48). Like IPA, AD60 is predicted to bind to the ATP binding pocket of IRE1 α 's kinase domain. Using an *XBP1* mRNA-splicing reporter that produces an *XBP1*-luciferase fusion protein only after IRE1-mediated splicing of its mRNA, we determined an IC₅₀ of 0.85 μ M for AD60 in HEK293T cells (Figure 7C and Figure 2-figure supplement 1). As expected, AD60 inhibited Tm-induced *XBP1* mRNA splicing (Figure 7C, lane 3). Likewise, AD60 fully ablated IPA-induced *XBP1* mRNA splicing (Figure 7C, lanes 9-12), even at the highest IPA concentration tested. Taken together, these results confirm that IPA binds to the ATP-pocket of IRE1 α to induce *XBP1* mRNA splicing in cells.

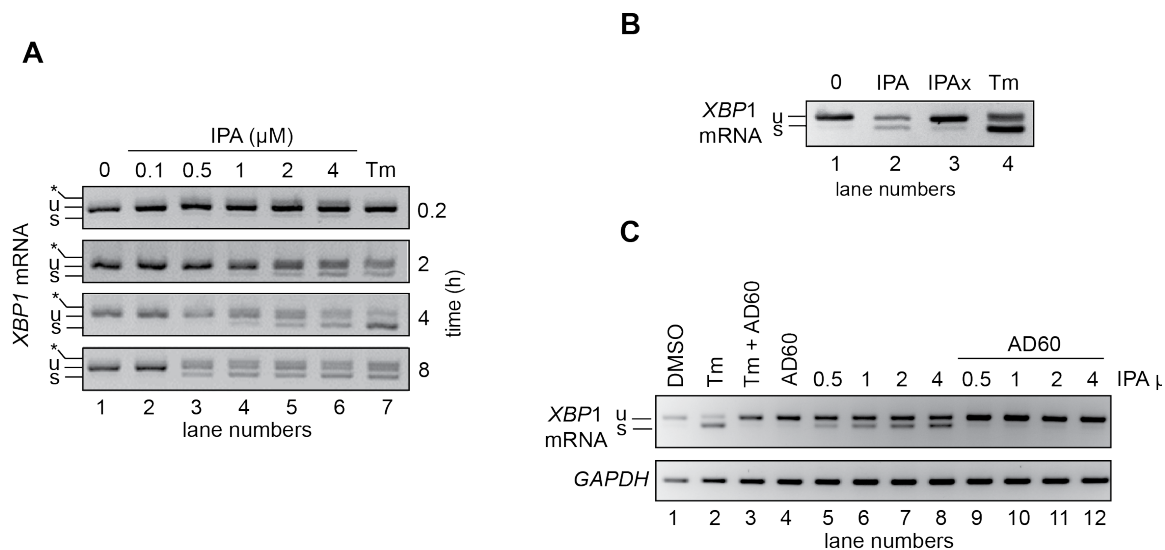


Figure 7: IPA activates the IRE1 branch of the UPR in HEK293T cells

(A) HEK293T cells were treated with increasing concentrations of IPA as a function of time. Tunicamycin (Tm, 2 $\mu\text{g}/\text{ml}$) was used as positive control to induce ER stress. The resulting *XBP1* mRNA spliced products detected by RT-PCR (“u”: unspliced and “s”: spliced) are indicated. Control cells were treated with DMSO only. The asterisk identifies a hybrid amplicon resulting from spliced and unspliced *XBP1* mRNA. (B) The effects of IPAx on the splicing of *XBP1* mRNA in HEK293T cells were detected by RT-PCR after 4 h incubation ([IPA] and [IPAx] = 2 μM). (C) Inhibition of IPA-mediated *XBP1* mRNA splicing in HEK293T cells by AD60 (incubation time = 4 h; [AD60] = 1 μM).

We next used a T-REx293 cell line, containing a genome-integrated doxycycline-inducible IRE1 α -GFP fusion gene, to monitor IRE1 α oligomerization in vivo (45). In the presence of doxycycline, IRE1 α -GFP was expressed and localized to the ER (Figure 9A). As previously described, Tm rapidly induced the relocalization of IRE1 α -GFP into discrete foci, indicative of IRE1 α oligomerization and activation (45). Furthermore, the foci dissolved by eight hours of treatment as cells attenuated IRE1 α signaling even in the presence of unmitigated ER stress (Figure 9A, upper panels). As expected, IPA

caused relocalization of IRE1 α -GFP into foci, consistent with sustained IRE1 activation (Figure 2D, lower panels). While Tm-induced foci became larger and fewer over time as previously observed, IPA-induced foci remained small and numerous. Interestingly, IPA-induced foci remained stable even at late time points, consistent with the results obtained for *XBP1* mRNA splicing (Figure 2A).

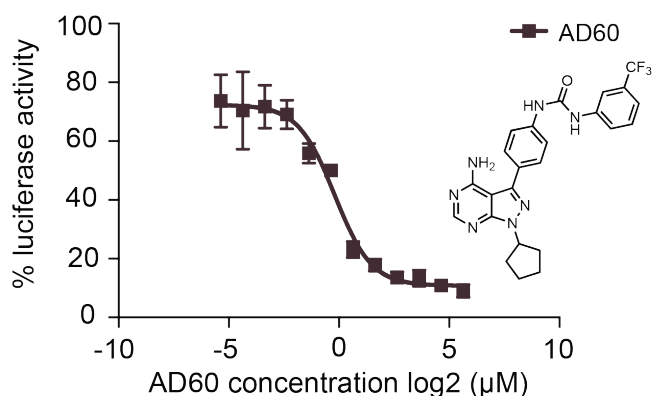


Figure 8: AD60 inhibition of XBP1-luciferase-splicing in HEK293T

A dose response of AD60 in the presences of Tm (2 μ g/m) is shown. Luciferase activity of cells treated with AD60 was normalized to cells treated with Tm only. AD60 IC₅₀ = 0.85 μ M

These results suggest that IPA-binding to IRE1 α stabilizes IRE1 α 's oligomeric state, interfering with its attenuation (45). We next tested the effect of IPA on cell viability. As shown in Figure 9B, IPA killed cells with an LD₅₀ of 0.82 μ M. This strong toxicity was surprising considering that previous studies have shown that IRE1 α has a cytoprotective role and that IRE1 α knock-out cells are viable. The result therefore is best explained by a possible off-target effect connected to ER stress, likely to be mediated through another kinase in the cell. Moreover, as the interplay between the

different UPR branches controls the switch over from cytoprotection to apoptosis (33), we next probed for possible effect of IPA on PERK and ATF6 signaling.

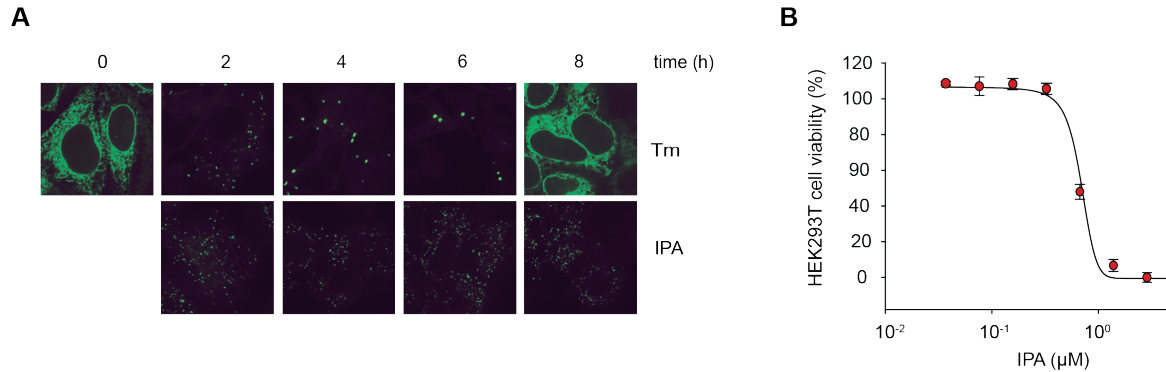


Figure 9: IPA mediated activation of IRE1 in HEK293T cells

(A) IRE1-GFP foci formation in T-REx293 cells. IRE1-GFP was visualized by confocal microscopy. (B) Effects of IPA on HEK293T cell viability ($LD_{50} = 0.83 \mu\text{M}$).

3.3 *In vivo* effects of IPA on the ATF6 and PERK UPR branches

To assess the effects of IPA on the activity of the two other UPR branches, we first examined activation of ATF6. To this end, we monitored mRNA levels by RT-PCR for two ATF6-driven transcriptional target genes, *HERP1* and *DERL3*, in HEK293T cells. As expected, treatment with Tm induced the expression of these two genes (Figure 10A and Figure 10B, lanes 6 - 9). By contrast, IPA caused no detectable induction (Figure 10A and Figure 10B, lanes 2 - 5), indicating that IPA does not induce general ER stress.

To evaluate effects of IPA on the PERK branch, we measured the phosphorylation state of PERK and eIF2 α by Western blotting. Upon activation, PERK

becomes hyperphosphorylated and displays a characteristic mobility shift in SDS-PAGE gels, as observed in cells treated with Tm (Figure 10C, lane 7). Unexpectedly, we observed that IPA also induced a shift in the mobility of PERK (Figure 10C, lanes 2 – 4). This shift, however, was only observed at low-to-intermediate concentrations (0.1, 0.5, and 1 μ M), whereas at higher concentrations (2 and 4 μ M, Figure 10C, lanes 5 and 6), PERK phosphorylation was severely diminished or not detectable. We also monitored PERK activation by phosphorylation of eIF2 α , detected with a phospho-eIF2 α -specific antibody (Figure 10C). These results paralleled those obtained for PERK phosphorylation. By contrast, equivalent concentrations of IPAx did not stimulate PERK or eIF2 α phosphorylation (Figure 10D, lane 3).

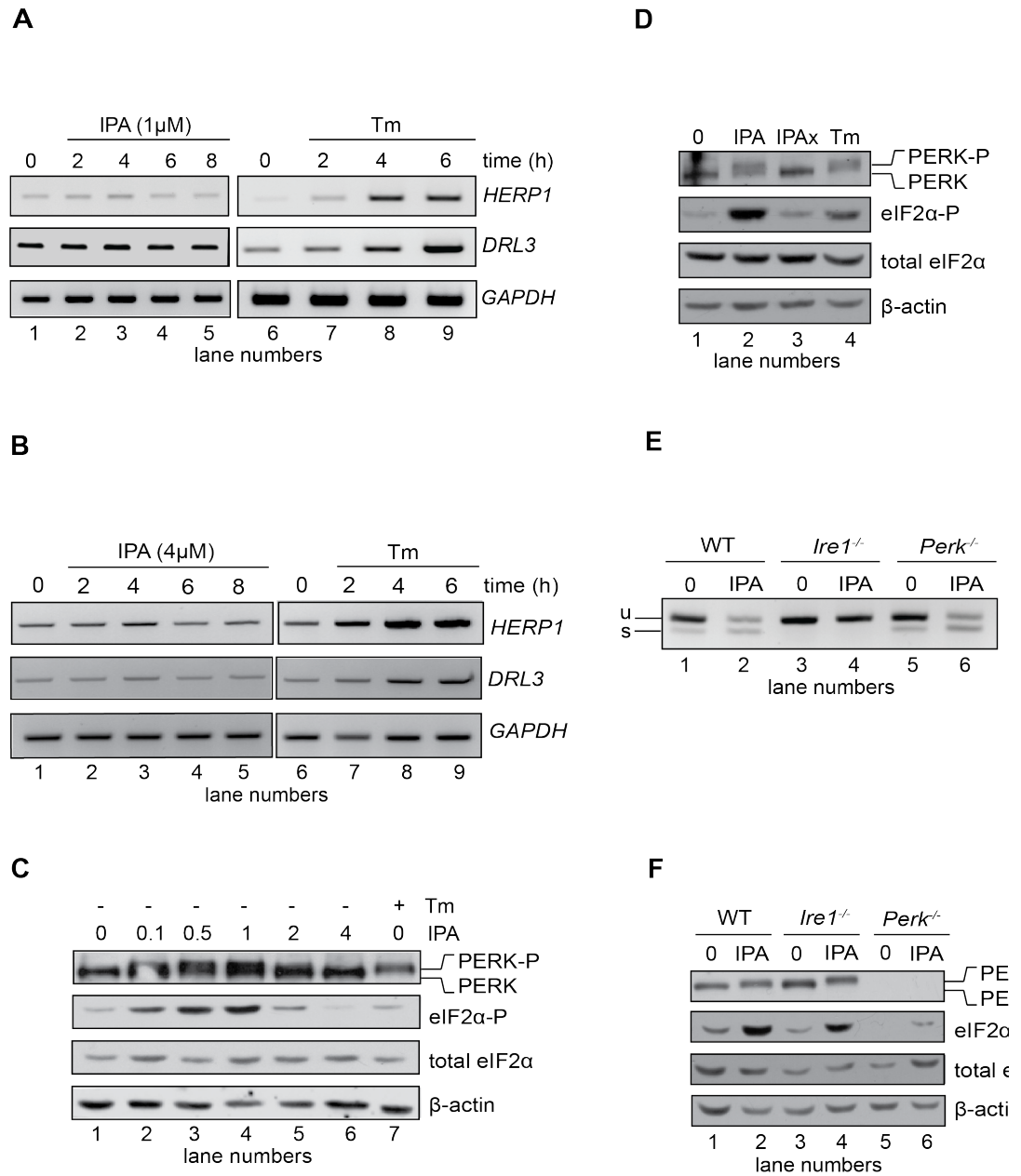


Figure 10: Effects of IPA on the ATF6 and PERK branches of the UPR

(A) The levels of ATF6 transcriptional target mRNAs *HERPUD1* (*HERP1*) and *DERLIN3* (*DRL3*) were measured by RT-PCR in HEK293T cells treated with 1 μ M IPA. GAPDH was used as a loading control. (B) Same as in (A) but cells were treated with 4 μ M IPA. (C) Phosphorylation of PERK and eIF2 α in HEK293T cells treated with IPA were detected by immunoblotting (incubation

time = 4 h); PERK phosphorylation is apparent from its shift in gel mobility; eIF2 α phosphorylation was detected using a phospho-specific antibody. β -actin was used as a loading control. (D) HEK293T cells were treated for 4 h with IPA (1 μ M), IPAx (1 μ M), or Tm (2 μ g/ml). PERK shift and eIF2 α phosphorylation were detected as in (C). (E) Wild-type (WT), *Ire1*^{-/-}, and *Perk*^{-/-} mouse embryonic fibroblast (MEFs) cells were treated with IPA (1 μ M) or Tm (5 μ g/ml) for 4 h. Induction of *XBP1* mRNA splicing by IPA was measured by RT-PCR. (F) Cells were treated as above. PERK gel mobility shift and eIF2 α phosphorylation were detected by immunoblotting.

PERK activation by IPA could be due to direct binding of IPA to PERK, or it could be caused by indirect activation of PERK by IRE1. If the latter were true, IPA should not trigger PERK activation in the absence of IRE1. To test this notion, we treated mouse embryonic fibroblasts (MEFs) derived from *Ire1* α ^{-/-} and *Perk*^{-/-} knock-out mice with IPA and monitored *XBP1* mRNA splicing, and PERK and eIF2 α phosphorylation. As in HEK293T cells, treatment of wild-type MEFs with IPA induced both the PERK and IRE1 branches of the UPR. As expected, we observed no IPA-induced *XBP1* mRNA splicing in *Ire1* α ^{-/-} MEFs (Figure 10E, lane 4) and only a trace amount of IPA-induced eIF2 α phosphorylation in *Perk*^{-/-} MEFs (Figure 10F, lane 6). By contrast, we observed no IPA-induced *XBP1* mRNA splicing, but pronounced PERK phosphorylation (indicated by its mobility shift) and eIF2 α phosphorylation in the *Ire1* α ^{-/-} knock-out MEFs. These results indicate that IPA activates the IRE1 and PERK branches of the UPR independently.

To test whether IPA binds PERK at its ATP binding site, we purified the cytosolic domain of PERK as a GST-PERK fusion protein. This preparation purified as a stable GST-PERK dimer, which in the presence of radiolabelled [γ -³²P]ATP efficiently phosphorylated eIF2 α *in vitro*. We next tested the effects of IPA and IPAx using this

kinase assay. IPA inhibited PERK the kinase reaction with an $IC_{50} = 2.8 \mu\text{M}$ (Figure 11A, solid red circles and Figure 11C). These data suggest that IPA binds to PERK directly, and likely acts as a competitive inhibitor for ATP, blocking its phosphorylation activity.

3.4 IPA activates PERK at low concentrations

The observation of IPA-induced PERK *inhibition* (shown in Figure 10C and Figure 11A) poses the conundrum of why we observed IPA-induced *activation* in the low micromolar IPA range, producing an unusual, bell-shaped dose response (Figure 10C). This behavior could be explained by a model posing that at lower IPA concentrations, IPA occupies the ATP-binding sites of a subset of PERK molecules, triggering kinase activation of neighboring, unoccupied PERK molecules, as previously shown for other kinases (50-52). At higher IPA concentrations, IPA would saturate all PERK molecules, thereby inhibiting the pathway. We treated HEK293T with both Tm and IPA, expecting that Tm would not be able to activate PERK signaling in the presence of sufficiently high IPA concentration. Indeed, at 4 μM IPA, we observed that Tm addition did not activate PERK (Figure 11B, lane 6). Moreover, at 1 μM IPA, which induces PERK activation (Figure 10C and Figure 10D), we found that Tm did not enhance the PERK mobility shift or eIF2 α phosphorylation further than what was achieved by IPA alone (Figure 11B, lane 5). IPA inhibition of PERK was reversible, since washing IPA out allowed for activation by Tm (Figure 11B, lane 9).

PERK inhibitors block IPA-induced PERK activation and restore translation

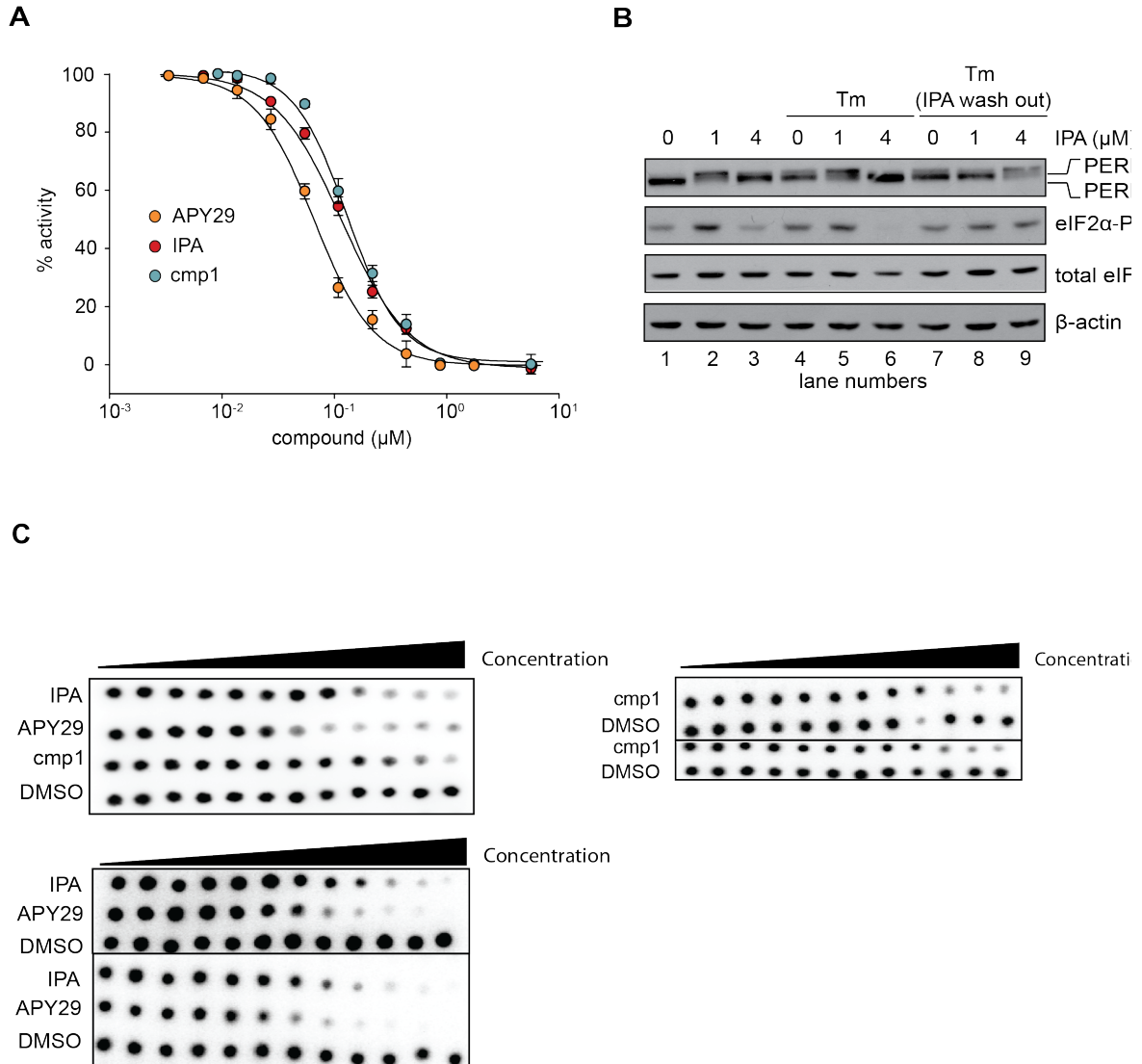


Figure 11: *In vitro* effects of IPA on GST-PERK kinase activity

(A) The effects of IPA, cmp1, and APY29 on GST-PERK kinase activity were monitored measuring phosphorylation of purified *S. cerevisiae* eIF2 α with γ -[³²P]-labeled ATP (IPA IC₅₀ = 2.8 μ M; cmp1 IC₅₀ = 3.5 μ M, APY29 IC₅₀ = 0.79 μ M). (B) HEK293T cells were pre-treated with IPA for 30 min. Cells were then either co-incubated with IPA and Tm (2 μ g/ml) for an additional 4 h (lanes 4, 5, and 6) or washed (IPA wash-out) and treated with Tm alone (lanes 7, 8, and 9). (C) A dose response of compound was used to determine the IC₅₀ values of PERK inhibition.

3.5 PERK inhibitors block IPA-induced PERK activation

We next demonstrated that it is possible to keep the PERK pathway off in the presence of IPA. To this end, we added the selective PERK inhibitor GSK2606414 (53, 54) (henceforth abbreviated as “GSK”) to HEK293T cells treated with IPA, at concentrations that exert the greatest effect on PERK pathway activation. As expected, GSK abolished IPA-induced PERK and eIF2 α phosphorylation (Figure 12A; lanes 5 and 6 and Figure 13A).

The phosphorylation of eIF2 α resulting from PERK activation inhibits translation initiation. Indeed, when we incubated HEK293T cells with IPA in the low concentration range where PERK becomes activated, incorporation of [³⁵S]-methionine into newly synthesized proteins was impaired (Figure 12B, lanes 3 and 5), consistent with translation attenuation. Interestingly, treatment with GSK restored translation to baseline levels (Figure 12B, lanes 4 and 6 and Figure 13B). This pharmacological manipulation therefore allowed us to experimentally uncouple IPA-induced IRE1 α and PERK activation. In particular, we were interested in testing whether the unexpected toxicity of IPA (Figure 9B) could, at last in part, be explained by PERK activation, which is known to induce apoptosis (33). To explore this notion, we tested cell viability at increasing IPA concentrations in the presence GSK. GSK inhibits PERK in cells with an EC₅₀ of 200 nM and shows no cell toxicity at 1 μ M (53, 55) (Figure 12C and Figure 13C). Indeed, GSK added at 1 μ M protected cells from IPA-induced cell death, shifting the LD₅₀ from 0.8 μ M to 6.2 μ M (Figure 12C). As a further control, we tested whether GSK would also

rescue cells treated with staurosporine, a rather pleiotropic kinase inhibitor. GSK had no effect under these conditions Figure 12C and Figure 13D).

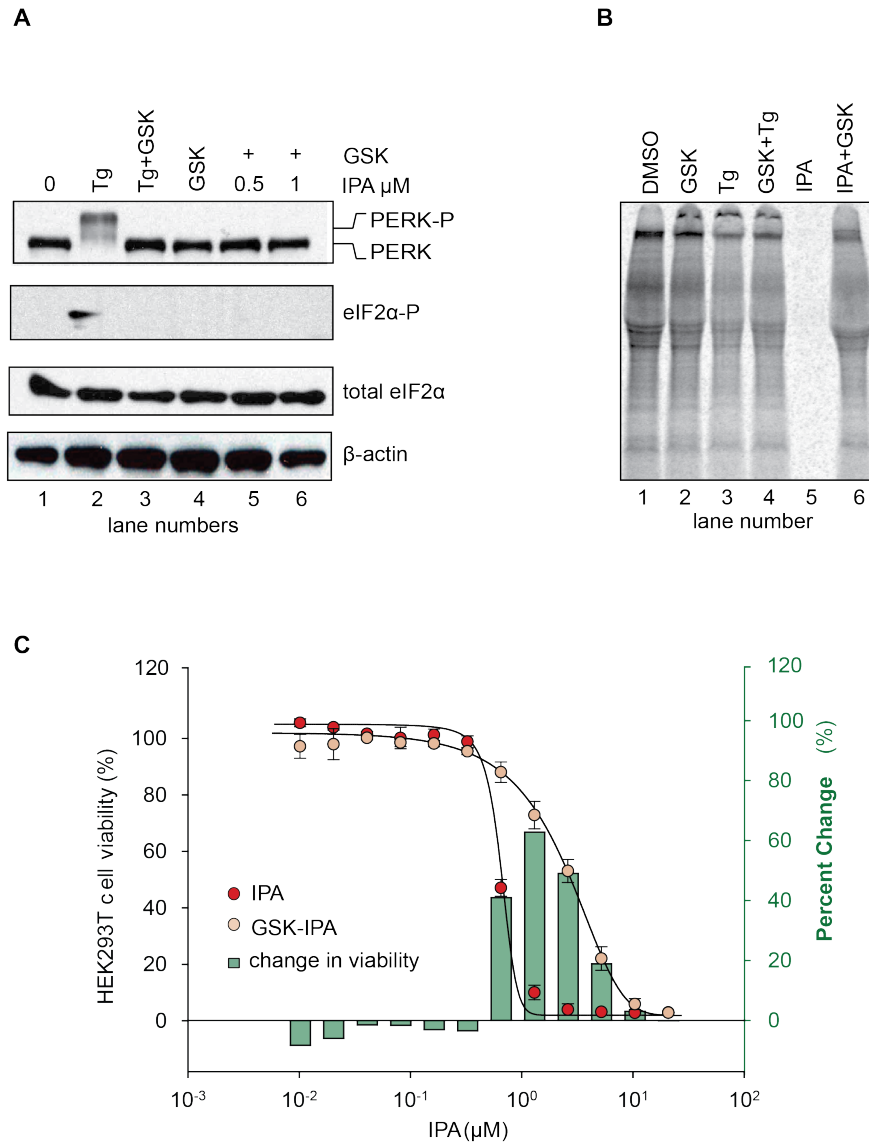


Figure 12: Inhibition of IPA-mediated PERK activation by GSK2606414

(A) Reversal of IPA-mediated PERK activation ([IPA] = 0.5 and 1 μM; lanes 5 and 6; note peak in Figure 3C at these concentrations) in combination with GSK2606414 (GSK, 1 μM) was observed using immunoblotting as described in (Figure 3C). As a control, GSK (1 μM) was used to also inhibit PERK branch activation by thapsigargin (Tg; 100 nM; lane 3). (B) HEK293T cells were

incubated with [35S] methionine to monitor protein translation upon addition of IPA (1 μM) or a combination of IPA (1 μM) and GSK (1 μM). The UPR was induced with Tg (100 nM) or DMSO as indicated. **(C)** Cotreatment of HEK293T cells with IPA+GSK. HEK293T cell viability was measured as a dose-response of IPA in combination with 1 μM of GSK (pink circles). The presence of 1 μM GSK shifted the IPA LD₅₀ from 0.82 μM to 6.21 μM . The change in cell viability +/- GSK inhibitor is overlaid on both dose responses (green bars). Cells were treated with compounds for 24 h and cell viability was normalized to DMSO controls.

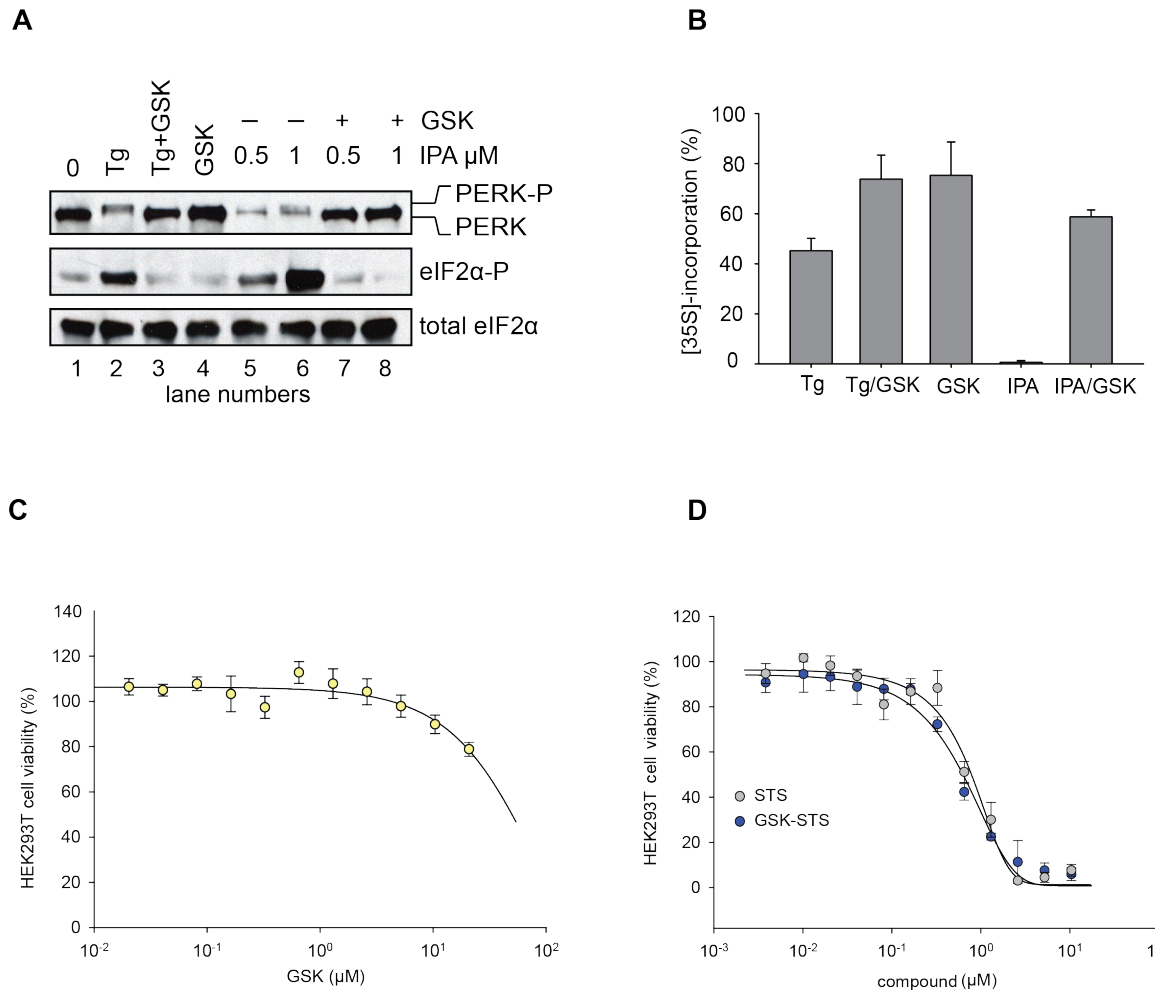


Figure 13: Effects of IPA-mediated PERK activation in HEK293T cells

(A) Reversal of IPA-mediated PERK activation ([IPA] = 0.5 and 1 μM ; lanes 7 and 8; note lanes 5 and 6 which show robust activation of the PERK pathway) in combination with GSK2606414 (GSK, 1 μM) was observed using immunoblotting as described in (Figure 10C). As a control, GSK (1 μM) was used to also inhibit PERK branch activation by thapsigargin (Tg; 100 nM; lane 3). No effect on the

pathway was observed with GSK alone (lane 4). **(B)** Quantification of [³⁵S] incorporation was performed a total of 3-time, and mean errors were derived. **(C)** A dose response of GSK was administered in HEK293T cells for 24 hours. No effect on viability was observed at 1 μM. **(D)** A dose response of staurosporine (STS) in the presence of 1 μM GSK PERK inhibitor. No change in cell viability was observed in the presence of GSK when STS was present.

To address directly whether PERK activation resulted from IPA binding to PERK itself, we recombinantly expressed the cytosolic portion of human PERK and eIF2α, the only known PERK substrate, and reconstituted the phosphorylation reaction in vitro. As shown in Figure 14A, we observed a large increase in the rate of PERK phosphorylation, which peaked at 0.5 mM IPA (3.2-fold increase over DMSO control) and then declined at higher IPA concentrations, whereas IPAx had no effect (Figure 14A and Figure 14B). The in vitro bell-shaped activity profile mimicked closely the effect observed in intact cells (Figure 3C). Furthermore using chemical crosslinking, we observed that IPA—but not its inactive analog IPAx—significantly increased PERK oligomerization, apparent as an enhanced formation of cross-linked species migrating at the size expected for PERK dimers, trimers and tetramers (Figure 15). The formation of higher-ordered PERK oligomers during ER stress was previously reported (13, 56).

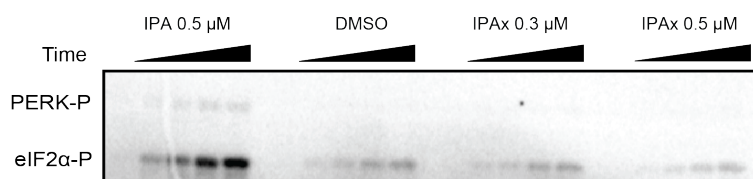
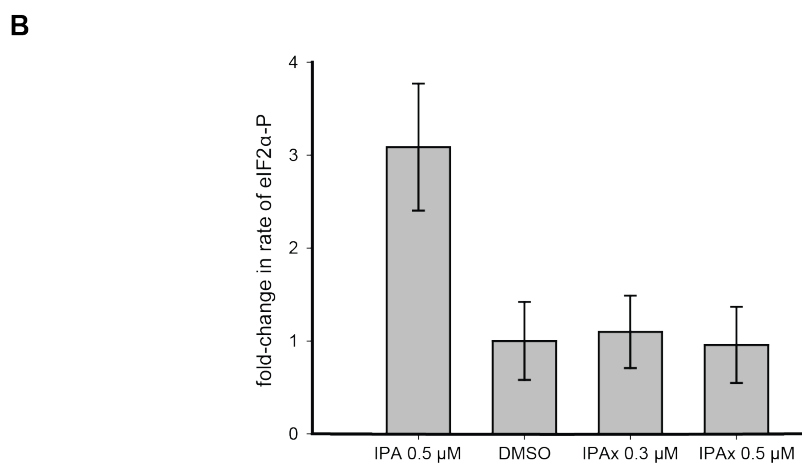
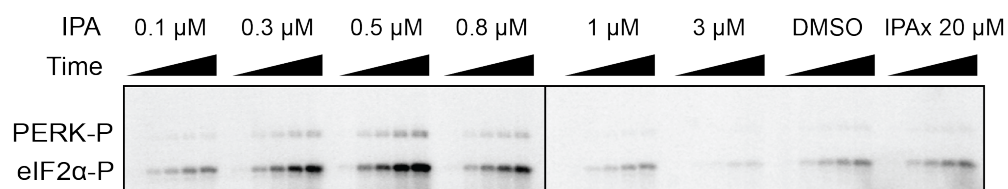
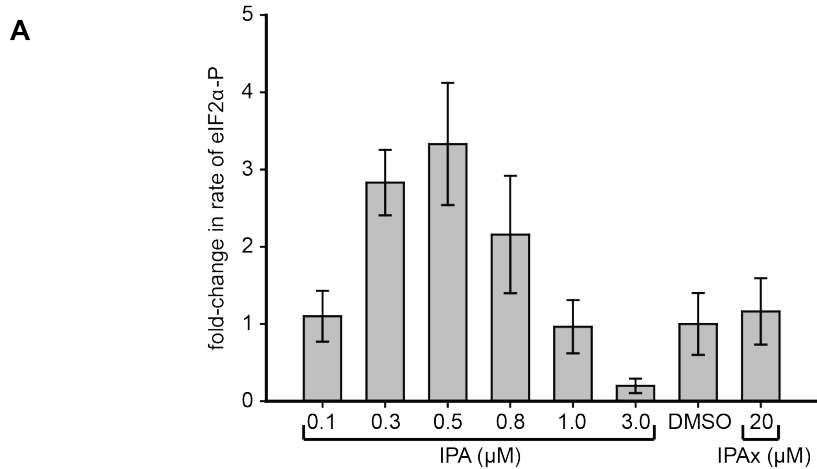


Figure 14: Reconstitution of activation of cytosolic PERK protein in vitro

(A) Recombinant PERK cytoplasmic domain was incubated at a set concentration of IPA. The fold-change in the rate of eIF2 α was normalized to the DMSO control and plotted for all concentration. The greatest effects were observed at 500 nM (3.3-fold change) and 3 μ M (0.31-fold change) in activity. IPAx showed no effect on the rate of PERK activity at a concentration of 20 μ M. (B) To test effect of IPAx on PERK activation two concentrations (0.3 and 0.5 μ M) were tested *in vitro*. The SDS-polyacrylamide gel shows the effect of IPAx on PERK activation at 0.3 and 0.5 μ M. No activation was observed when normalized to the DMSO control.

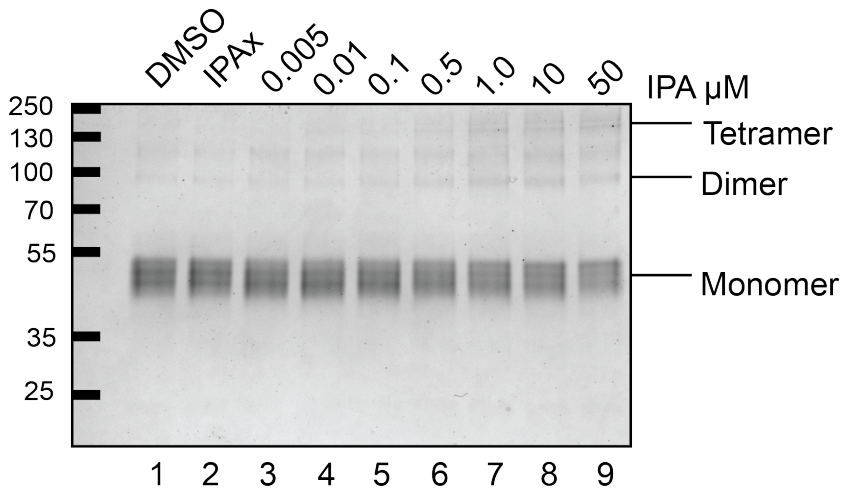


Figure 15: In vitro higher-ordered oligomerization of PERK

Recombinant PERK cytoplasmic domain (2 μ M) was preincubated with varying concentrations of IPA (or IPAx) and subjected to chemical cross-linking. An IPA-dependent increase in the dimer, trimer, and tetramer complexes was observed, whereas IPAx (50 μ M) showed no effect when compared to the DMSO control.

4 Discussion

The kinase domain of IRE1 can be targeted by small molecules to modulate its function. Based on the co-crystal structure of *S. cerevisiae* Ire1 with APY29, we developed a series of new small molecule activators, including IPA. We showed that IPA is a strong activator of IRE1 α signaling *in vitro*, by trapping IRE1 α 's kinase domain in its active (DFG/ α C-in) conformation, which promotes IRE1 oligomerization. In the oligomer, IRE1's RNase becomes activated (11, 20, 21, 42), offering the unique opportunity to read-out the conformational status of a kinase domain in the absence of phospho-transfer. Conversely, a compound, AD60, that traps IRE1's kinase domain in its inactive (DFG/ α C-out) conformation acts as an inhibitor of IRE1 signaling. Our studies confirm in mammalian cells that IRE1's kinase domain acts as a conformational switch, in which ligand binding to the ATP binding pocket—rather than enzymatic phospho-transfer—controls activity and down-stream signal transduction events (11, 20).

To rule out that IPA exerts its IRE1 activating activity by causing general ER stress, we explored its effects on the two other branches of the UPR that signal through ATF6 and PERK. Unexpectedly, we discovered that IPA also activated PERK. By contrast to IRE1 however, for which IPA drives activation *in vitro* and *in vivo* as IPA concentrations were increased, PERK activation displayed a bell-shaped dose response: PERK was *activated* at low IPA concentrations while being *inhibited* at higher ones.

The paradoxical activation of kinase signaling by kinase inhibitors was first noted for Raf kinase inhibitors almost 15 years ago (51). The observation of kinase activation in patients undergoing Raf inhibitor (vemurafenib) clinical trials then led to an intense investigation of the cellular basis for the phenomenon (50, 52). Current models suggest that drug-induced dimerization of Raf causes an increase in Raf kinase activity. This contention is supported by apo- and drug-kinase complex crystal structures, which show Raf dimers in the asymmetric crystal unit (57). Other models have been proposed that Raf inhibitor-induced Raf activation, and, to date, the critical prediction of the model that the Raf kinase inhibitor vemurafenib should induce Raf kinase activity in a purified system has resisted all attempts at biochemical reconstitution (58). This paucity in direct experimental access has forced mechanistic studies of inhibitor-induced activation to be carried out in cells, where the effects of the many components of the Ras-Raf-Mek-Erk pathway are necessarily confounding. Our work with the reconstitution of PERK's paradoxical activation by IPA shows for the first time that no other components of the kinase pathway are necessary and that inhibitor binding is sufficient for activation through the formation of homo-dimers or higher-ordered homo-oligomers (13). It was previously suggested that PERK activation is depended upon dimerization and the formation of higher-ordered oligomers (11, 12).

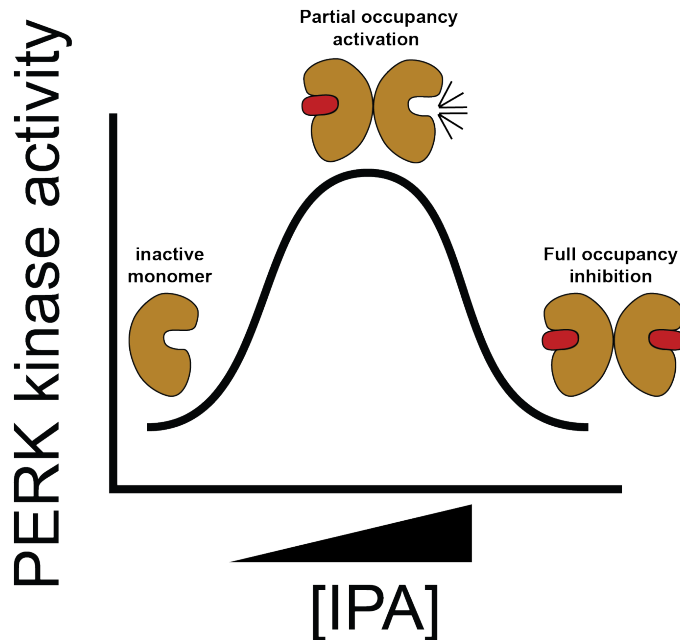


Figure 16: Proposed model for PERK activation

The mechanism of PERK activation suggests that at low concentrations of IPA PERK protein is hyper activated presumably through movements of the (DFG/ α C-in). At higher doses of IPA all active sites are filled blocking PERK's activity.

This behavior can be explained in a model in which ligand binding to a few kinase molecules biases them towards the DFG/ α C-in conformation that nucleates assembly with apo-kinases, enabling their *trans*-activation (Figure 16) Assuming a K_d of 2.8 μ M for IPA-binding to PERK as determined by PERK inhibition (Figure 4A), we estimate that approximately 15% of the PERK molecules are occupied by IPA under assay conditions that yield maximal activation. Since PERK•IPA triggered activation of unoccupied apo-PERK molecules would bias their conformation towards the active state and hence is likely to enhance their affinity for the inhibitor, the estimate of IPA-

occupancy in the population defines an upper limit. This back-of-the-envelope calculation therefore suggests that PERK may form oligomers larger than dimers, in which one PERK•IPA may suffice to activate more than one apo-PERK. At low concentrations of IPA, heterodimers of PERK•IPA/PERKapo, or perhaps larger oligomers of PERK•IPA/[PERKapo]_n, where all PERK molecules are in the active DFG/αC-in conformation, are active in phospho-transfer. At higher, saturating IPA doses, all PERK molecules would be occupied by IPA and thus inhibited through competition with ATP binding.

Thus, the PERK/IPA enzyme/ligand combination mimics the RAF/vemurafenib combination and broadens the number of examples where an ATP-competitive binder can activate rather than inhibit a kinase. This mode of kinase regulation, now documented for two different protein kinases, may be more widespread than currently appreciated. Indeed, we observed a small amount of activation of eIF2α phosphorylation in PERK^{-/-} cells (Figure 3F, lane 6), indicating that at least one of the other known eIF2a kinases (GCN2, HRI, and PKR) (59, 60) may be similarly regulated. Kinase activation by partial occupancy of the active site, therefore, may be an important consideration in dosing kinase inhibitors for therapeutic applications, imposing a “minimal tolerable dose” below which potential drugs may exert detrimental effects that oppose the desired therapy. This dangerous scenario may result from many kinase inhibitors that bind and stabilize kinases in the DFG/αC -in conformation.

Based on the observation that ATF6 was not activated in cells treated with IPA, we conclude that IPA-mediated activation of IRE1 and PERK occurred in the absence of

ER stress. This property contrasts with that of the previously described activator 1NM-PP1, which binds in the ATP binding pocket to IRE1-as, the cognate, analog-sensitized allele (44). Activation of IRE1-as by 1NM-PP1 requires the additional induction of ER stress, or overproduction of IRE1-as driving IRE1-as oligomerization by mass action (21). IPA therefore presents a unique pharmacological tool with which activation of wild-type IRE1 can be studied in living cells directly in the absence of ER stress.

The select application of combinations of UPR modulators has allowed us to begin dissecting the individual contributions of the signaling branches of the UPR. In particular, we have shown that the lethality that IPA displays at high doses can be partially overcome if the PERK pathway is inactivated using a selective PERK inhibitor, GSK, increasing the EC₅₀ with which IPA drives cells into apoptosis by about an order of magnitude. This observation is consistent with the proposed roles of both the IRE1 and PERK branches, providing cytoprotective and pro-apoptotic outputs, respectively (33). IPA, AD60, and other compounds developed to date therefore provide a stepping-stone towards developing novel methodologies for the selective pharmacological tuning of the UPR. Diseases, such as multiple myeloma, a cancer of highly secretory plasma cells where the UPR is thought to play a major cytoprotective role (61, 62), or triple-negative breast cancer, in which high XBP1 activity has been correlated with poor patient prognosis (61, 63), have exposed the potential significance of targeting the UPR in cancers (64). Furthermore, recent studies in Parkinson's disease model systems have revealed the potential for small molecule activators of the UPR in stopping the progression of the disease (65). Additionally, mutations found in cancer cells that

weaken IRE1 α RNase activity may be amenable targets for allosteric modulation. The chemical biology tools developed in this work provide an important step forward towards exploring the utility of UPR-based therapies, as well as offer fundamental mechanistic insights into a key mechanism that keeps the healthy balance of protein folding in the ER.

5 Contributions

ASM, JA and MAMS contributed equally to this work. ASM, JA and MAMS conceived and designed experiments with SB, KMS and PW. ASM and ACD performed chemical synthesis and characterization, ASM performed *in vitro* biochemical measurements and cell drug combinations. JA and MAMS performed in cell characterization of IPA. HL performed imaging of IRE1 foci. KG provided PERK-GST fusion protein and eIF2 α . EM, KG, DAA and AVK helped with analysis. CS and DAA generated the XBP1 reporter cell line. ASM, KMS and PW wrote the manuscript with input from all authors.

6 Work Cited

1. A. M. Reimold *et al.*, Plasma cell differentiation requires the transcription factor XBP-1. *Nature* **412**, 300-307 (2001).
2. A. H. Lee, G. C. Chu, N. N. Iwakoshi, L. H. Glimcher, XBP-1 is required for biogenesis of cellular secretory machinery of exocrine glands. *The EMBO journal* **24**, 4368-4380 (2005).
3. Y. Ma, L. M. Hendershot, The stressful road to antibody secretion. *Nature immunology* **4**, 310-311 (2003).
4. K. Mori, W. Ma, M. J. Gething, J. Sambrook, A transmembrane protein with a cdc2+/CDC28-related kinase activity is required for signaling from the ER to the nucleus. *Cell* **74**, 743-756 (1993).
5. P. Walter, D. Ron, The unfolded protein response: from stress pathway to homeostatic regulation. *Science* **334**, 1081-1086 (2011).
6. J. S. Cox, C. E. Shamu, P. Walter, Transcriptional induction of genes encoding endoplasmic reticulum resident proteins requires a transmembrane protein kinase. *Cell* **73**, 1197-1206 (1993).
7. C. Sidrauski, J. S. Cox, P. Walter, tRNA ligase is required for regulated mRNA splicing in the unfolded protein response. *Cell* **87**, 405-413 (1996).
8. T. Aragon *et al.*, Messenger RNA targeting to endoplasmic reticulum stress signalling sites. *Nature* **457**, 736-740 (2009).

9. J. J. Credle, J. S. Finer-Moore, F. R. Papa, R. M. Stroud, P. Walter, On the mechanism of sensing unfolded protein in the endoplasmic reticulum. *Proceedings of the National Academy of Sciences of the United States of America* **102**, 18773-18784 (2005).
10. A. V. Korennykh *et al.*, Cofactor-mediated conformational control in the bifunctional kinase/RNase Ire1. *BMC biology* **9**, 48 (2011).
11. A. V. Korennykh *et al.*, The unfolded protein response signals through high-order assembly of Ire1. *Nature* **457**, 687-693 (2009).
12. A. V. Korennykh *et al.*, Structural and functional basis for RNA cleavage by Ire1. *BMC biology* **9**, 47 (2011).
13. A. Bertolotti, Y. Zhang, L. M. Hendershot, H. P. Harding, D. Ron, Dynamic interaction of BiP and ER stress transducers in the unfolded-protein response. *Nature cell biology* **2**, 326-332 (2000).
14. J. Zhou *et al.*, The crystal structure of human IRE1 luminal domain reveals a conserved dimerization interface required for activation of the unfolded protein response. *Proceedings of the National Academy of Sciences of the United States of America* **103**, 14343-14348 (2006).
15. D. Pincus *et al.*, BiP binding to the ER-stress sensor Ire1 tunes the homeostatic behavior of the unfolded protein response. *PLoS biology* **8**, e1000415 (2010).
16. B. M. Gardner, P. Walter, Unfolded proteins are Ire1-activating ligands that directly induce the unfolded protein response. *Science* **333**, 1891-1894 (2011).

17. A. Chawla, S. Chakrabarti, G. Ghosh, M. Niwa, Attenuation of yeast UPR is essential for survival and is mediated by IRE1 kinase. *The Journal of cell biology* **193**, 41-50 (2011).
18. F. R. Papa, C. Zhang, K. Shokat, P. Walter, Bypassing a kinase activity with an ATP-competitive drug. *Science* **302**, 1533-1537 (2003).
19. C. Rubio *et al.*, Homeostatic adaptation to endoplasmic reticulum stress depends on Ire1 kinase activity. *The Journal of cell biology* **193**, 171-184 (2011).
20. A. S. Mendez *et al.*, Endoplasmic reticulum stress-independent activation of unfolded protein response kinases by a small molecule ATP-mimic. *eLife* **4**, (2015).
21. L. Wang *et al.*, Divergent allosteric control of the IRE1alpha endoribonuclease using kinase inhibitors. *Nature chemical biology* **8**, 982-989 (2012).
22. R. L. Wiseman *et al.*, Flavonol activation defines an unanticipated ligand-binding site in the kinase-RNase domain of IRE1. *Molecular cell* **38**, 291-304 (2010).
23. J. Jurkin *et al.*, The mammalian tRNA ligase complex mediates splicing of XBP1 mRNA and controls antibody secretion in plasma cells. *The EMBO journal* **33**, 2922-2936 (2014).
24. Y. Lu, F. X. Liang, X. Wang, A synthetic biology approach identifies the mammalian UPR RNA ligase RtcB. *Molecular cell* **55**, 758-770 (2014).
25. W. Cui, J. Li, D. Ron, B. Sha, The structure of the PERK kinase domain suggests the mechanism for its activation. *Acta crystallographica. Section D, Biological crystallography* **67**, 423-428 (2011).

26. A. C. Dar, T. E. Dever, F. Sicheri, Higher-order substrate recognition of eIF2alpha by the RNA-dependent protein kinase PKR. *Cell* **122**, 887-900 (2005).
27. M. Dey, C. Cao, F. Sicheri, T. E. Dever, Conserved intermolecular salt bridge required for activation of protein kinases PKR, GCN2, and PERK. *The Journal of biological chemistry* **282**, 6653-6660 (2007).
28. S. R. Nallagatla, R. Toroney, P. C. Bevilacqua, Regulation of innate immunity through RNA structure and the protein kinase PKR. *Current opinion in structural biology* **21**, 119-127 (2011).
29. C. Koumenis, ER stress, hypoxia tolerance and tumor progression. *Current molecular medicine* **6**, 55-69 (2006).
30. K. Kohno, Stress-sensing mechanisms in the unfolded protein response: similarities and differences between yeast and mammals. *Journal of biochemistry* **147**, 27-33 (2010).
31. X. Zhang, J. Gureasko, K. Shen, P. A. Cole, J. Kuriyan, An allosteric mechanism for activation of the kinase domain of epidermal growth factor receptor. *Cell* **125**, 1137-1149 (2006).
32. D. O. Morgan, Cyclin-dependent kinases: engines, clocks, and microprocessors. *Annual review of cell and developmental biology* **13**, 261-291 (1997).
33. J. H. Lin *et al.*, IRE1 signaling affects cell fate during the unfolded protein response. *Science* **318**, 944-949 (2007).
34. M. Calfon *et al.*, IRE1 couples endoplasmic reticulum load to secretory capacity by processing the XBP-1 mRNA. *Nature* **415**, 92-96 (2002).

35. H. P. Harding, Y. Zhang, D. Ron, Protein translation and folding are coupled by an endoplasmic-reticulum-resident kinase. *Nature* **397**, 271-274 (1999).
36. R. C. Wek, H. Y. Jiang, T. G. Anthony, Coping with stress: eIF2 kinases and translational control. *Biochemical Society transactions* **34**, 7-11 (2006).
37. H. P. Harding *et al.*, Regulated translation initiation controls stress-induced gene expression in mammalian cells. *Molecular cell* **6**, 1099-1108 (2000).
38. D. J. Maly, F. R. Papa, Druggable sensors of the unfolded protein response. *Nature chemical biology* **10**, 892-901 (2014).
39. A. C. Dar, K. M. Shokat, The evolution of protein kinase inhibitors from antagonists to agonists of cellular signaling. *Annual review of biochemistry* **80**, 769-795 (2011).
40. A. Joshi *et al.*, Molecular mechanisms of human IRE1 activation through dimerization and ligand binding. *Oncotarget* **6**, 13019-13035 (2015).
41. R. Ghosh *et al.*, Allosteric inhibition of the IRE1alpha RNase preserves cell viability and function during endoplasmic reticulum stress. *Cell* **158**, 534-548 (2014).
42. M. Sanches *et al.*, Structure and mechanism of action of the hydroxy-aryl-aldehyde class of IRE1 endoribonuclease inhibitors. *Nature communications* **5**, 4202 (2014).
43. D. Han *et al.*, IRE1alpha kinase activation modes control alternate endoribonuclease outputs to determine divergent cell fates. *Cell* **138**, 562-575 (2009).

44. D. Han *et al.*, A kinase inhibitor activates the IRE1alpha RNase to confer cytoprotection against ER stress. *Biochemical and biophysical research communications* **365**, 777-783 (2008).
45. H. Li, A. V. Korennykh, S. L. Behrman, P. Walter, Mammalian endoplasmic reticulum stress sensor IRE1 signals by dynamic clustering. *Proceedings of the National Academy of Sciences of the United States of America* **107**, 16113-16118 (2010).
46. P. E. Harrington *et al.*, Unfolded Protein Response in Cancer: IRE1alpha Inhibition by Selective Kinase Ligands Does Not Impair Tumor Cell Viability. *ACS medicinal chemistry letters* **6**, 68-72 (2015).
47. P. W. Alexei Korennykh, Avin C. Dar, Kevan M. Shokat in *University of California S. F. university of California*, Ed. (USA, 2012).
48. A. C. Dar, M. S. Lopez, K. M. Shokat, Small molecule recognition of c-Src via the Imatinib-binding conformation. *Chemistry & biology* **15**, 1015-1022 (2008).
49. A. Korennykh, P. Walter, Structural basis of the unfolded protein response. *Annual review of cell and developmental biology* **28**, 251-277 (2012).
50. P. I. Poulikakos, C. Zhang, G. Bollag, K. M. Shokat, N. Rosen, RAF inhibitors transactivate RAF dimers and ERK signalling in cells with wild-type BRAF. *Nature* **464**, 427-430 (2010).
51. C. A. Hall-Jackson *et al.*, Paradoxical activation of Raf by a novel Raf inhibitor. *Chemistry & biology* **6**, 559-568 (1999).

52. G. Hatzivassiliou *et al.*, RAF inhibitors prime wild-type RAF to activate the MAPK pathway and enhance growth. *Nature* **464**, 431-435 (2010).
53. J. M. Axten *et al.*, Discovery of 7-methyl-5-(1-[[3-(trifluoromethyl)phenyl]acetyl]-2,3-dihydro-1H-indol-5-yl)-7H-pyrrolo[2,3-d]pyrimidin-4-amine (GSK2606414), a potent and selective first-in-class inhibitor of protein kinase R (PKR)-like endoplasmic reticulum kinase (PERK). *Journal of medicinal chemistry* **55**, 7193-7207 (2012).
54. J. Krishnamoorthy *et al.*, Evidence for eIF2alpha phosphorylation-independent effects of GSK2656157, a novel catalytic inhibitor of PERK with clinical implications. *Cell cycle* **13**, 801-806 (2014).
55. J. A. Moreno *et al.*, Oral treatment targeting the unfolded protein response prevents neurodegeneration and clinical disease in prion-infected mice. *Science translational medicine* **5**, 206ra138 (2013).
56. S. J. Marciniak, L. Garcia-Bonilla, J. Hu, H. P. Harding, D. Ron, Activation-dependent substrate recruitment by the eukaryotic translation initiation factor 2 kinase PERK. *The Journal of cell biology* **172**, 201-209 (2006).
57. T. Rajakulendran, M. Sahmi, M. Lefrancois, F. Sicheri, M. Therrien, A dimerization-dependent mechanism drives RAF catalytic activation. *Nature* **461**, 542-545 (2009).
58. M. Holderfield *et al.*, RAF inhibitors activate the MAPK pathway by relieving inhibitory autophosphorylation. *Cancer cell* **23**, 594-602 (2013).

59. T. Chen *et al.*, Chemical genetics identify eIF2alpha kinase heme-regulated inhibitor as an anticancer target. *Nature chemical biology* **7**, 610-616 (2011).
60. H. P. Harding *et al.*, Bioactive small molecules reveal antagonism between the integrated stress response and sterol-regulated gene expression. *Cell metabolism* **2**, 361-371 (2005).
61. X. Chen *et al.*, XBP1 promotes triple-negative breast cancer by controlling the HIF1alpha pathway. *Nature* **508**, 103-107 (2014).
62. A. Hosoda, M. Tokuda, R. Akai, K. Kohno, T. Iwawaki, Positive contribution of ERdj5/JPDI to endoplasmic reticulum protein quality control in the salivary gland. *The Biochemical journal* **425**, 117-125 (2010).
63. D. R. Carrasco *et al.*, The differentiation and stress response factor XBP-1 drives multiple myeloma pathogenesis. *Cancer cell* **11**, 349-360 (2007).
64. C. Hetz, B. Mollereau, Disturbance of endoplasmic reticulum proteostasis in neurodegenerative diseases. *Nature reviews. Neuroscience* **15**, 233-249 (2014).
65. C. Hetz, E. Chevet, S. A. Oakes, Proteostasis control by the unfolded protein response. *Nature cell biology* **17**, 829-838 (2015).
66. A. V. Statsuk *et al.*, Tuning a three-component reaction for trapping kinase substrate complexes. *Journal of the American Chemical Society* **130**, 17568-17574 (2008).

7 Material and Methods

7.1 Cell Culture

HEK293T, T-REx293 and wild type, *Ire1^{-/-}* and *Perk^{-/-}* cells MEF cells were maintained at 37°C, 5% CO₂ in Dulbecco's Modified Eagle Medium (DMEM) supplemented with 10% Fetal Bovine Serum (FBS), 10 units/ml penicillin and 10 µg/ml streptomycin (Life technologies). Tunicamycin was obtained from Sigma. Transient and stable transfections were performed using the Lipofectamine 2000 (Invitrogen) and FuGene6 reagent (Roche). Stable cell lines expressing IRE1-3F6HGFP T-REx293 were described previously (45).

7.2 Live cell imaging

T-REx293 cells were split two days before imaging onto glass-bottom micro-well dishes (MatTek) at 5×10^4 cells/dish. Doxycyclin-containing medium (10 nM doxycycline) was added for 24 h, withdrawn before imaging and replaced with imaging media (Hank's Balanced Salt Solution (GIBCO), 2% FBS, and 5 mM HEPES pH 7.0). Images were acquired on a spinning-disk confocal microscope as described (45).

7.3 Metabolic labeling

HEK293T cells (500,000 cells/ml) were plated in 12-well flat bottom culture cluster dishes (Costar) 24 hours before the experiment. IPA (1 µM), or a combination of

IPA with GSK2606414, were added to the cells culture for no longer than 2 hours. Fifteen minutes prior to lysing cells, 4 μCi of Express [^{35}S] protein-labeling mix (Perkin-Elmer) was added. Media was removed, and cells were immediately lysed in a buffer containing 25 mM Tris-HCl pH 8, 8 mM MgCl_2 , 1 mM dithiothreitol (DTT), 1% Triton X-100, 15% glycerol, 10 mM leupeptin, 153 μM aprotinin and 1 mM phenylmethanesulfonyl fluoride. Cells lysates were kept on ice for 30 minutes before high-speed centrifugation followed by denaturation at 95 C. The samples were resolved on a SDS-polyacrylamide gel which were then stained with Coomassie blue to ascertain protein loading. Dry gels were exposed to a blank phosphorscreen and scanned using a Typhoon variable mode imager (GE Healthcare). The resulting autoradiograms were quantified using ImageQuant software (Molecular Dynamics).

7.4 Cell viability assays

HEK293T cells were grown in DMEM (Sigma) complete media containing 10% FBS, 10 units/ml penicillin (Invitrogen) and 10 $\mu\text{g/ml}$ streptomycin (Invitrogen). Cells were plated at a density of 30,000 cells per well in 96-well black plates with clear flat bottoms (Corning) 24 h before the experiment. A 12-point semi-logarithmic dilution series of compounds was made starting at 30 μM not to exceed 0.1% DMSO after final dilution into the growth media. Viability assays were conducted over the course of 24 h. Cell viability was determined using CellTiter-Blue (Promega) following the manufacturer's instructions. A Spectramax5 Microplate reader equipped with SoftMax

Pro 5 software (Molecular Devices) was used to read out viability and data were plotted using SigmaPlot software package (Systat Software). Experiments were done in triplicate and mean values were computed for each data point.

7.5 RNA isolation and RT-PCR

Cells were lysed and total RNA was collected (Total RNA Kit 1, EZ-RNA, EZNA (USA)). PolyA⁺ mRNA was reverse transcribed with M-MLV (Invitrogen) and the resulting cDNA was used as template for PCR amplification across the fragment of *XBP1* cDNA containing the intron. Primers used to amplify human *XBP1*: 5'-TTACGAGAGAAAACATCATGGC - 3' and 5'-GGGTCCAAGTTGTCCAGAATGC - 3'. To amplify murine *XBP1*: 5'-GAACCAGGAGTTAAGAACACG - 3' and 5'-AGGCAACAGTGTGCGAGTCC - 3'. PCR conditions were as follows: 95°C for 5 min, 95°C for 1 min, 58°C for 30 s, 72°C for 30 s, and 72°C for 5 min, with 35 cycles of amplification. PCR products were resolved on a 2.5% agarose tris-acetate EDTA (TAE) gel. As previously reported, a hybrid amplicon species consisting of unspliced Xbp-1 annealed to spliced Xbp-1 can also be produced through this PCR reaction and was visible as a slower migrating band above the unspliced amplicon. The same cDNA was used as template for PCR of DERLIN-3 and HERPUD1, both ATF6 targets, and GAPDH, which was used as loading control. Primers used included the following: DERLIN-3, 5'-AGTTCCAACCTCTTTGATGGAGGGCA- 3' and 5'-AGCCAGCTGTGAGGAATATGGGAA - 3'; HERPUD1-1, 5'-ACAAGGTGGCCCTATTGTGGAAGA- 3' and 5'-AGTCCATTCCTGTCAAAGCCTCCA -

3'; GAPDH, 5' CCATGTTTCGTCATGGGTGTGA- 3' and 5'-
CATGGACTGTGGTCATGAGT - 3'. PCR conditions were: 95°C x 5 min, 95°C x 1 min,
56°C x 30 s, 72°C for 30 s for 30 cycles, 72°C for 5 min at 4°C. PCR products were
resolved on a 2% agarose TAE gel.

7.6 Protein expression and purification

7.6.1 IRE1 α -KR43

Human IRE1 α -KR43 tagged with a hexa-histidine (6xHis) tag in its N-terminus was expressed and purified in SF21 cells as described(45). Cells were lysed in buffer containing 20 mM Tris-HCl, pH 7.5, 600 mM NaCl, 2 mM MgCl₂, 3 mM imidazole, 10% glycerol, 1% Triton X-100, 3 mM β -mercaptoethanol, COMPLETE protease inhibitors (Roche), and PhosSTOP phosphatase inhibitor cocktail (Roche) and passed through an AVESTIN emulsiflex-C3 3x times for complete lysis. The lysate was cleared using centrifugation at 100,000 x *g*. Clear lysate was allowed to incubate on Ni-NTA agarose (Qiagen) beads for 2 hours before being washed 3x times with buffer containing 20 mM Tris-HCl, pH7.5, 600 mM NaCl, 2 mM MgCl₂, 30 mM imidazole, 10% glycerol and 3 mM β -mercaptoethanol. Protein was eluted from the column by raising the imidazole concentration to 250 mM. The eluate was then passed through a HiTrap desalting column (GE Healthcare). Lastly, the 6xHis was cleaved as described(45) and the resulting protein was then loaded onto a HisTrap HP, 5 x 5 ml column to remove the uncleaved protein. The cleaved protein was then loaded on a Mono-S 5/50 GL column

(GE Healthcare), and the eluate was then concentrated to 5 mg/ml and loaded on a Superdex 200 HR 10/300 (GE Healthcare) column in buffer containing 20 mM Tris-HCl pH 7.5, 250 mM NaCl, 10% Glycerol and 0.5 mM tris (2-carboxyethyl) phosphine (TCEP). The pure protein solution was aliquoted and stored at -80°C.

7.6.2 PERK (580-1077aa) murine

To express the cytosolic kinase domain of PERK, the murine PERK kinase domain (580-1077aa) was cloned into a pGEX4T1 vector to create a fusion protein containing N-terminal GST. The plasmid was transformed into *E. coli* strain BL21DE3 (RIPL). Cells were grown in LB medium containing ampicillin and chloramphenicol until OD600 = 0.6. Expression was induced with 0.2 mM IPTG at 18°C for 16 hours. Cells were harvested by centrifugation, resuspended in buffer A (50 mM Tris pH 7.5, 150 mM NaCl, 5 mM MgCl₂, 3 mM β-mercaptoethanol, 2.5% Glycerol) and lysed by sonication. After centrifugation, the supernatant was applied to a GST-Sepharose column and washed with buffer A and buffer A containing 500 mM KCl and 1 mM ATP. Sample was eluted with buffer A containing 20 mM glutathione. GST-PERK kinase domain was then concentrated and further purified on a Superdex 200 10/300 gel filtration column equilibrated in buffer B (50 mM Tris pH 7.5, 50 mM NaCl, 5 mM MgCl₂, 3 mM DTT, 1% Glycerol). Fractions containing GST-PERK kinase domain were concentrated and flash-frozen in liquid nitrogen and stored at -80°C.

7.6.3 PERK mammalian (535-1093 Δ660-868)

Full-length cytosolic human PERK was codon-optimized for *E. coli* expression by Genewiz Inc. A construct was then cloned into a Pgex-6p-2 vector for expression using two rounds of In-Fusion cloning (Clontech) (535-1093 Δ660-868). The cytosolic portion of PERK, lacking the unstructured loop region (amino acids 535-1093 Δ660-868) was then co-expressed with a tagless lambda phosphatase to produce a fully dephosphorylated PERK protein in BL21 star (DE3) (Life Technologies) (53). Cells were grown to an OD600 of 0.5 before induction with 0.1 mM IPTG at 15°C for 25 h. Cells were harvested and lysed using AVESTIN Emulsiflex-C3 in a buffer containing 50 mM Tris-HCl, pH 8.0, 500 mM NaCl, 5% glycerol, 5 mM TCEP (buffer A) and EDTA-free COMPLETE protease inhibitor cocktail (Roche). Lysate was cleared by centrifugation at 100,000 x g before batch binding to a GST-Sepharose resin. The resin was washed 5x times with buffer A, and on-column tag cleavage was performed using PreScission protease (GE Healthcare). The protein was loaded onto a HiTrap Q HP column to remove remaining protease. The PERK (535-1093 Δ660-868) protein was then concentrated and fractionated on a Superdex 200 GL (GE Healthcare) to remove uncleaved GST-PERK protein.

7.7 Immunoblotting

Cells were lysed in 50 mM Tris-HCl, 2% SDS, 10% glycerol, 0.01% bromophenol blue, pH 6.8 with supplemented with phosphatase inhibitors (Sigma) and protease

inhibitors (Roche). 30 to 50 μ g of total protein was loaded on each lane of 8% or 10% SDS-PAGE gels. The separated proteins were then transferred onto nitrocellulose membranes for immunoblotting. The following antibodies and dilutions were used: anti- β -actin 1:10,000 (A5441, Sigma), anti-total PERK at 1:1000 (C33E10, Cell Signaling Technology), anti-phospho eIF2 α at 1:1,000 (3597S, Cell Signaling Technology), anti-total eIF2 α at 1:1,000 (L57A5, Cell Signaling Technology). After overnight incubation with primary antibody, membranes were washed in PBS with 0.05% Tween and incubated in HRP-coupled secondary antibody anti-rabbit (611-1302, Rockland) or anti-mouse (610-1302, Rockland) diluted at 1:5,000 in wash buffer. Immunoreactive bands were detected by chemiluminescence.

7.8 In vitro endoribonuclease IRE1 α activity assay

IRE1 endoribonuclease activity was detected employing two in vitro assays. *k*_{obs} and Hill coefficients were determined from the cleavage kinetics of [³²P]-labeled RNA substrates as previously described (49). EC₅₀ values were determined using a FRET-based cleavage assay. A FRET probe (FRET_IDT_17 56-FAM/rCrArCrCrUrCrUrGrCrArGrCrArGrGrUrG/IABIk_FQ) was purchased from IDT (RNase free HPLC purification) and dissolved in RNase-free H₂O. Excitation: 485 (480-490) and emission: 517 (512-520). The reactions were started by addition of RNA FRET probe (to a final concentration of 100 nM) to 9.4 ml of premixture containing 20 mM HEPES, pH 7.4, 70 mM NaCl, 2 mM MgCl₂, 4 mM DTT, 5% glycerol, and compound in

DMSO not to exceed 1%. Reactions were performed at 30°C and contained 150 nM enzyme under single turnover conditions. Reactions were quenched at time intervals with equal volumes of formamide. Samples were analyzed using a SpectraMax M5 plate reader equipped with SoftMax® Pro 5 and data acquisition software (Molecular Devices). The data were plotted using SigmaPlot software package (Systat Software). Experiments were repeated 3-4 times and mean values were computed.

7.9 Generation of XBP1 reporter cell line

A plasmid encoding a modified ER stress reporter construct consisting of a C-terminally FLAG-tagged firefly luciferase coding sequence fused to an N-terminal hemagglutinin-tagged tandem repeat of a partial sequence of XBP1 of human origin lacking its DNA-binding domain and containing the IRE1-cognate intron (pCAX-HA-2xXBP1ΔDBD(anATG)-LUC-F, kind gift of Takao Iwawaki(62), was used as a template to generate a retroviral expression construct. The coding sequence of the reporter was amplified by PCR using primers with engineered BamHI and EcoRI sites, and was subsequently cloned into the cognate sites of the retroviral expression vector pBABE.puro (Addgene) to generate construct DAA-A171. DAA-A171 was used to generate recombinant retroviral particles using standard methods and the resulting retroviral supernatant was used to transduce HEK293T cells, which were then subsequently selected with puromycin to create a stable reporter cell line.

7.10 Kinase-inhibitor profiling

IPA and cmp1 were assayed by Invitrogen to derive percent inhibition of kinase activity. All compounds were screened at 1 μ M and raw values are shown in supplementary tables. Detailed procedures for kinase reactions, ATP concentrations used and Z'-LYTE or Adapta assay formats are described in SelectScreen Customer Protocol (<http://www.invitrogen.com/kinaseprofiling>). Kinase-inhibition data for 1 μ M inhibitor of each of the clinical and tool compounds Staurosporine, Sunitinib, Dasatinib, Imatinib, SB202190, Erlotinib and Gefitinib were provided by Invitrogen based on stock results and not an independent comparison conducted or commissioned by the authors. Raw data of percent inhibition of all 266 kinases can be located in (Table 1 Invitrogen kinome screen raw data). Screening analysis for APY24 was previously reported (66).

7.11 In vitro PERK cross-linking assay

A solution of PERK cytosolic domain (535-1093 Δ 660-868) (2 μ M) was incubated with IPA or IPAx for 15 minutes before the addition of 250 μ M of the amino group-reactive cross-linking agent bis[sulfosuccinimidyl] suberate (BS2g-d0, Thermo Scientific). After 30 min incubation at room temperature Tris-HCl pH 7.5 was aged to a final concentration of 55 mM. Samples were then boiled in Laemmli sample buffer and loaded into an Any kD Mini-protean TGX gel (Bio Rad). Cross-linked protein was visualized using Colloidal Coomassie G-250 stain.

7.12 In vitro PERK kinase assay

GST-PERK kinase domain (580-1077 aa) was pre-incubated with compounds for 30 min. The kinase reaction was initiated by addition of ATP including 0.2 mCi γ -[³²P]-ATP. The final concentrations of the reactants were 50 nM GST-PERK, 50 μ M eIF2 α , 100 μ M ATP and varying concentrations of compound. At 30 minutes 2 μ l of each reaction was spotted onto a P81 phospho-cellulose membrane. The membrane was washed in 1% phosphoric acid and the sheets were washed five times in buffer, dried, and transferred radioactivity was measured using a Typhoon variable mode imager (GE Healthcare) and quantified using the ImageQuant (Molecular Devices). Titration data were fit to a sigmoidal dose response to derive IC₅₀ values using the SigmaPlot software package (Systat software). Dose responses were based on a 12-point inhibitor titration, using a semi-logarithmic dilution series starting from 30 μ M. Experiments were completed 2-4 times and mean values were computed.

7.12.1 PERK activation assay

PERK activation was measured using PERK (535-1093 Δ 660-868) in a buffer containing 20 mM Tris-HCl, 150 mM NaCl, 4 mM MgCl₂, 5 mM TCEP, 1% glycerol, pH 8.0. PERK concentration was 1 μ M, and activity was measured at 30°C. PERK was pre-incubated with 50 μ M of cold ATP in the presence or absence of IPA or IPAx. The reaction was then initiated by adding *S. cerevisiae* eIF2 α (1-180) and 0.2 mCi γ -[³²P]-ATP. The reaction was monitored over a time course of 30 min, during which 1/6 of the

reaction volume was removed at 0.5, 1,5, 10, 20 and 30 min and stopped in Laemmli buffer supplemented with 50 mM EDTA. Reactions were then boiled and loaded onto a 12.5 % Criterion precast gel (Bio-rad). The gel was then dried before imaging using a Typhoon variable mode imager (GE Healthcare). Gels were quantified using ImageQuant software and data was processed using SigmaPlot software package. Rates were determined using non-linear regression. Experiments were performed 3-times, and mean errors were determined.

The fraction PERK bound by IPA was calculated using the standard Langmuir isotherm equation. Using the calculated IC_{50} described in Figure 11.

$$\text{fraction bound} = \frac{1}{1 + \frac{IC_{50}}{[I]}}$$

Figure 17: Langmuir isotherm equation

7.13 Chemical synthesis

7.13.1 Synthesis of intermediate 3

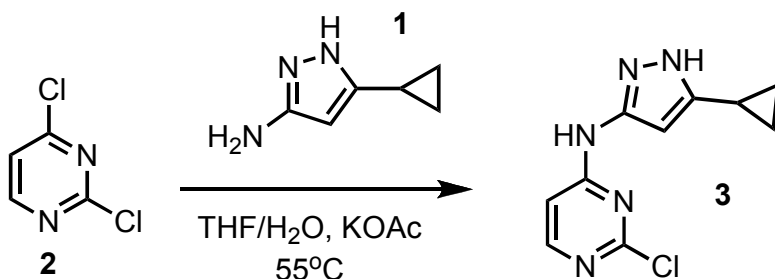


Figure 18: Synthesis of intermediate 3

2,4-dichloropyrimidine **2** (13.30 g, 89.31 mmol) and 3-amino-5-cyclopropylpyrazole **1** (11.00 g, 89.31 mmol) were dissolved in tetrahydrofuran (THF) (100 ml) followed by the addition of deionized water (100 ml). The solution was then treated with potassium acetate (261.9 g, 2.5 mol). The resulting mixture was kept at 55°C for 48 h. The mixture was filtered to remove excess potassium acetate. The organic layer was separated and dried using magnesium sulfate and concentrated before loading on an AnaLogix silica column. Intermediate **3** was separated as previously reported (34). ¹H NMR (400 MHz, DMSO) δ 12.14 (s, 1H), 10.23 (s, 1H), 1.84 (m, 1H), 0.88 (m, 2H), 0.64 (m, 2H). ¹³C NMR (100 MHz, DMSO) δ 161.4, 160.7, 160.0, 153.9, 148.6, 147.8, 146.8, 8.4, 8.2. MS calculated for C₁₀H₁₀N₅ 235.06, found 236.15 (M⁺).

7.13.2 Synthesis of intermediate 5

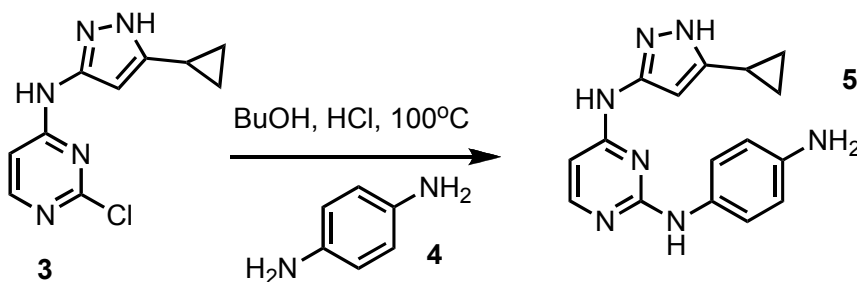


Figure 19: Synthesis of intermediate 5

Pyrimidine monochloride **3** (4 g, 16.9 mmol) (Oakwood chemical) and p-phenylene-diamine **4** (1.9 g, 16.9 mmol) (Sigma) were dissolved in butanol (BuOH) (50

ml) (Sigma) followed by the addition of concentrated HCl (0.1 ml) (Fisher Scientific). Resulting mixture was kept at 100°C overnight. Purple precipitate was collected by filtration, washed with 30 ml of cold BuOH and dried under vacuum yielding intermediate **5**, which was used in the next step without further purification. MS calculated for C₁₆H₁₇N₇ 307.15, found 308.5.

7.13.3 Synthesis of AD75/cmp1

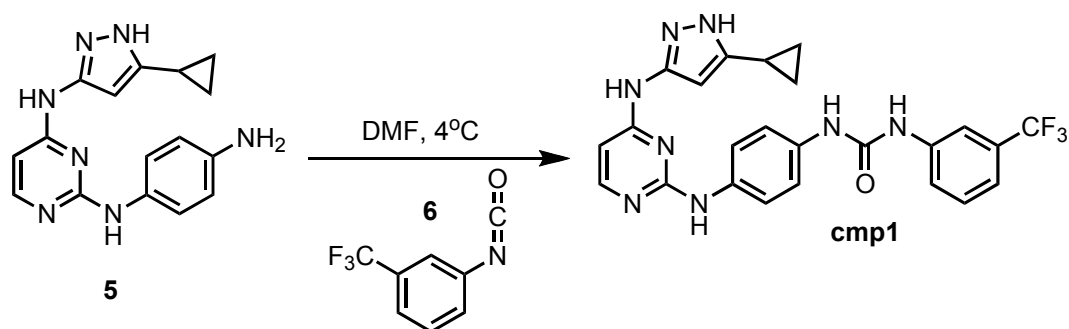


Figure 20: Synthesis of AD75/cmp1

Intermediate **5** (153 mg, 0.5 mmol) was dissolved in 10 ml of dry dimethylformamide (DMF) (Sigma). The flask was placed in an ice bath before addition of 3-(trifluoromethyl)phenyl isocyanate (93.5 mg; 0.069 ml; 0.5 mmol) **6** (Sigma) drop wise using a Hamilton syringe under argon. The resulting mixture was allowed to warm to room temperature overnight. Crude compound was isolated by addition of cold H₂O (30 ml) and isolated by filtration. Solid was washed with 100% CH₃CN and then suspended in 1:1 CH₃CN and distilled water (dH₂O) for reverse-phase purification using HPLC. A gradient from 2-80% CH₃CN:H₂O (0.1% TFA) was used to further during

purification on a C18 column (Agilent Technologies) followed by lyophilization to yielded **AD75/cmp1**. ^1H NMR (400 MHz, DMSO- d_6): δ 12.30 (s, 1H), 10.00 (s, 2H), 8.70 (s, 3H), 7.43 (m, $J = 2.3$ Hz, 6H), 6.62 (d, $J=2.1$ Hz, 5H), 5.29 (s, 1H) 2.51 (m, $J = 10.2$ Hz, 4H), 1.79 (t, $J= 9.6$ Hz, 1H), 0.87 (s, 4H) ^{13}C NMR (151 MHz, DMSO- d_6) δ 155.7, 152.8, 141.8, 138.4, 135.5, 133.6, 130.2, 129.3 128.9, 118.8, 112.6, 97.6, 8.9; ESI-MS m/z [M+H] found 495.49 calculated 494.49.

7.13.4 Synthesis of AM1/cmp4

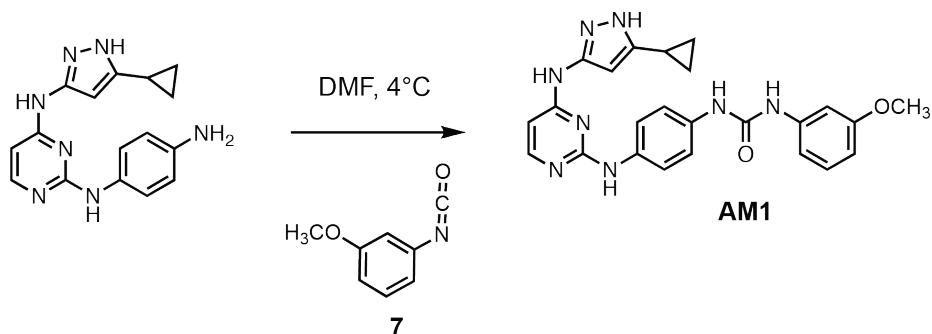


Figure 21: Synthesis of AM1/cmp4

Intermediate **5** (153 mg, 0.5 mmol) was dissolved in 10 ml of dry dimethylformamide (DMF) (Sigma). The flask was placed in an ice bath before addition of 3-methoxybenzene-1-isocyanate (93.5 mg; 0.069 ml; 0.5 mmol) **7** (Sigma) drop wise using a Hamilton syringe under argon. The resulting mixture was allowed to warm to room temperature overnight. Crude compound was isolated by addition of cold H_2O (30 ml) and isolated by filtration. Solid was washed with 100% CH_3CN and then suspended

in 1:1 CH₃CN and distilled water (dH₂O) for reverse-phase purification using HPLC. A gradient from 2-80% CH₃CN:H₂O (0.1% TFA) was used to further during purification on a C18 column (Agilent Technologies) followed by lyophilization to yielded **AM1/cmp3**.
¹H NMR (400 MHz, DMSO-d₆): δ 12.30 (s, 1H), 10.00 (s, 2H), 8.70 (s, 3H), 7.43 (m, *J* = 2.3 Hz, 6H), 5.62 (d, *J*=2.1 Hz, 5H), 5.29 (s, 1H) 2.51 (m, *J* = 10.2 Hz, 4H), 1.81 (t, *J*= 9.6 Hz, 1H), 0.87 (s, 4H) ¹³C NMR (151 MHz, DMSO-d₆) δ 155.7, 152.8, 141.8, 138.4, 140.5,133.6, 130.2, 129.3 130.9, 118.8, 112.6, 97.6, 10; ESI-MS *m/z* [M+H] found 457.18 calculated 456.20.

7.13.5 Synthesis of AM2

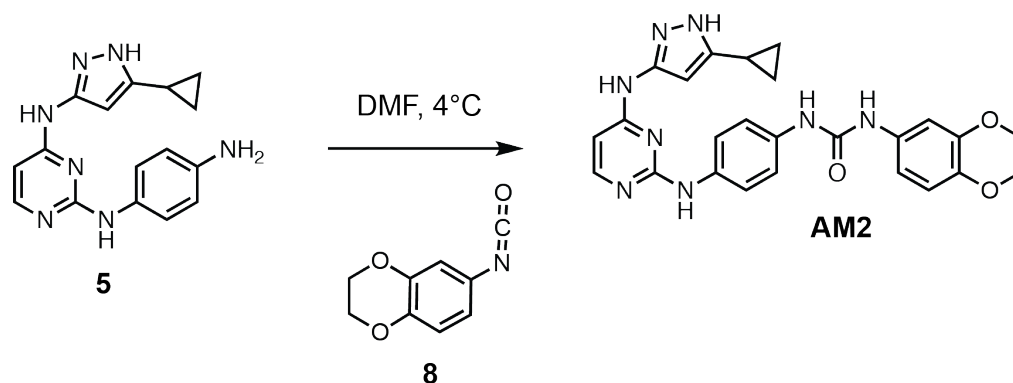


Figure 22: Synthesis of AM2

Intermediate **5** (153 mg, 0.5 mmol) was dissolved in 10 ml of dry DMF. The flask was placed in an ice bath before addition of 2,3-dihydrobenzo dioxine-6-isocyanate (.099 mg, 0.5 mmol) **8** (Sigma) drop wise using a Hamilton syringe under argon. The resulting mixture was allowed to warm to room temperature overnight. Crude compound

was isolated by addition of cold H₂O (30 ml) and isolated by filtration. Solid was washed with 100% CH₃CN and then suspended in 1:1 CH₃CN and dH₂O for reverse-phase purification using HPLC. A gradient from 2-80% CH₃CN:H₂O (0.1% TFA) was used to further during purification on a C18 column (Agilent Technologies) followed by lyophilization to yield **AM2**. ¹H NMR (400 MHz, DMSO-d₆): δ 12.21 (s, 1H), 9.51 (s, 1H), 8.81 (m, *J* = 21.8 Hz, 2H), 7.68 (d, *J* = 6.3 Hz, 1H), 7.82 (s, 1H), 8.48 (m, *J* = 22.5 Hz, 8H), 7.33 (d, *J* = 23.2 Hz, 2H), 7.08 (t, *J* = 7.2, 3H), 1.79 (s, 1H), 0.95 (s, 4H); ¹³C NMR (151 MHz DMSO-d₆) δ 155.3, 152.3, 130.9, 138.3, 140.6, 132.6, 122.4, 121.8, 118.8, 118.4, 95.4, 82.7, 10.2; ESI-MS *m/z* [M+H] found 485.25 calculated 484.20.

7.13.6 Synthesis of AM3

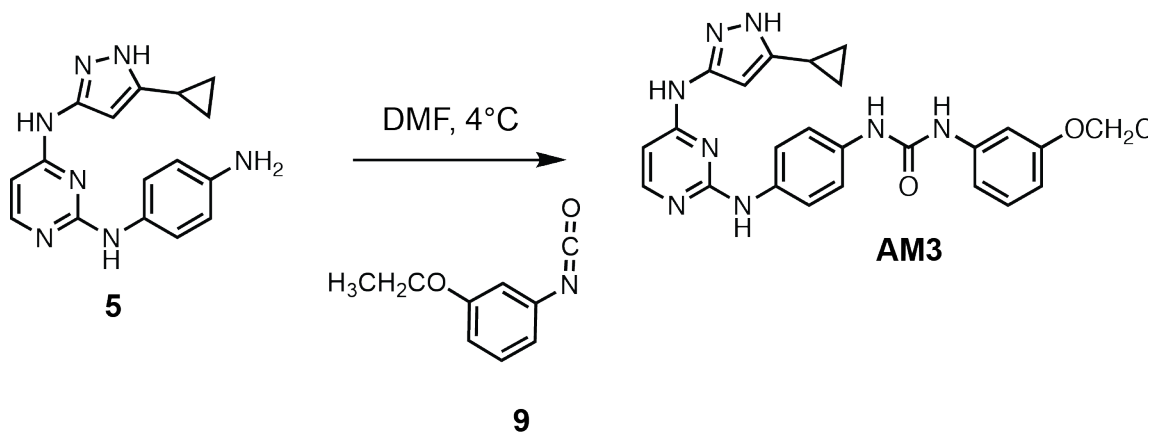


Figure 23: Synthesis of AM3

Intermediate **5** (153 mg, 0.5 mmol) was dissolved in 10 ml of dry DMF. The flask was placed in an ice bath before addition of 1-ethoxy-3-isocyanatobenzene (.122 mg,

0.5 mmol) **9** (Sigma) drop wise using a Hamilton syringe under argon. The resulting mixture was allowed to warm to room temperature overnight. Crude compound was isolated by addition of cold H₂O (30 ml) and isolated by filtration. Solid was washed with 100% CH₃CN and then suspended in 1:1 CH₃CN and dH₂O for reverse-phase purification using HPLC. A gradient from 2-80% CH₃CN:H₂O (0.1% TFA) was used to further during purification on a C18 column (Agilent Technologies) followed by lyophilization to yield **AM3**. ¹H NMR (400 MHz, DMSO-d₆): δ 12.21 (s, 1H), 9.10 (s, 1H), 8.81 (s, 1H), 8.79 (s, 1H), 8.52 (t, *J* = 4.5 Hz, 1H), 8.08 (s, 1H), 8.68 (m, *J* = 12.8 Hz, 2H), 7.38 (m, *J* = 8.2, 2H), 4.14 (d, *J* = 12.2 Hz, 2H), 1.79 (s, 1H), 0.87 (s, 4H); ¹³C NMR (151 MHz DMSO-d₆) δ 156.4, 152.9, 140.3, 131.7, 130.1, 133.5, 120.7, 120.2, 109.3, 104.9, 98.1, 80.7, 12.1; ESI-MS *m/z* [M+H] found 471.50 calculated 470.22.

7.13.7 Synthesis of AM4 / cmp5

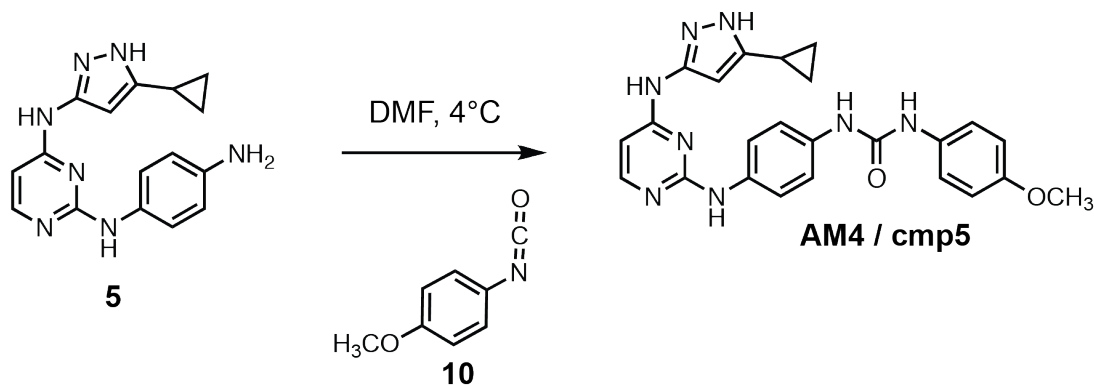


Figure 24: Synthesis of AM4 / cmp5

Intermediate **5** (153 mg, 0.5 mmol) was dissolved in 10 ml of dry DMF. The flask was placed in an ice bath before addition of 4-methoxyphenyl isocyanate (.075 mg; .065; 0.5 mmol) **10** (Sigma) drop wise using a Hamilton syringe under argon. The resulting mixture was allowed to warm to room temperature overnight. Crude compound was isolated by addition of cold H₂O (30 ml) and isolated by filtration. Solid was washed with 100% CH₃CN and then suspended in 1:1 CH₃CN and dH₂O for reverse-phase purification using HPLC. A gradient from 2-80% CH₃CN:H₂O (0.1% TFA) was used to further during purification on a C18 column (Agilent Technologies) followed by lyophilization to yield **AM4 / cmp5**. ¹H NMR (400 MHz, DMSO-d₆): δ 12.40 (s, 1H), 11.18 (s, 1H), 10.20 (s, 1H), 9.73 (q, *J* = 8.6 Hz, 2H), 8.78 (d, *J* = 8.9 Hz, 3H), 7.62 (t, *J* = 2.5 Hz 2H), 7.44 (t, *j* = 6.1 Hz, 3H), 6.98 (t, *J* = 7.2 Hz, 2H) 3.78 (m, *J* = 12.2 Hz, 3H), 1.79 (s, 1H), 0.87 (s, 4H), 0.54 (s, 2H); ¹³C NMR (151 MHz DMSO-d₆) δ 159.3, 153.1, 141.3, 125.3, 121.4, 110.4 108.6, 104.3, 58.3, 8.4; ESI-MS m/z [M+H] found 457.5 calculated 456.51.

7.13.8 Synthesis of AM5

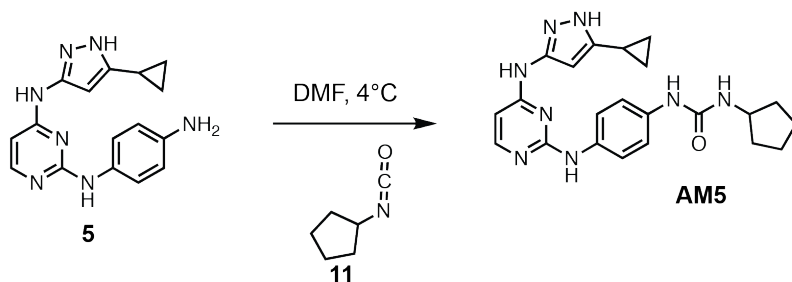


Figure 25: Synthesis of AM5

Intermediate **5** (153 mg, 0.5 mmol) was dissolved in 10 ml of dry DMF. The flask was placed in an ice bath before addition of isocyanatocyclopentane (.075 mg; .066 ml; 0.5 mmol) **11** (Sigma) drop wise using a Hamilton syringe under argon. The resulting mixture was allowed to warm to room temperature overnight. Crude compound was isolated by addition of cold H₂O (30 ml) and isolated by filtration. Solid was washed with 100% CH₃CN and then suspended in 1:1 CH₃CN and dH₂O for reverse-phase purification using HPLC. A gradient from 2-80% CH₃CN:H₂O (0.1% TFA) was used to further during purification on a C18 column (Agilent Technologies) followed by lyophilization to yield **AM5**. ¹H NMR (400 MHz, DMSO-d₆): δ 12.43 (s, 1H), 12.1 (s, 1H), 10.17 (s, 1H), 8.78 (d, *J*=19 Hz, 2H), 8.68, 7.82 (s, 1H), 9.57 (q, *j*=4.1 Hz, 2H), 7.41, 7.18 (d, *J* = 6.2 Hz, 2H), 7.84 (d, *J*= 4.8 Hz, 2H), 3.89 (s, 3H), 1.79, 0.87 (s, 4H); ¹³C NMR (151 MHz DMSO-d₆) δ 160.1, 152.95, 141.4, 132.0, 125.9, 112.9, 117.6, 114.4, 30.3, 8.37; ESI-MS *m/z* [M+H] found 419.16 calculated 418.22.

7.13.9 Synthesis of AM6

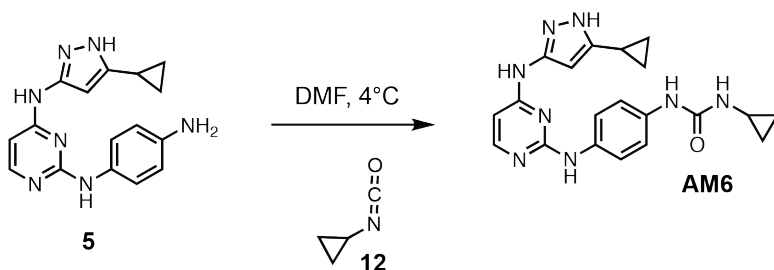


Figure 26: Synthesis of AM6

Intermediate **5** (153 mg, 0.5 mmol) was dissolved in 10 ml of dry DMF. The flask was placed in an ice bath before addition of 4-bromophenyl isocyanate (.099 mg, 0.5 mmol) **12** (Sigma) drop wise using a Hamilton syringe under argon. The resulting mixture was allowed to warm to room temperature overnight. Crude compound was isolated by addition of cold H₂O (30 ml) and isolated by filtration. Solid was washed with 100% CH₃CN and then suspended in 1:1 CH₃CN and dH₂O for reverse-phase purification using HPLC. A gradient from 2-80% CH₃CN:H₂O (0.1% TFA) was used to further during purification on a C18 column (Agilent Technologies) followed by lyophilization to yield **AM6**. ¹H NMR (400 MHz, DMSO-d₆): δ 12.21 (s, 1H), 9.51 (s, 1H), 8.81 (m, *J* = 21.8 HZ, 2H), 8.68 (d, *J* = 6.3 Hz, 1H), 8.82 (s, 1H), 7.08 (t, *J* = 7.2, 3H), 4.79 (s, 1H), 1.87 (s, 4H); ¹³C NMR (151 MHz DMSO-d₆) δ 155.3, 152.3, 140.9, 138.3, 129.4, 128.8, 127.8, 125.4, 100.4, 82.7, 19.2; ESI-MS m/z [M+H] found 391.21 calculated 390.19.

7.13.10 Synthesis of AM7

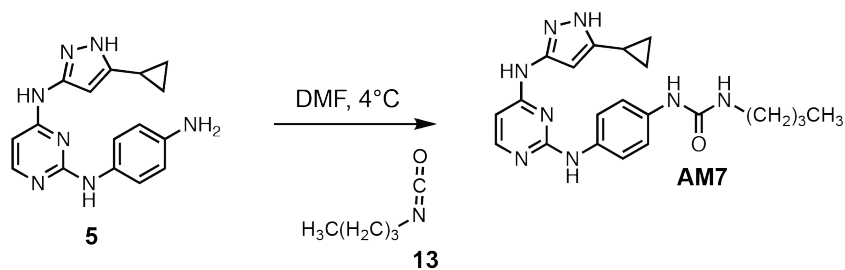


Figure 27: Synthesis of AM7

Intermediate **5** (153 mg, 0.5 mmol) was dissolved in 10 ml of dry DMF. The flask was placed in an ice bath before addition of 1-isocyanatobutane (.099 mg, 0.5 mmol) **13** (Sigma) drop wise using a Hamilton syringe under argon. The resulting mixture was allowed to warm to room temperature overnight. Crude compound was isolated by addition of cold H₂O (30 ml) and isolated by filtration. Solid was washed with 100% CH₃CN and then suspended in 1:1 CH₃CN and dH₂O for reverse-phase purification using HPLC. A gradient from 2-80% CH₃CN:H₂O (0.1% TFA) was used to further during purification on a C18 column (Agilent Technologies) followed by lyophilization to yield **AM7**. ¹H NMR (400 MHz, DMSO-d₆): δ 12.21 (s, 1H), 9.51 (s, 1H), 8.81 (m, *J* = 21.8 HZ, 2H), 8.68 (d, *J* = 6.3 Hz, 1H), 8.82 (s, 1H), 7.08 (t, *J* = 7.2, 3H), 4.79 (s, 1H), 1.87 (s, 4H); 125.4, 100.4, 82.7, 19.2; ESI-MS *m/z* [M+H] found 307.22 calculated 406.22.

7.13.11 Synthesis of AM8

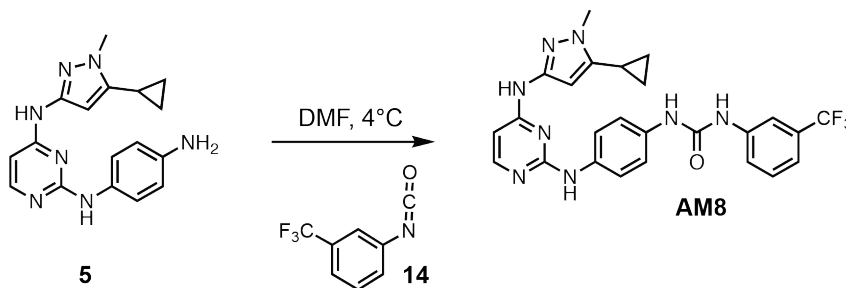


Figure 28: Synthesis of AM8

Intermediate **5** (153 mg, 0.5 mmol) was dissolved in 10 ml of dry DMF. The flask was placed in an ice bath before addition of 1-isocyanato-3-(trifluoromethyl)benzene (.075 mg; .066 ml; 0.5 mmol) **14** (Sigma) drop wise using a Hamilton syringe under argon. The resulting mixture was allowed to warm to room temperature overnight. Crude compound was isolated by addition of cold H₂O (30 ml) and isolated by filtration. Solid was washed with 100% CH₃CN and then suspended in 1:1 CH₃CN and dH₂O for reverse-phase purification using HPLC. A gradient from 2-80% CH₃CN:H₂O (0.1% TFA) was used to further during purification on a C18 column (Agilent Technologies) followed by lyophilization to yield **AM8**. ¹H NMR (400 MHz, DMSO-d₆): δ 12.43 (s, 1H), 12.1 (s, 1H), 10.17 (s, 1H), 8.78 (d, *J*=19 Hz, 2H), 8.68, 7.82 (s, 1H), 9.57 (q, *j*=4.1 Hz, 2H), 7.41, 7.18 (d, *J* = 6.2 Hz, 2H), 7.84 (d, *J* = 4.8 Hz, 2H), 3.89 (s, 3H), 1.79, 0.87; ESI-MS *m/z* [M+H] found 509.16 calculated 508.22.

7.13.12 Synthesis of AM9/IPA

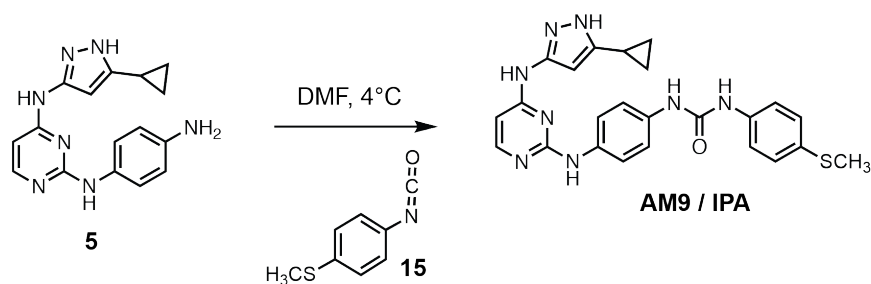


Figure 29: Synthesis of AM9/IPA

Intermediate **5** (153 mg, 0.5 mmol) was dissolved in 10 ml of dry DMF. The flask was placed in an ice bath before addition of isocyanatophenyl methyl sulfate (.082 mg; .07 ml; 0.5 mmol) **15** (sigma) drop wise using a Hamilton syringe under argon. The resulting mixture was allowed to warm to room temperature overnight. Crude compound was isolated by addition of cold H₂O (30 ml) and isolated by filtration. Solid was washed with 100% CH₃CN and then suspended in 1:1 CH₃CN and dH₂O for reverse-phase purification using HPLC. A gradient from 2-80% CH₃CN:H₂O (0.1% TFA) was used to further during purification on a C18 column (Agilent Technologies) followed by lyophilization to yield **AM9/IPA**. ¹H NMR (400 MHz, DMSO-d₆): δ 12.10 (s, 1H), 9.95 (s, 2H), 8.61 (d, *J* = 3.7 Hz 2H), 7.48 (d, *J* = 2.3 Hz, 8H), 7.22 (d, *J* = 21.3 Hz, 3H), 2.21 (m, *J* = 10.2 Hz, 3H), 1.79 (s, 1H), 0.87 (s, 4H); ¹³C NMR (151 MHz DMSO-d₆) δ 161.3, 155.3, 142.3, 140.6, 137.4, 135.8, 133.3, 131.2, 128.3, 119.5, 114.3, 16.5, 8.2; ESI-MS m/z [M+H] found 472.18 calculated 472.20.

7.13.13 Synthesis of AM10/cmp3

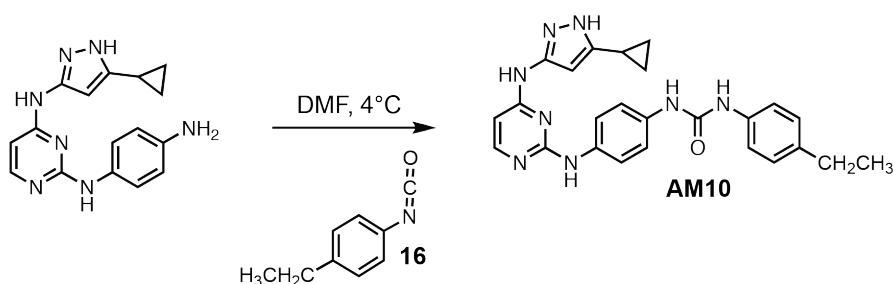


Figure 30: Synthesis of AM10/cmp3

Intermediate 5 (153 mg, 0.5 mmol) was dissolved in 10 ml of dry DMF. The flask was placed in an ice bath before addition of 4-Ethylphenyl isocyanate (.073 mg; .072 ml; 0.5 mmol) 8 (Sigma) drop wise using a Hamilton syringe under argon. The resulting mixture was allowed to warm to room temperature overnight. Crude compound was isolated by addition of cold H₂O (30 ml) and isolated by filtration. Solid was washed with 100% CH₃CN and then suspended in 1:1 CH₃CN and dH₂O for reverse-phase purification using HPLC. A gradient from 2-80% CH₃CN:H₂O (0.1% TFA) was used to further during purification on a C18 column (Agilent Technologies) followed by lyophilization to yield product cmp3. ¹H NMR (400 MHz, DMSO-d₆): δ 12.30 (s, 1H), 10.00 (s, 2H), 7.50 (d, J=2.1 Hz, 3H), 7.33 (s, 6H), 7.08 (t, J = 7.2 Hz, 3H), 1.79 (s, 2H), 1.13 (m, J = 13.4 Hz, 5H), 0.87 (s, 4H); ¹³C NMR (151 MHz DMSO-d₆) δ 162.4, 153.0, 141.16, 130.4, 130.0, 129.9, 123.8, 122.21, 118.4, 114.5, 113.9, 35.6, 8.4; ESI-MS m/z [M+H] found 455.5 calculated 454.31.

7.13.14 Synthesis of AM11

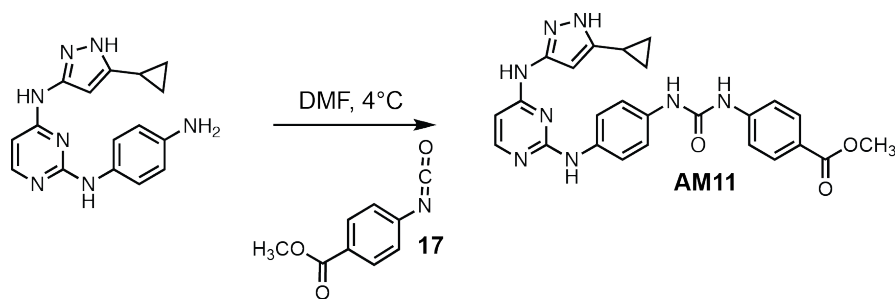


Figure 31: Synthesis of AM11

Intermediate **5** (153 mg, 0.5 mmol) was dissolved in 10 ml of dry DMF. The flask was placed in an ice bath before addition of methyl 4-isocyanatobenzoate (.075 mg; .066 ml; 0.5 mmol) **17** (Sigma) drop wise using a Hamilton syringe under argon. The resulting mixture was allowed to warm to room temperature overnight. Crude compound was isolated by addition of cold H₂O (30 ml) and isolated by filtration. Solid was washed with 100% CH₃CN and then suspended in 1:1 CH₃CN and dH₂O for reverse-phase purification using HPLC. A gradient from 2-80% CH₃CN:H₂O (0.1% TFA) was used to further during purification on a C18 column (Agilent Technologies) followed by lyophilization to yield **AM11**. ¹H NMR (400 MHz, DMSO-d₆): δ 12.43 (s, 1H), 11.1 (s, 1H), 10.17 (s, 1H), 8.78 (d, *J*=19 Hz, 2H), 8.68, 7.82 (s, 1H), 7.57 (q, *j*=6.1 Hz, 2H), 7.41 (t, *J*= 8.9 Hz, 2H), 7.18 (q, *J* = 7.2 Hz, 3H), 6.84 (d, *J*= 5.8 Hz, 1H), 3.89 (s, 3H), 1.79 (s, 1H), 0.87 (s, 4H); ¹³C NMR (151 MHz DMSO-d₆) δ 160.1, 152.95, 141.4, 130.0, 119.9, 110.9, 107.6, 104.4, 55.3, 8.37; ESI-MS *m/z* [M+H] found 485.19 calculated 484.20.

7.13.15 Synthesis of AM12

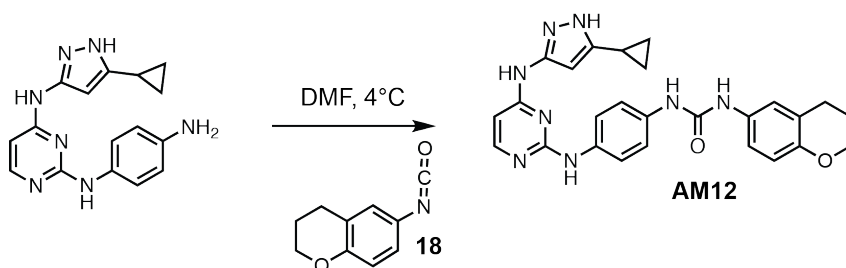


Figure 32: Synthesis of AM12

Intermediate **5** (153 mg, 0.5 mmol) was dissolved in 10 ml of dry DMF. The flask was placed in an ice bath before addition of 6-isocyanatochroman (.075 mg; .065; 0.5 mmol) **18** (Sigma) drop wise using a Hamilton syringe under argon. The resulting mixture was allowed to warm to room temperature overnight. Crude compound was isolated by addition of cold H₂O (30 ml) and isolated by filtration. Solid was washed with 100% CH₃CN and then suspended in 1:1 CH₃CN and dH₂O for reverse-phase purification using HPLC. A gradient from 2-80% CH₃CN:H₂O (0.1% TFA) was used to further during purification on a C18 column (Agilent Technologies) followed by lyophilization to yield **AM12**. ¹H NMR (400 MHz, DMSO-d₆): δ 12.40 (s, 1H), 11.18 (s, 1H), 10.20 (s, 1H), 9.73 (q, *J* = 8.6 Hz, 2H), 10.78 (d, *J* = 8.9 Hz, 3H), 7.62 (t, *J* = 2.5 Hz, 2H), 7.44 (t, *j* = 8.1 Hz, 2H), 8.98 (t, *J* = 7.2 Hz, 2H) 3.78 (m, *J* = 12.2 Hz, 3H), 2.79 (s, 1H), 1.87 (s, 2H), 0.54 (s, 2H); ESI-MS *m/z* [M+H] found 483.2 calculated 482.22.

7.13.16 Synthesis of AM13

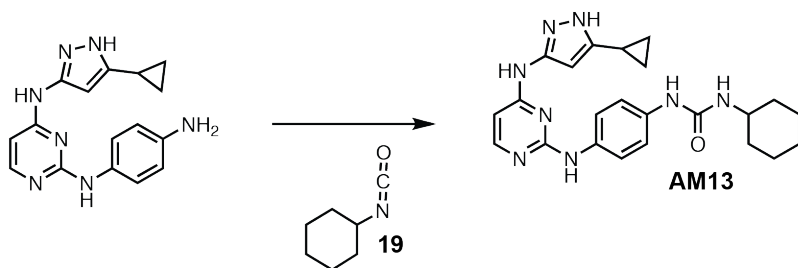


Figure 33: Synthesis of AM13

Intermediate **5** (153 mg, 0.5 mmol) was dissolved in 10 ml of dry DMF. The flask was placed in an ice bath before addition of isocyanatocyclohexane (.082 mg; .07 ml; 0.5 mmol) **19** (sigma) drop wise using a Hamilton syringe under argon. The resulting mixture was allowed to warm to room temperature overnight. Crude compound was isolated by addition of cold H₂O (30 ml) and isolated by filtration. Solid was washed with 100% CH₃CN and then suspended in 1:1 CH₃CN and dH₂O for reverse-phase purification using HPLC. A gradient from 2-80% CH₃CN:H₂O (0.1% TFA) was used to further during purification on a C18 column (Agilent Technologies) followed by lyophilization to yield **AM13**. ¹H NMR (400 MHz, DMSO-d₆): δ 12.10 (s, 1H), 9.95 (s, 2H), 8.61 (d, *J* = 3.7 Hz 2H), 7.48 (d, *J* = 2.3 Hz, 8H), 7.22 (d, *J* = 21.3 Hz, 3H), 2.21 (m, *J* = 10.2 Hz, 3H), 1.79 (s, 1H), 0.87 (s, 4H); ESI-MS *m/z* [M+H] found 433.25 calculated 432.24

7.13.17 Synthesis of AM14

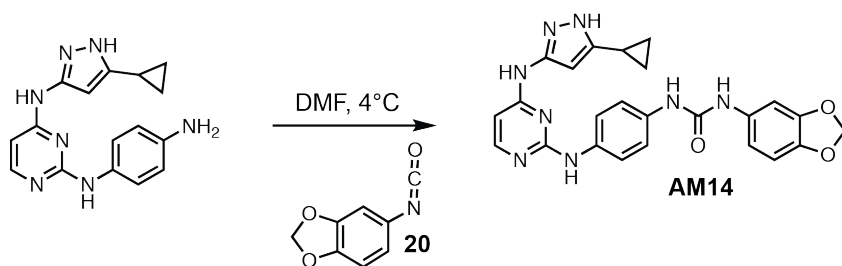


Figure 34: Synthesis of AM14

Intermediate **5** (153 mg, 0.5 mmol) was dissolved in 10 ml of dry DMF. The flask

was placed in an ice bath before addition of 5-isocyanatobenzo dioxole (.080 mg; .08; 0.5 mmol) **20** (Sigma) drop wise using a Hamilton syringe under argon. The resulting mixture was allowed to warm to room temperature overnight. Crude compound was isolated by addition of cold H₂O (30 ml) and isolated by filtration. Solid was washed with 100% CH₃CN and then suspended in 1:1 CH₃CN and dH₂O for reverse-phase purification using HPLC. A gradient from 2-80% CH₃CN:H₂O (0.1% TFA) was used to further during purification on a C18 column (Agilent Technologies) followed by lyophilization to yield **AM14**. ¹H NMR (400 MHz, DMSO-d₆): δ 12.11 (s, 1H), 8.51 (t, *J* = 13.6 Hz, 4H), 7.58 (m, *J* = 8.3 Hz, 2H), 7.22 (q, *J* = 12.6 Hz, 8H), 6.48 (d, *J* = 5.1 Hz, 1H), 1.13 (m, *J* = 13.4, 8H), 0.87 (m, *J* = 19.4 Hz, 4H); ESI-MS *m/z* [M+H] found 471.5 calculated 470.18.

7.13.18 Synthesis of AM15

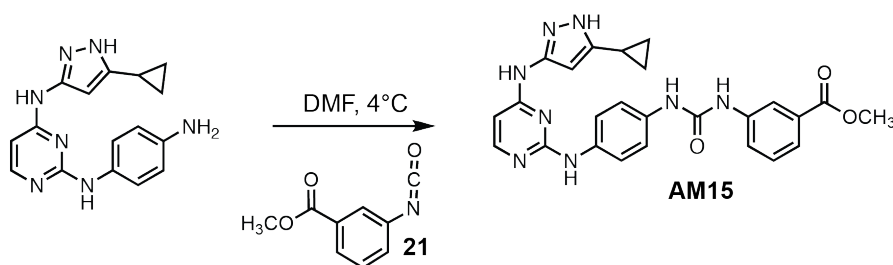


Figure 35: Synthesis of AM15

Intermediate **5** (200 mg, 0.5 mmol) was dissolved in 10 ml of dry DMF. The flask was placed in an ice bath before addition of 4-tert-butylphenyl isocyanate (.087 mg;

.089 ml; 0.5 mmol) **21** (Sigma) drop wise using a Hamilton syringe under argon. The resulting mixture was allowed to warm to room temperature overnight. Crude compound was isolated by addition of cold H₂O (30 ml) and isolated by filtration. Solid was washed with 100% CH₃CN and then suspended in 1:1 CH₃CN and dH₂O for reverse-phase purification using HPLC. A gradient from 2-80% CH₃CN:H₂O (0.1% TFA) was used to further during purification on a C18 column (Agilent Technologies) followed by lyophilization to yield **AM15**. ¹H NMR (400 MHz, DMSO-d₆): δ 12.11 (s, 1H), 9.43 (s, 1H), 8.81 (s, 1H), 8.68 (m, *J* = 22.3 Hz, 2H), 7.92 (s, 1H), 7.43 (m, *j* = 28.1 Hz, 8H), 6.28 (t, *J* = 7.2 Hz, 2H) 1.79 (s, 1H), 1.13 (s, 9H), 0.87 (s, 4H); ESI-MS *m/z* [M+H] found 485.5 calculated 484.55.

7.13.19 Synthesis of AM16

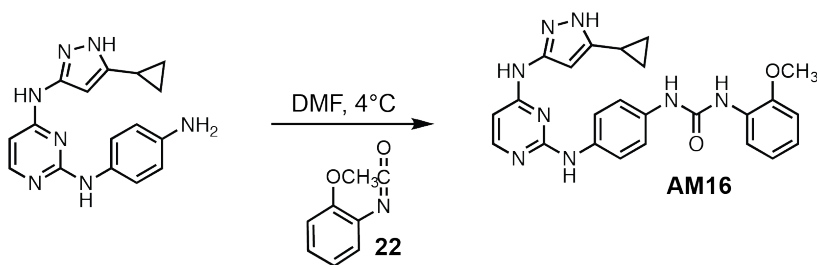


Figure 36: Synthesis of AM16

Intermediate **5** (153 mg, 0.5 mmol) was dissolved in 10 ml of dry DMF. The flask was placed in an ice bath before addition of isocyanatobenzoate (.075 mg; .066 ml; 0.5 mmol) **16** (Sigma) drop wise using a Hamilton syringe under argon. The resulting mixture was allowed to warm to room temperature overnight. Crude compound was

isolated by addition of cold H₂O (30 ml) and isolated by filtration. Solid was washed with 100% CH₃CN and then suspended in 1:1 CH₃CN and dH₂O for reverse-phase purification using HPLC. A gradient from 2-80% CH₃CN:H₂O (0.1% TFA) was used to further during purification on a C18 column (Agilent Technologies) followed by lyophilization to yield **AM16**. ¹H NMR (400 MHz, DMSO-d₆): δ 12.43 (s, 1H), 11.1 (s, 1H), 10.17 (s, 1H), 8.78 (d, J=19 Hz, 2H), 8.68, 7.82 (s, 1H), 7.57 (q, j =6.1 Hz, 2H), 7.41 (t, J= 8.9 Hz, 2H), 7.18 (q, J = 7.2 Hz, 3H), 6.84 (d, J= 5.8 Hz, 1H), 3.89 (s, 3H), 1.79 (s, 1H), 0.87 (s, 4H); ¹³C NMR (151 MHz DMSO-d₆) δ 160.1, 152.95, 141.4, 130.0, 119.9, 110.9, 107.6, 104.4, 55.3, 8.37; ESI-MS m/z [M+H] found 457.6 calculated 456.20.

7.13.20 Synthesis of AM17

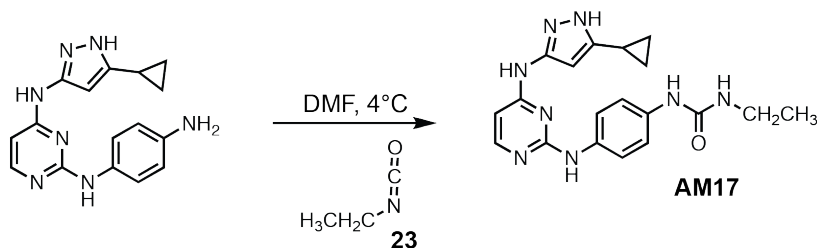


Figure 37: Synthesis of AM17

Intermediate **5** (153 mg, 0.5 mmol) was dissolved in 10 ml of dry DMF. The flask was placed in an ice bath before addition of 4-bromophenyl isocyanate (.099 mg, 0.5 mmol) **23** (Sigma) drop wise using a Hamilton syringe under argon. The resulting

mixture was allowed to warm to room temperature overnight. Crude compound was isolated by addition of cold H₂O (30 ml) and isolated by filtration. Solid was washed with 100% CH₃CN and then suspended in 1:1 CH₃CN and dH₂O for reverse-phase purification using HPLC. A gradient from 2-80% CH₃CN:H₂O (0.1% TFA) was used to further during purification on a C18 column (Agilent Technologies) followed by lyophilization to yield **AM17**. ¹H NMR (400 MHz, DMSO-d₆): δ 12.21 (s, 1H), 9.51 (s, 1H), 8.81 (m, *J* = 21.8 HZ, 2H), 8.68 (d, *J* = 6.3 Hz, 1H), 8.82 (s, 1H), 7.08 (t, *J* = 7.2, 3H), 4.79 (s, 1H), 1.87 (s, 4H); ¹³C NMR (151 MHz DMSO-d₆) δ 155.3, 152.3, 140.9, 138.3, 129.4, 128.8, 127.8, 125.4, 100.4, 82.7, 19.2; ESI-MS *m/z* [M+H] found 379.19 calculated 378.19.

7.13.21 Synthesis of AM18

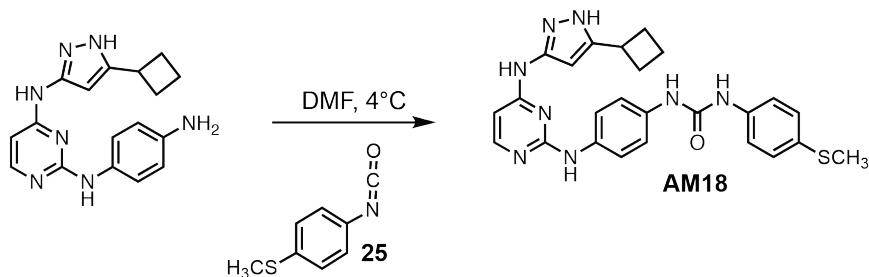


Figure 38: Synthesis of AM18

Intermediate **5** (153 mg, 0.5 mmol) was dissolved in 10 ml of dry dimethylformamide (DMF) (Sigma). The flask was placed in an ice bath before addition of 3-(trifluoromethyl)phenyl isocyanate (93.5 mg; 0.069 ml; 0.5 mmol) **25** (Sigma) drop

wise using a Hamilton syringe under argon. The resulting mixture was allowed to warm to room temperature overnight. Crude compound was isolated by addition of cold H₂O (30 ml) and isolated by filtration. Solid was washed with 100% CH₃CN and then suspended in 1:1 CH₃CN and distilled water (dH₂O) for reverse-phase purification using HPLC. A gradient from 2-80% CH₃CN:H₂O (0.1% TFA) was used to further during purification on a C18 column (Agilent Technologies) followed by lyophilization to yielded **AM18**. ¹H NMR (400 MHz, DMSO-d₆): δ 12.30 (s, 1H), 10.00 (s, 2H), 8.70 (s, 3H), 7.43 (m, *J* = 2.3 Hz, 6H), 6.62 (d, *J*=2.1 Hz, 5H), 5.29 (s, 1H) 2.51 (m, *J* = 10.2 Hz, 4H), 1.79 (t, *J*= 9.6 Hz, 1H), 0.87 (s, 4H) ; ESI-MS *m/z* [M+H] found 487.25 calculated 486.20.

7.13.22 Synthesis of AM19

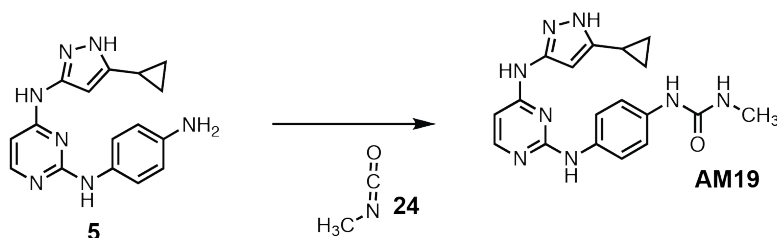


Figure 39: Synthesis of AM19

Intermediate **5** (153 mg, 0.5 mmol) was dissolved in 10 ml of dry dimethylformamide (DMF) (Sigma). The flask was placed in an ice bath before addition of isocyanatomethane (93.5 mg; 0.069 ml; 0.5 mmol) **25** (Sigma) drop wise using a Hamilton syringe under argon. The resulting mixture was allowed to warm to room temperature overnight. Crude compound was isolated by addition of cold H₂O (30 ml)

and isolated by filtration. Solid was washed with 100% CH₃CN and then suspended in 1:1 CH₃CN and distilled water (dH₂O) for reverse-phase purification using HPLC. A gradient from 2-80% CH₃CN:H₂O (0.1% TFA) was used to further during purification on a C18 column (Agilent Technologies) followed by lyophilization to yielded **AM19**. ¹H NMR (400 MHz, DMSO-d₆): δ 12.30 (s, 1H), 10.00 (s, 2H), 8.70 (s, 3H), 7.43 (m, *J* = 2.3 Hz, 6H), 6.62 (d, *J*=2.1 Hz, 5H), 5.29 (s, 1H) 2.51 (m, *J* = 10.2 Hz, 4H), 1.79 (t, *J*= 9.6 Hz, 1H), 0.87 (s, 4H); ESI-MS *m/z* [M+H] found 365.20 calculated 364.19.

7.13.23 Synthesis of AM20/cmp2

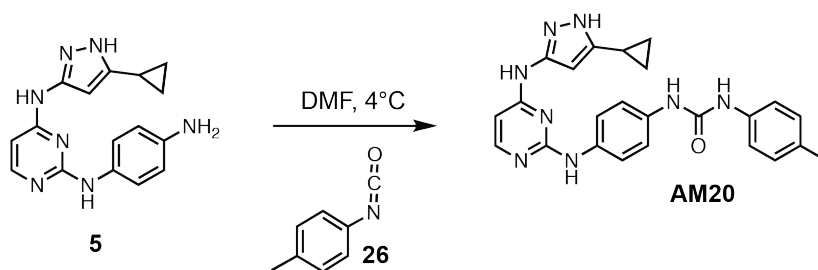


Figure 40: Synthesis of AM20/cmp2

Intermediate **5** (153 mg, 0.5 mmol) was dissolved in 10 ml of dry DMF. Flask was placed in an Ice bath before addition of p-Tolyl isocyanate (0.066 mg; 0.063 ml; 0.5 mmol) **26** (Sigma) drop wise using a Hamilton syringe under argon. Resulting mixture was allowed to warm to room temperature overnight. Crude compound was isolated by addition of cold H₂O (30 ml) and isolated by filtration. Solid was washed with 100% CH₃CN and then suspended in 1:1 CH₃CN and dH₂O for reverse-phase purification using HPLC. A gradient from 2-80% CH₃CN:H₂O (0.1% TFA) was used to further during

purification on a C18 column (Agilent Technologies) followed by lyophilization to yield **AM20/cmp2**. ^1H NMR (400 MHz, DMSO-d_6): δ 12.21 (s, 1H), 9.13 (s, 1H), 8.58 (q, $J = 1.3$ Hz, 9H), 8.35 (d, $J = 21.6$ Hz, 3H), 6.54 (s, 3H) 2.51 (m, $J = 10.2$ Hz, 4H), 1.89 (s, 1H) 1.29 (t, $J = 1.1$ Hz, 3H), 0.87 (s, 4H); ^{13}C NMR (151 MHz DMSO-d_6) δ 155.4, 153.8, 146.8, 140.3, 139.7, 136.7, 131.2, 127.8, 117.3, 115.4, 63.5, 33.5, 32.1 8.1; ESI-MS m/z $[\text{M}+\text{H}]$ found 440.28 calculated 440.21.

7.13.24 Synthesis of AM21

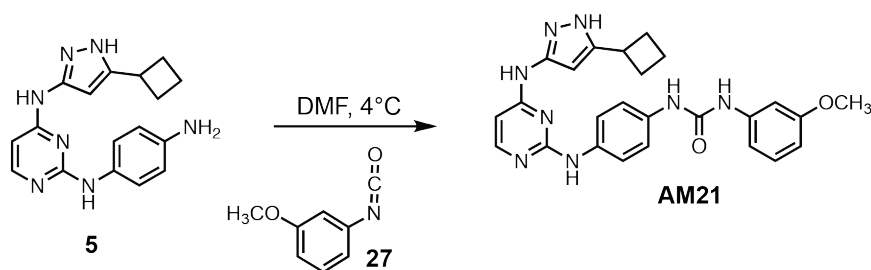


Figure 41: Synthesis of AM21

Intermediate **5** (153 mg, 0.5 mmol) was dissolved in 10 ml of dry DMF. The flask was placed in an ice bath before addition of 3-methoxyphenyl isocyanate (.075 mg; .066 ml; 0.5 mmol) **27** (Sigma) drop wise using a Hamilton syringe under argon. The resulting mixture was allowed to warm to room temperature overnight. Crude compound was isolated by addition of cold H_2O (30 ml) and isolated by filtration. Solid was washed with 100% CH_3CN and then suspended in 1:1 CH_3CN and dH_2O for reverse-phase purification using HPLC. A gradient from 2-80% $\text{CH}_3\text{CN}:\text{H}_2\text{O}$ (0.1% TFA) was used to

further during purification on a C18 column (Agilent Technologies) followed by lyophilization to yield **AM21**. ^1H NMR (400 MHz, DMSO- d_6): δ 12.43 (s, 1H), 11.1 (s, 1H), 10.17 (s, 1H), 8.78 (d, $J=19$ Hz, 2H), 8.68, 7.82 (s, 1H), 7.57 (q, $j=6.1$ Hz, 2H), 7.41 (t, $J=8.9$ Hz, 2H), 7.18 (q, $J=7.2$ Hz, 3H), 6.84 (d, $J=5.8$ Hz, 1H), 3.89 (s, 3H), 1.79 (s, 1H), 0.87 (s, 4H); ^{13}C NMR (151 MHz DMSO- d_6) δ 160.1, 152.95, 141.4, 130.0, 119.9, 110.9, 107.6, 104.4, 55.3, 8.37; ESI-MS m/z $[\text{M}+\text{H}]$ found 471.6 calculated 470.45.

7.13.25 Synthesis of AM22

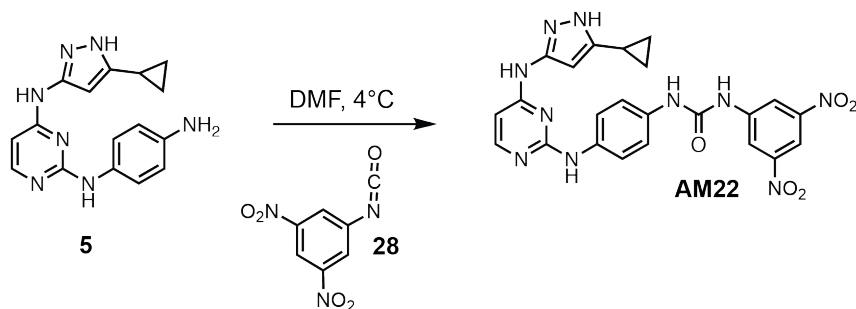


Figure 42: Synthesis of AM22

Intermediate **5** (153 mg, 0.5 mmol) was dissolved in 10 ml of dry DMF. The flask was placed in an ice bath before addition of 4-iodophenyl isocyanate (.122 mg, 0.5 mmol) **28** (Sigma) drop wise using a Hamilton syringe under argon. The resulting mixture was allowed to warm to room temperature overnight. Crude compound was isolated by addition of cold H_2O (30 ml) and isolated by filtration. Solid was washed with 100% CH_3CN and then suspended in 1:1 CH_3CN and dH_2O for reverse-phase

purification using HPLC. A gradient from 2-80% CH₃CN:H₂O (0.1% TFA) was used to further during purification on a C18 column (Agilent Technologies) followed by lyophilization to yield **cmp7**. ¹H NMR (400 MHz, DMSO-d₆): δ 12.21 (s, 1H), 9.10 (s, 1H), 8.81 (s, 1H), 8.79 (s, 1H), 8.52 (t, *J* = 8.5 Hz, 1H), 8.08 (s, 1H), 7.68 (m, *J* = 11.8 Hz, 4H), 7.38 (m, *J* = 10.2, 4H), 6.14 (d, *J* = 15.2 Hz, 2H), 1.79 (s, 1H), 0.87 (s, 4H); ESI-MS *m/z* [M+H] found 517.20 calculated 516.18.

7.13.26 Synthesis of AM23/IPAx

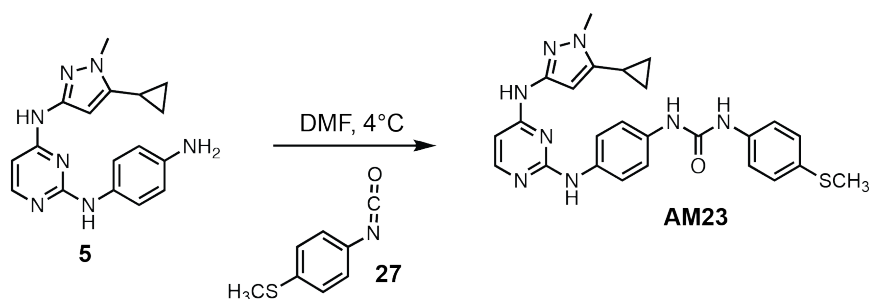


Figure 43: Synthesis of AM23/IPAx

Intermediate 5 (0.038 mg, 0.123 mmol) was dissolved in 5 ml of dry DMF. The flask was placed in a ice bath before addition of 4-(methylthio)phenyl isocyanat (0.023 mg, 0.123 mmol) (sigma) drop wise using a Hamilton syringe under argon. The resulting mixture was allowed to warm to room temperature overnight. Crude compound was isolated by addition of cold H₂O (30 ml) and isolated by filtration. Solid was washed with 100% CH₃CN and then suspended in 1:1 CH₃CN and dH₂O for reverse-phase purification using HPLC. A gradient from 2-80% CH₃CN:H₂O (0.1% TFA) was used to

further during purification on a C18 column (Agilent Technologies) followed by lyophilization to yield **AM23/IPAX**. ^1H NMR (400 MHz, DMSO- d_6): δ 10.00 (s, 2H), 8.81 (s, 1H), 8.68 (d, $J = 2.3$ Hz, 1H), 7.82 (s, 1H), 7.50 (d, $J = 2.1$ Hz, 3H), 7.33 (s, 6H), 7.08 (t, $J = 7.2$, 3H), 6.08 (s, 2H), 1.79 (s, 1H), 0.87 (s, 4H); ^{13}C NMR (151 MHz DMSO- d_6) δ 162.4, 153.0, 141.1, 131.3, 130.1, 129.3, 123.8, 122.1, 118.2, 115.2, 114.2, 8.4; ESI-MS m/z $[\text{M}+\text{H}]^+$ found 487.5 calculated 486.21.

7.13.27 Synthesis of AM24

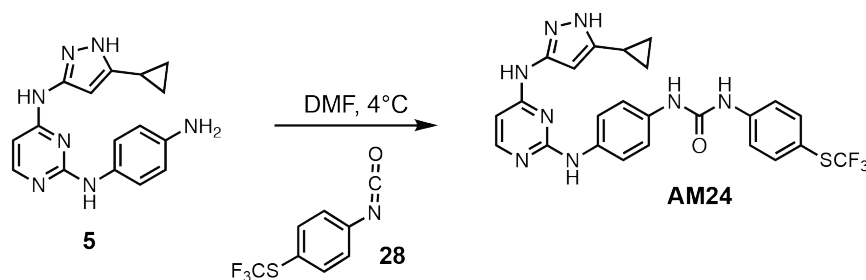


Figure 44: Synthesis of AM24

Intermediate **5** (153 mg, 0.5 mmol) was dissolved in 10 ml of dry DMF. The flask was placed in an ice bath before addition of isocyanatophenyl trifluoromethyl sulfane (.099 mg, 0.5 mmol) **28** (Sigma) drop wise using a Hamilton syringe under argon. The resulting mixture was allowed to warm to room temperature overnight. Crude compound was isolated by addition of cold H_2O (30 ml) and isolated by filtration. Solid was washed with 100% CH_3CN and then suspended in 1:1 CH_3CN and dH_2O for reverse-phase purification using HPLC. A gradient from 2-80% $\text{CH}_3\text{CN}:\text{H}_2\text{O}$ (0.1% TFA) was used to

further during purification on a C18 column (Agilent Technologies) followed by lyophilization to yield **AM24**. ^1H NMR (400 MHz, DMSO-d_6): δ 12.21 (s, 1H), 9.51 (s, 1H), 8.81 (m, $J = 21.8$ Hz, 2H), 8.68 (d, $J = 6.3$ Hz, 1H), 7.82 (s, 1H), 7.48 (m, $J = 22.5$ Hz, 8H), 7.33 (d, $J = 23.2$ Hz, 2H), 7.08 (t, $J = 7.2$, 3H), 1.79 (s, 1H), 0.87 (s, 4H); found 527.25 calculated 526.15.

7.13.28 Synthesis of AM25/cmp9

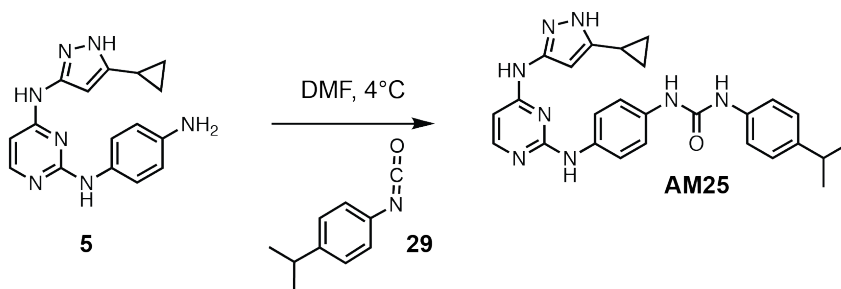


Figure 45: Synthesis of AM25/cmp9

Intermediate **5** (153 mg, 0.5 mmol) was dissolved in 10 ml of dry DMF. The flask was placed in an ice bath before addition of 4-isopropylphenyl isocyanate (.080 mg; .08; 0.5 mmol) **29** (Sigma) drop wise using a Hamilton syringe under argon. The resulting mixture was allowed to warm to room temperature overnight. Crude compound was isolated by addition of cold H_2O (30 ml) and isolated by filtration. Solid was washed with 100% CH_3CN and then suspended in 1:1 CH_3CN and dH_2O for reverse-phase purification using HPLC. A gradient from 2-80% $\text{CH}_3\text{CN}:\text{H}_2\text{O}$ (0.1% TFA) was used to further during purification on a C18 column (Agilent Technologies) followed by

lyophilization to yield **AM25**. ^1H NMR (400 MHz, DMSO- d_6): δ 12.11 (s, 1H), 8.51 (t, J = 13.6 Hz, 4H), 7.58 (m, J = 8.3 Hz, 2H), 7.22 (q, J = 12.6 Hz, 8H), 6.48 (d, J = 5.1 Hz, 1H), 1.13 (m, J = 13.4, 8H), 0.87 (m, J = 19.4 Hz, 4H); ^{13}C NMR (151 MHz DMSO- d_6) δ 158.3, 151.6, 144.7, 139.3, 138.6, 136.9, 134.5, 124.8, 119.1, 118.5, 36.5, 32.5, 8.1; ESI-MS m/z [M+H] found 469.5 calculated 468.24.

7.13.29 Synthesis of AM26

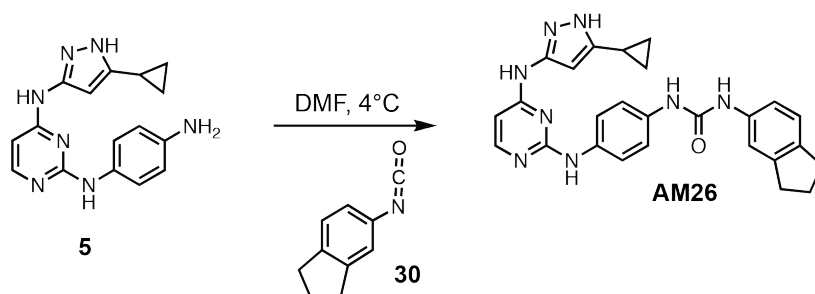


Figure 46: Synthesis of AM26

Intermediate **5** (153 mg, 0.5 mmol) was dissolved in 10 ml of dry DMF. The flask was placed in an ice bath before addition of isocyanato 2,3-dihydro-1H-indene (.082 mg; .07 ml; 0.5 mmol) **30** (sigma) drop wise using a Hamilton syringe under argon. The resulting mixture was allowed to warm to room temperature overnight. Crude compound was isolated by addition of cold H₂O (30 ml) and isolated by filtration. Solid was washed with 100% CH₃CN and then suspended in 1:1 CH₃CN and dH₂O for reverse-phase purification using HPLC. A gradient from 2-80% CH₃CN:H₂O (0.1% TFA) was used to further during purification on a C18 column (Agilent Technologies) followed by

lyophilization to yield **AM26**. $^1\text{H NMR}$ (400 MHz, DMSO-d_6): δ 12.10 (s, 1H), 9.95 (s, 2H), 8.61 (d, $J = 3.7$ Hz 2H), 7.48 (d, $J = 2.3$ Hz, 8H), 7.22 (d, $J = 21.3$ Hz, 3H), 2.21 (m, $J = 10.2$ Hz, 3H), 1.79 (s, 1H), 0.87 (s, 4H); ESI-MS m/z $[\text{M}+\text{H}]$ found 483.21 calculated 482.20.

7.13.30 Synthesis of **AM27/cmp10**

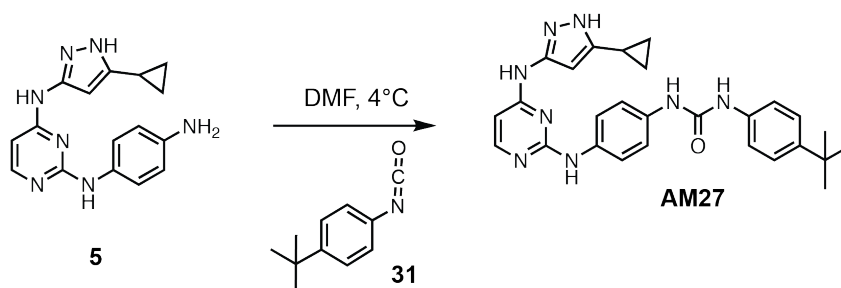


Figure 47: Synthesis of **AM27/cmp10**

Intermediate **5** (153 mg, 0.5 mmol) was dissolved in 10 ml of dry DMF. The flask was placed in an ice bath before addition of 4-isopropylphenyl isocyanate (.080 mg; .08; 0.5 mmol) **31** (Sigma) drop wise using a Hamilton syringe under argon. The resulting mixture was allowed to warm to room temperature overnight. Crude compound was isolated by addition of cold H_2O (30 ml) and isolated by filtration. Solid was washed with 100% CH_3CN and then suspended in 1:1 CH_3CN and dH_2O for reverse-phase purification using HPLC. A gradient from 2-80% $\text{CH}_3\text{CN}:\text{H}_2\text{O}$ (0.1% TFA) was used to further during purification on a C18 column (Agilent Technologies) followed by lyophilization to yield **AM27/cmp10**. $^1\text{H NMR}$ (400 MHz, DMSO-d_6): δ 12.11 (s, 1H),

8.51 (t, $J = 13.6$ Hz, 4H), 7.58 (m, $J = 8.3$ Hz, 2H), 7.22 (q, $J = 12.6$ Hz, 8H), 6.48 (d, $J = 5.1$ Hz, 1H), 1.13 (m, $J = 13.4$, 8H), 0.87 (m, $J = 19.4$ Hz, 4H); ^{13}C NMR (151 MHz DMSO- d_6) δ 158.3, 151.6, 144.7, 139.3, 138.6, 136.9, 134.5, 124.8, 119.1, 118.5, 36.5, 32.5, 8.1; ESI-MS m/z [M+H] found 469.5 calculated 468.24.

7.13.31 Synthesis of AM28/cmp7

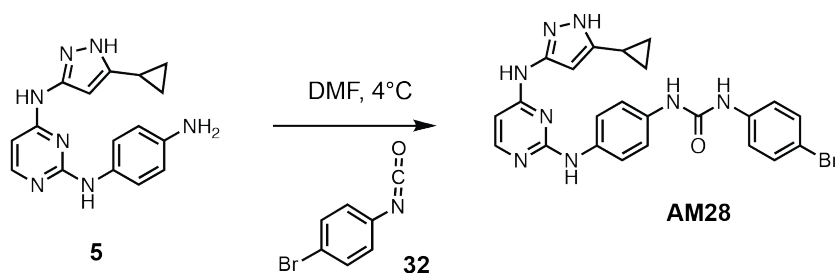


Figure 48: Synthesis of AM28/cmp7

Intermediate **5** (153 mg, 0.5 mmol) was dissolved in 10 ml of dry DMF. The flask was placed in an ice bath before addition of 4-bromophenyl isocyanate (.099 mg, 0.5 mmol) **32** (Sigma) drop wise using a Hamilton syringe under argon. The resulting mixture was allowed to warm to room temperature overnight. Crude compound was isolated by addition of cold H₂O (30 ml) and isolated by filtration. Solid was washed with 100% CH₃CN and then suspended in 1:1 CH₃CN and dH₂O for reverse-phase purification using HPLC. A gradient from 2-80% CH₃CN:H₂O (0.1% TFA) was used to further during purification on a C18 column (Agilent Technologies) followed by lyophilization to yield **AM28/cmp7**. ^1H NMR (400 MHz, DMSO- d_6): δ 12.21 (s, 1H), 9.51

(s, 1H), 8.81 (m, $J = 21.8$ Hz, 2H), 8.68 (d, $J = 6.3$ Hz, 1H), 7.82 (s, 1H), 7.48 (m, $J = 22.5$ Hz, 8H), 7.33 (d, $J = 23.2$ Hz, 2H), 7.08 (t, $J = 7.2$, 3H), 1.79 (s, 1H), 0.87 (s, 4H); ^{13}C NMR (151 MHz DMSO- d_6) δ 155.3, 152.3, 140.9, 138.3, 137.6, 132.6, 122.4, 121.8, 120.8, 118.4, 95.4, 82.7, 8.2; ESI-MS m/z $[M+H]$ found 505.5 calculated 504.10.

7.13.32 Synthesis of AM29/cmp8

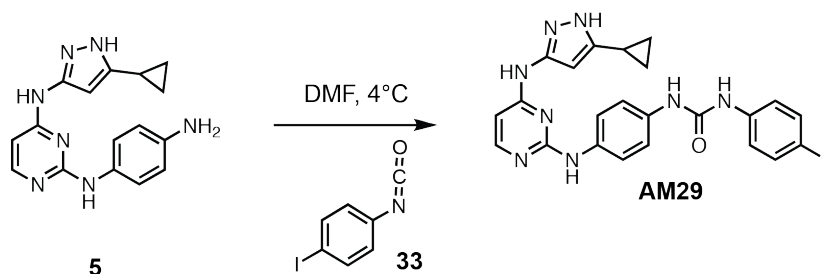


Figure 49: AM29/cmp8

Intermediate **5** (153 mg, 0.5 mmol) was dissolved in 10 ml of dry DMF. The flask was placed in an ice bath before addition of 4-iodophenyl isocyanate (122 mg, 0.5 mmol) **33** (Sigma) drop wise using a Hamilton syringe under argon. The resulting mixture was allowed to warm to room temperature overnight. Crude compound was isolated by addition of cold H₂O (30 ml) and isolated by filtration. Solid was washed with 100% CH₃CN and then suspended in 1:1 CH₃CN and dH₂O for reverse-phase purification using HPLC. A gradient from 2-80% CH₃CN:H₂O (0.1% TFA) was used to further during purification on a C18 column (Agilent Technologies) followed by lyophilization to yield **AM29/cmp8**. ^1H NMR (400 MHz, DMSO- d_6): δ 12.21 (s, 1H), 9.10

(s, 1H), 8.81 (s, 1H), 8.79 (s, 1H), 8.52 (t, $J = 8.5$ Hz, 1H), 8.08 (s, 1H), 7.68 (m, $J = 11.8$ Hz, 4H), 7.38 (m, $J = 10.2$, 4H), 6.14 (d, $J = 15.2$ Hz, 2H), 1.79 (s, 1H), 0.87 (s, 4H); ^{13}C NMR (151 MHz DMSO- d_6) δ 156.4, 152.9, 140.3, 137.7, 136.1, 133.5, 120.7, 120.2, 119.3, 116.9, 98.1, 84.7, 8.1; ESI-MS m/z $[\text{M}+\text{H}]$ found 553.3 calculated 552.08.

7.13.33 Synthesis of AM30

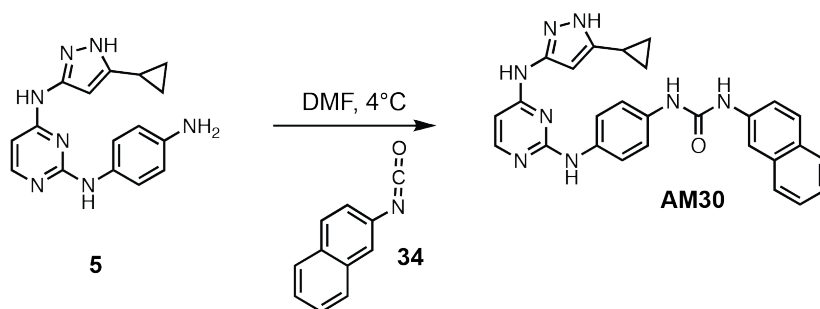


Figure 50: Synthesis of AM30

Intermediate **5** (200 mg, 0.5 mmol) was dissolved in 10 ml of dry DMF. The flask was placed in an ice bath before addition of isocyanatophthalene (.087 mg; .089 ml; 0.5 mmol) **30** (Sigma) drop wise using a Hamilton syringe under argon. The resulting mixture was allowed to warm to room temperature overnight. Crude compound was isolated by addition of cold H_2O (30 ml) and isolated by filtration. Solid was washed with 100% CH_3CN and then suspended in 1:1 CH_3CN and dH_2O for reverse-phase purification using HPLC. A gradient from 2-80% $\text{CH}_3\text{CN}:\text{H}_2\text{O}$ (0.1% TFA) was used to further during purification on a C18 column (Agilent Technologies) followed by

lyophilization to yield **AM30**. $^1\text{H NMR}$ (400 MHz, DMSO-d_6): δ 12.11 (s, 1H), 9.43 (s, 1H), 8.81 (s, 1H), 8.68 (m, $J = 22.3$ Hz, 2H), 7.92 (s, 1H), 7.43 (m, $J = 28.1$ Hz, 8H), 6.28 (t, $J = 7.2$ Hz, 2H) 1.79 (s, 1H), 1.13 (s, 9H), 0.87 (s, 4H); ESI-MS m/z $[\text{M}+\text{H}]$ found 477.35 calculated 476.25.

7.13.34 Synthesis of AM31

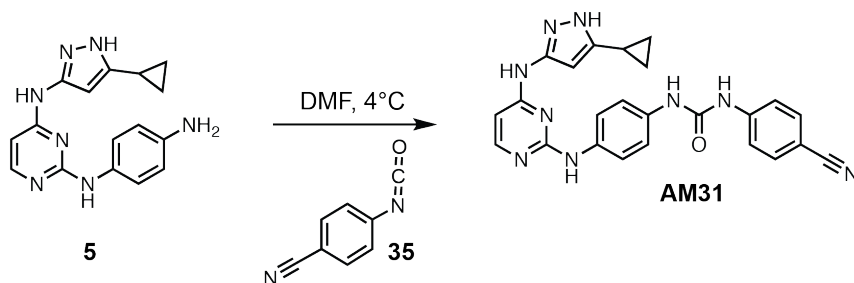


Figure 51: synthesis of AM31

Intermediate **5** (153 mg, 0.5 mmol) was dissolved in 10 ml of dry DMF. The flask was placed in an ice bath before addition of isocyanatobenzonitrile (.099 mg, 0.5 mmol) **35** (Sigma) drop wise using a Hamilton syringe under argon. The resulting mixture was allowed to warm to room temperature overnight. Crude compound was isolated by addition of cold H_2O (30 ml) and isolated by filtration. Solid was washed with 100% CH_3CN and then suspended in 1:1 CH_3CN and dH_2O for reverse-phase purification using HPLC. A gradient from 2-80% $\text{CH}_3\text{CN}:\text{H}_2\text{O}$ (0.1% TFA) was used to further during purification on a C18 column (Agilent Technologies) followed by lyophilization to yield **AM31**. $^1\text{H NMR}$ (400 MHz, DMSO-d_6): δ 12.21 (s, 1H), 9.51 (s, 1H), 8.81 (m, $J = 21.8$

HZ, 2H), 8.68 (d, $J = 6.3$ Hz, 1H), 7.82 (s, 1H), 7.48 (m, $J = 22.5$ Hz, 8H), 7.33 (d, $J = 23.2$ Hz, 2H), 7.08 (t, $J = 7.2$, 3H), 1.79 (s, 1H), 0.87 (s, 4H); ESI-MS m/z [M+H] found 452.20 calculated 451.19.

7.14 Raw Kinome data

Table 1 Invitrogen kinome screen raw data

All kinases screened in the Invitrogen panel and their percent inhibitions. Classification of kinases can be located on the right hand column and the number of kinases inhibited can be located at the bottom of the last page of the panel.

		Sorafenib	Dasatinib	Imatinib	Gefetinib	SB 202190	Staurosporine	Sunitinib	Erlotinib	IPA	cmp1
Y	ABL1	9	101	81	17	-1	90	60	32	33	79
Y	ABL1 E255K	5	102	67	13	4	91	60	23	25	-5
Y	ABL1 G250E	6	102	58	10	1	93	66	17	75	13
Y	ABL1 T315I	2	17	-1	4	3	99	74	15	45	25
Y	ABL1 Y253F	10	102	51	24	5	91	73	38	45	20
Y	ABL2 (Arg)	9	102	55	25	10	91	20	33	36	23
S/T	ACVR1B (ALK4)	-2	12	-3	-3	18	54	-10	4	7	18
S/T	ADRBK1 (GRK2)	-1	1	-5	2	1	32	4	3	29	50
S/T	ADRBK2 (GRK3)	-2	1	-1	1	-2	28	-5	0	13	7
S/T	AKT1 (PKB alpha)	5	-1	6	3	2	97	9	2	1	81
S/T	AKT2 (PKB beta)	6	9	1	-1	4	84	20	-6	-1	8
S/T	AKT3 (PKB gamma)	7	6	-8	0	5	96	18	1	-1	1
Y	ALK	20	2	0	7	8	97	93	5	5	-6
S/T	AMPK A1/B1/G1	5	-3	2	3	4	103	86	1	9	8
S/T	AMPK A2/B1/G1	12	0	2	6	-1	101	85	5	49	2
S/T	AURKA (Aurora A)	6	0	21	-2	-2	98	38	4	76	7
S/T	AURKB (Aurora B)	38	7	1	5	2	100	68	15	96	49
S/T	AURKC (Aurora C)	9	5	-1	7	3	95	44	-5	95	63
Y	AXL	7	3	2	20	7	98	97	10	91	78
Y	BLK	-1	113	29	10	-3	101	80	0	13	66
Y	BMX	-2	100	-4	-4	-5	95	0	3	46	44
S/T	BRAF	53	51	27	17	79	102	38	19	-9	11
S/T	BRAF V599E	93	77	71	16	90	99	20	-19	22	19
S/T	BRSK1 (SAD1)	-2	-1	-7	9	9	100	58	1	80	91
Y	BTK	6	101	9	10	1	95	27	4	79	10
S/T	CAMK1 (CaMK1)	12	3	4	-11	-5	92	27	18	43	15
S/T	CAMK1D (CaMKI delta)	-1	19	-5	-1	3	106	29	9	13	52
S/T	CAMK2A (CaMKII alpha)	6	-5	-2	-2	0	100	73	4	61	9
S/T	CAMK2B (CaMKII beta)	1	-2	5	0	1	99	20	-4	33	51
S/T	CAMK2D (CaMKII delta)	5	5	6	-5	10	99	92	12	3	13
S/T	CAMK4 (CaMKIV)	-4	-3	-3	8	-2	81	43	5	16	14
S/T	CDC42 BPA (MRCKA)	-6	0	-11	-1	4	101	-4	1	15	9
S/T	CDC42 BPB (MRCKB)	-6	-2	-1	-3	-10	98	-12	-2	5	91
S/T	CDK1/cyclin B	0	1	2	-1	-6	100	5	2	18	3
S/T	CDK2/cyclin A	-10	8	-15	-7	2	94	-4	1	16	18
S/T	CDK5/p25	-2	8	3	-5	-1	109	18	6	12	23
S/T	CDK5/p35	-5	0	-1	-6	0	109	19	3	2	17
S/T	CDK7/cyclin H/MNAT1	2	-2	-4	-8	9	90	85	-1	26	7
S/T	CDK9/cyclin T1	-13	-12	-18	-5	4	96	-15	-22	85	18
S/T	CHEK1 (CHK1)	4	3	0	3	0	102	63	-1	59	11
S/T	CHEK2 (CHK2)	9	0	-21	5	4	103	95	2	77	7
S/T	CHUK (IKK alpha)	-18	-4	4	-14	6	79	0	1	47	3
S/T	CLK1	5	-1	6	1	8	85	81	-1	83	35
S/T	CLK2	28	-2	14	2	12	99	94	14	53	75
S/T	CLK3	-6	3	-4	0	1	19	-3	-1	77	85
Y	CSF1R (FMS)	94	97	97	8	4	100	104	4	13	80
Y	CSK	-2	103	2	11	5	89	2	14	10	23
S/T	CSNK1A1 (CK1 alpha 1)	7	-2	5	1	16	4	25	5	12	96
S/T	CSNK1D (CK1 delta)	-2	0	3	2	56	3	62	1	19	33
S/T	CSNK1E (CK1 epsilon)	-1	5	1	-3	33	-6	55	3	2	56
S/T	CSNK1G1 (CK1 gamma 1)	5	-4	14	-10	1	2	28	-1	8	7
S/T	CSNK1G2 (CK1 gamma 2)	-3	13	0	-3	3	14	51	-8	74	8
S/T	CSNK1G3 (CK1 gamma 3)	3	1	0	1	11	3	50	9	39	0
S/T	CSNK2A1 (CK2 alpha 1)	5	1	4	4	-2	7	6	1	14	11
S/T	CSNK2A2 (CK2 alpha 2)	3	-3	3	2	12	20	8	4	2	33
S/T	DAPK1	0	1	-1	0	3	100	32	-3	10	-1
S/T	DAPK3 (ZIPK)	2	-1	7	0	0	99	38	1	9	91
S/T	DCAMKL2 (DCK2)	5	3	2	-2	0	95	17	-2	10	32
S/T	DNA-PK	0	3	5	8	4	-1	2	0	8	16
S/T	DYRK1A	0	0	1	2	0	93	16	0	9	0
S/T	DYRK1B	-2	-1	-1	8	6	91	10	-1	3	1
S/T	DYRK3	1	0	3	0	15	82	25	1	1	7
S/T	DYRK4	-6	0	-8	-2	-1	5	-8	1	19	5
S/T	EEF2K	0	0	-2	7	8	1	2	0	6	12
Y	EGFR (ErbB1)	6	71	4	88	28	83	1	106	22	5
Y	EGFR (ErbB1) L858R	5	58	2	88	36	88	2	101	50	4
Y	EGFR (ErbB1) L861Q	1	82	7	93	31	85	-1	98	32	3
Y	EGFR (ErbB1) T790M	0	-8	3	84	20	101	18	21	9	4
Y	(ErbB1) T790M L858R	0	13	4	72	28	99	27	70	30	0
Y	EPHA1	-4	99	2	43	19	93	22	3	6	10
Y	EPHA2	21	92	11	25	27	87	8	9	15	81
Y	EPHA4	13	103	-4	28	12	90	5	13	5	43
Y	EPHA5	23	101	29	24	18	87	27	6	8	8
Y	EPHA8	12	101	25	38	18	81	5	5	8	81
Y	EPHB1	11	101	1	20	8	81	51	6	1	1
Y	EPHB2	14	100	7	22	4	70	44	5	5	1
Y	EPHB3	-1	95	6	3	6	13	-4	0	1	5

Y	EPHB4	5	100	5	31	0	44	25	1	11	1
Y	ERBB2 (HER2)	-2	6	-2	70	5	59	-2	27	25	15
Y	ERBB4 (HER4)	1	60	28	84	14	53	5	24	29	9
Y	FER	15	6	12	2	1	99	84	3	6	10
Y	FES (FPS)	-2	3	4	1	-2	100	63	-2	2	4
Y	FGFR1	14	4	-7	2	1	98	54	0	5	8
Y	FGFR2	58	18	7	11	5	108	76	10	9	20
Y	FGFR3	21	4	6	-5	8	94	58	1	17	24
Y	FGFR3 K650E	54	5	0	18	-5	105	76	9	14	4
Y	FGFR4	10	3	12	-12	-8	75	19	-8	6	91
Y	FGR	6	101	50	43	10	98	94	11	13	5
Y	FLT1 (VEGFR1)	62	8	6	0	10	97	45	9	3	17
Y	FLT3	90	38	1	18	5	100	96	19	12	10
Y	FLT3 D835Y	91	12	5	52	16	100	100	37	17	65
Y	FLT4 (VEGFR3)	85	6	13	13	5	92	92	11	-1	15
S/T	FRAP1 (mTOR)	-3	-3	-5	-13	6	-5	-5	-3	10	15
Y	FRK (PTK5)	19	101	19	21	10	98	63	7	44	5
Y	FYN	-4	101	16	3	-1	99	45	9	25	4
S/T	GRK4	-5	8	-3	-27	-7	95	18	13	22	2
S/T	GRK5	-3	-4	-2	0	1	80	10	1	62	3
S/T	GRK6	1	-1	-3	-1	-4	92	40	0	37	18
S/T	GRK7	3	1	6	1	0	99	41	3	56	8
S/T	GSG2 (Haspin)	-2	-3	4	1	21	97	18	-6	41	18
S/T	GSK3A (GSK3 alpha)	-3	0	-10	7	71	97	8	1	51	51
S/T	GSK3B (GSK3 beta)	21	-2	16	-2	40	98	19	-3	63	51
Y	HCK	-1	100	9	22	7	101	54	5	50	32
S/T	HIPK1 (Myak)	2	0	0	-2	0	13	41	2	60	48
S/T	HIPK2	8	-1	5	4	0	32	66	-1	93	19
S/T	HIPK3 (YAK1)	6	3	3	1	2	16	19	-7	3	32
S/T	HIPK4	85	10	11	10	-2	25	38	2	23	42
Y	IGF1R	2	6	8	4	-4	80	52	2	52	92
S/T	IKKB (IKK beta)	1	0	0	-1	0	57	3	4	7	89
S/T	IKBE (IKK epsilon)	-1	-2	1	0	-2	100	24	1	-1	76
Y	INSR	3	2	5	8	13	84	76	5	15	0
Y	INSRR (IRR)	0	7	4	4	-1	62	69	9	17	14
S/T	IRAK1	7	9	14	52	-5	93	86	-10	24	18
S/T	IRAK4	-4	2	-9	3	5	99	67	5	48	-2
Y	ITK	2	4	-10	7	3	94	83	-3	47	10
Y	JAK1	-4	3	-7	14	-5	100	38	9	11	3
Y	JAK2	2	44	1	0	-3	97	44	15	35	5
Y	JAK2 JH1 JH2	7	10	-3	-3	-3	108	29	-2	20	5
Y	JAK2 JH1 JH2 V617F	-9	6	-5	-3	-8	97	26	4	16	67
Y	JAK3	-12	25	3	0	5	97	45	35	36	68
Y	KDR (VEGFR2)	99	15	-3	23	23	102	90	19	7	2
Y	KIT	49	80	55	1	3	62	91	1	29	11
Y	KIT T670I	43	-3	10	2	-3	84	99	5	2	8
Y	LCK	18	102	78	34	3	102	94	17	5	91
S/T	LRRK2	9	17	-1	18	-3	100	96	44	12	15
S/T	LRRK2 G2019S	-12	10	4	-2	13	100	99	24	53	12
Y	LYN A	1	1	1	4	1	101	68	4	-1	21
Y	LYN B	24	101	82	57	12	102	92	26	10	-5
Y	LYN B	13	101	81	49	4	100	91	33	30	4
S/T	MAP2K1 (MEK1)	0	11	3	-2	0	100	59	12	51	21
S/T	MAP2K2 (MEK2)	1	13	4	3	8	99	68	5	60	27
S/T	MAP2K6 (MKK6)	17	3	1	-5	5	100	6	2	50	-6
S/T	MAP3K8 (COT)	6	8	-13	10	16	93	45	-4	47	10
S/T	MAP3K9 (MLK1)	3	1	-2	1	30	98	32	4	73	51
S/T	MAP4K2 (GCK)	0	13	-11	2	2	97	75	12	26	16
S/T	MAP4K4 (HGK)	17	31	16	11	20	100	98	9	17	16
S/T	MAP4K5 (KHS1)	38	66	-5	18	15	101	98	-5	26	19
S/T	MAPK1 (ERK2)	-1	5	5	0	0	22	5	1	29	42
S/T	MAPK10 (JNK3)	-11	-2	-3	7	18	5	-10	0	98	70
S/T	MAPK11 (p38 beta)	56	10	7	-1	79	15	0	-1	95	12
S/T	MAPK12 (p38 gamma)	6	-8	5	2	3	59	5	9	47	0
S/T	MAPK13 (p38 delta)	-4	20	5	-1	5	52	-2	-3	37	12
S/T	MAPK14 (p38 alpha)	11	22	-15	19	98	18	-7	12	7	36
S/T	MAPK14 (p38 alpha) Direct	46	75	2	19	94	10	-2	-2	54	94
S/T	MAPK3 (ERK1)	-6	3	0	-1	-1	16	-6	0	55	63
S/T	MAPK8 (JNK1)	-30	3	-12	5	12	26	-17	3	67	18
S/T	MAPK9 (JNK2)	-15	20	-1	5	23	11	-12	14	53	9
S/T	MAPKAP2	-8	2	-5	-2	0	51	-3	4	80	2
S/T	MAPKAP3	7	17	1	4	34	9	-1	7	79	30
S/T	MAPKAP5 (PRAK)	0	9	1	-1	0	38	15	6	75	24
S/T	MARK1 (MARK)	6	0	-5	6	9	102	63	2	95	18
S/T	MARK2	5	2	-2	4	5	96	66	0	39	65
S/T	MARK3	13	14	-2	12	11	102	88	19	28	32
S/T	MARK4	8	15	12	8	12	102	79	18	4	24
Y	MATK (HYL)	-5	7	4	-4	-1	68	-1	-4	48	59
S/T	MELK	3	3	9	20	2	101	90	1	35	77
Y	MERTK (cMER)	10	4	-1	16	10	99	98	3	8	91
Y	MET (cMet)	12	2	16	14	3	83	22	2	43	67
Y	MET M1250T	-2	-3	-4	6	3	74	23	-7	58	90

S/T	MINK1	1	19	5	5	23	101	97	14	51	45
S/T	MKNK1 (MKNK1)	32	-7	0	76	4	87	0	40	33	28
Y	MST1R (RON)	9	0	-4	0	0	95	9	-2	51	-1
S/T	MST4	-2	16	-9	3	17	98	20	17	71	59
Y	MUSK	78	12	5	-6	-5	95	100	8	76	46
S/T	MYLK2 (skMLCK)	14	6	6	-6	10	78	93	3	13	3
S/T	NEK1	6	1	6	2	-1	92	1	0	14	17
S/T	NEK2	0	-1	-4	-1	-5	3	3	-1	14	61
S/T	NEK4	-3	4	-4	0	-1	46	0	6	4	36
S/T	NEK6	-20	3	-19	3	-3	4	-17	4	4	13
S/T	NEK7	-3	5	-3	10	2	-5	-2	0	11	1
S/T	NEK9	-1	-4	-4	-9	-2	31	-2	5	84	59
Y	NTRK1 (TRKA)	29	13	8	3	2	101	97	6	17	41
Y	NTRK2 (TRKB)	13	2	-16	4	12	102	96	-2	28	55
Y	NTRK3 (TRKC)	46	6	6	-1	1	100	92	2	14	-4
S/T	NUAK1 (ARK5)	-11	-6	-8	-1	-9	98	91	0	8	11
S/T	PAK1	15	8	5	-2	5	94	3	-5	5	6
S/T	PAK2 (PAK65)	4	-2	2	7	7	100	4	1	30	11
S/T	PAK3	8	13	9	-9	5	97	33	-5	17	-2
S/T	PAK4	-25	1	-22	-5	22	101	38	-8	64	-8
S/T	PAK6	-14	-10	-3	4	0	103	6	-17	70	43
S/T	PAK7 (KIAA1264)	1	-2	7	3	2	97	47	-5	7	29
S/T	PASK	4	1	0	-3	12	94	3	0	75	12
Y	PDGFRA (PDGFR alpha)	94	96	97	6	-1	89	83	-15	18	45
Y	PDGFRA D842V	21	65	28	18	1	111	82	5	41	10
Y	PDGFRA T674I	41	-5	5	6	4	92	106	10	15	2
Y	PDGFRA V561D	101	101	103	84	48	105	100	50	22	1
Y	PDGFRB (PDGFR beta)	78	84	70	1	1	97	77	6	20	3
S/T	PDK1	12	8	11	3	1	92	37	1	39	18
S/T	PDK1 Direct	-9	-7	0	4	-10	99	59	6	51	18
S/T	PHKG1	1	7	-6	9	2	101	94	6	36	7
S/T	PHKG2	1	-2	-2	7	2	100	84	-8	-3	13
PI	PI4KA (PI4K alpha)	6	1	5	5	3	-8	-7	2	72	11
PI	PI4KB (PI4K beta)	-1	10	6	13	-1	15	19	9	18	36
PI	PIK3C2A (PI3K-C2 alpha)	7	12	11	9	12	3	2	7	34	19
PI	PIK3C2B (PI3K-C2 beta)	2	9	1	13	-5	0	-3	15	32	25
PI	PIK3C3 (hVPS34)	-17	-6	-1	5	3	-11	-29	-11	-11	6
PI	PIK3R1 (p110 alpha/p85)	-12	-9	-9	-20	1	-20	-7	-4	17	36
PI	PIK3R1 (p110 delta/p85)	-6	-13	-11	-13	-8	-27	-18	-11	9	91
PI	PIK3CG (p110 gamma)	8	-7	-16	-2	-3	13	4	0	12	80
S/T	PIM1	-16	2	-14	22	4	90	-14	4	7	70
S/T	PIM2	2	-6	-4	-9	6	94	-1	-2	15	10
S/T	PKN1 (PRK1)	-7	6	-3	6	6	102	10	15	78	53
S/T	PLK1	3	-2	5	-6	8	47	1	6	81	78
S/T	PLK2	3	1	7	0	1	58	2	8	87	12
S/T	PLK3	4	-14	5	-4	13	10	12	23	94	25
S/T	PRKACA (PKA)	-4	4	1	4	24	99	7	1	55	-3
S/T	PRKCA (PKC alpha)	28	2	-10	-1	-2	100	-7	16	51	-8
S/T	PRKCB1 (PKC beta)	-4	11	-19	-2	44	100	-12	15	24	7
S/T	PRKCB2 (PKC beta II)	-6	7	-22	2	11	100	-3	1	66	9
S/T	PRKCD (PKC delta)	-16	4	-17	0	9	101	-7	4	55	19
S/T	PRKCE (PKC epsilon)	5	7	-1	-2	5	103	2	-5	69	4
S/T	PRKCG (PKC gamma)	-10	3	-10	5	8	112	-3	5	-2	31
S/T	PRKCH (PKC eta)	-7	7	-20	6	4	105	-12	0	80	65
S/T	PRKCI (PKC iota)	-20	5	-12	1	-1	75	-17	7	16	67
S/T	PRKCN (PKD3)	6	7	-13	18	34	105	88	6	23	91
S/T	PRKCQ (PKC theta)	-11	10	-16	3	4	103	-15	0	38	93
S/T	PRKCZ (PKC zeta)	-8	0	-15	-3	-7	56	-11	3	49	43
S/T	PRKD1 (PKC mu)	-6	5	1	26	19	97	90	9	16	40
S/T	PRKD2 (PKD2)	5	-4	2	15	15	101	91	1	11	9
S/T	PRKG1	0	6	-3	1	17	95	24	-3	11	62
S/T	PRKG2 (PKG2)	10	9	12	7	5	96	19	-5	19	72
S/T	PRXK	-6	4	-8	8	15	102	17	4	5	52
Y	PTK2 (FAK)	10	14	10	6	1	97	77	7	54	-5
Y	PTK2B (FAK2)	-2	1	-4	2	2	98	67	1	6	31
Y	PTK6 (Brk)	-4	92	6	21	23	41	21	4	12	5
S/T	(cRAF) Y340D Y341D	93	57	64	5	81	94	46	13	31	17
Y	RET	94	25	3	28	4	100	96	23	15	80
Y	RET V804L	81	7	-7	6	4	100	99	1	12	27
Y	RET Y791F	94	47	8	37	3	99	98	34	23	26
S/T	ROCK1	-10	3	-11	-10	-4	103	11	8	6	5
S/T	ROCK2	-4	-13	-3	-3	2	102	7	8	13	11
Y	ROS1	-1	3	7	7	13	102	25	6	1	-7
S/T	RPS6KA1 (RSK1)	-3	0	3	3	-2	100	64	3	21	-7
S/T	RPS6KA2 (RSK3)	5	1	-4	15	15	102	78	-1	-2	41
S/T	RPS6KA3 (RSK2)	11	5	3	8	-3	106	64	2	9	-18
S/T	RPS6KA4 (MSK2)	10	-8	2	-15	25	102	73	-11	2	10
S/T	RPS6KA5 (MSK1)	0	8	3	-3	7	100	25	-4	22	80
S/T	RPS6KA6 (RSK4)	8	-2	7	15	103	105	88	-7	34	40
S/T	RPS6KB1 (p70S6K)	-9	-1	-16	-6	20	101	66	3	17	10
S/T	SGK (SGK1)	9	16	8	-1	3	98	66	8	14	17
S/T	SGK2	-3	-10	-1	-5	16	95	27	3	39	-11

S/T	SGKL (SGK3)	-4	-3	-1	7	15	93	10	1	19	4
S/T	SNF1LK2	9	96	9	29	11	99	54	15	50	-8
PI	SPHK1	8	2	1	6	4	0	10	11	30	-1
PI	SPHK2	3	3	7	3	3	-12	-13	8	11	5
Y	SRC	3	102	0	10	6	97	57	6	17	4
Y	SRC N1	-2	103	-7	15	6	102	54	17	8	-5
Y	SRMS (Srm)	3	93	8	4	7	75	12	3	1	29
S/T	SRPK1	1	1	5	1	2	54	6	1	87	-1
S/T	SRPK2	-6	-1	-12	-1	-2	20	-6	-1	90	5
S/T	STK22B (TSSK2)	3	1	5	-2	-1	97	15	15	24	19
S/T	STK22D (TSSK1)	0	12	6	3	-2	101	80	5	28	2
S/T	STK23 (MSSK1)	2	3	-5	-1	-3	15	0	-4	52	24
S/T	STK24 (MST3)	8	14	-9	4	4	99	80	16	23	10
S/T	STK25 (YSK1)	-11	2	-14	-8	17	99	23	4	18	11
S/T	STK3 (MST2)	-15	-3	-9	-4	-1	101	63	11	12	3
S/T	STK4 (MST1)	-11	4	-29	-9	-9	99	91	4	72	85
Y	SYK	2	24	8	15	15	101	42	-3	24	8
S/T	TAOK2 (TAO1)	22	0	-10	-10	8	97	1	1	19	-13
S/T	TBK1	5	7	3	13	3	100	54	4	90	91
Y	TEK (Tie2)	13	2	17	1	3	89	8	-7	25	91
Y	TXK	14	94	-2	50	28	94	19	27	0	9
Y	TYK2	0	17	2	2	1	102	60	-2	9	3
Y	TYRO3 (RSE)	5	9	0	5	7	100	81	6	30	95
Y	YES1	17	101	0	7	-1	98	92	5	28	13
Y	ZAP70	1	2	7	2	4	66	1	0	36	3

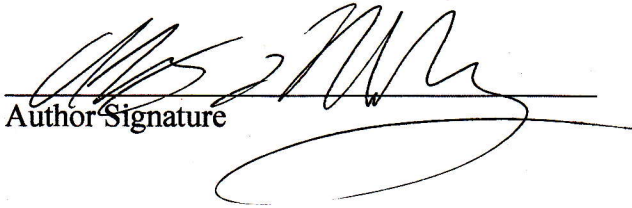
Total in red (ie. >80% inhib)	13	37	6	6	5	192	53	3	16	23
Total in column	266	266	266	266	266	266	266	266	266	266

Publishing Agreement

It is the policy of the University to encourage the distribution of all theses, dissertations, and manuscripts. Copies of all UCSF theses, dissertations, and manuscripts will be routed to the library via the Graduate Division. The library will make all theses, dissertations, and manuscripts accessible to the public and will preserve these to the best of their abilities, in perpetuity.

Please sign the following statement:

I hereby grant permission to the Graduate Division of the University of California, San Francisco to release copies of my thesis, dissertation, or manuscript to the Campus Library to provide access and preservation, in whole or in part, in perpetuity.



Author Signature

1/7/2016

Date